Pneumatic submersible caissons as a foundation for an offshore wind turbine

A new foundation for Offshore Wind Turbines
- A monopile comparison study

MSc thesis Civil Engineering

B.A.W. (Benjamin) Witmer

Delft University of Technology

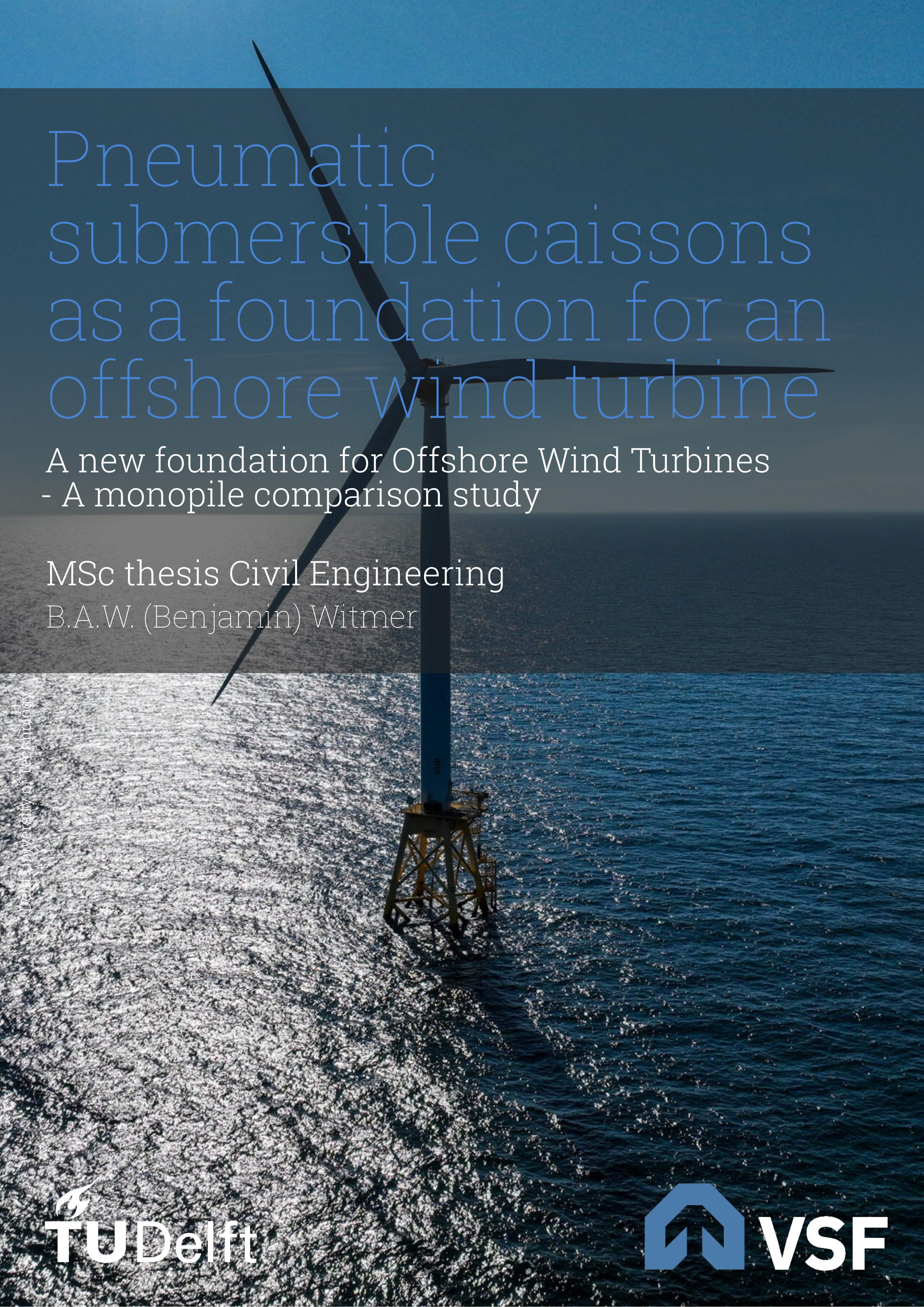

Pneumatic submersible caissons as a foundation for an offshore wind turbine

A new foundation for Offshore Wind Turbines - A monopile comparison study

by

B.A.W. (Benjamin) Witmer

to obtain the degree of Master of Science
at the Delft University of Technology
to be defended publicly on Monday December 9, 2024 at 11:00 AM.

Student number:	4716582	
Project duration:	April 22, 2024 – November, 2024	
Thesis committee:	Dr. ir. E. Kementzetzidis,	TU Delft, Chair
	Dr. ir. L. Flessati,	TU Delft
	Ing. D. Bergwerf,	Volker Staal en Funderingen (VSF)
	Ir. B. J. Admiraal,	Volker Staal en Funderingen (VSF)
	Ir. W. M. Visser	Iv-consult

Cover: A wind turbine generates electricity at the Block Island Wind Farm on July 07, 2022 near Block Island, Rhode Island. (Photo by John Moore/Getty Images)

Preface

My studies at the Delft University of Technology comes to an end with this thesis. It is the last stage I need to take to earn my Master of Science in Civil Engineering with a specialisation in Hydraulic and Offshore Structures. Throughout this study, I have developed a great interest in the offshore industry. This thesis has given me the opportunity to further follow this passion.

I would like to thank the people at VSF (Volker Staal en Funderingen) for their guidance and for providing a great atmosphere at the office. Especially I would like to thank my supervisors from VSF, Duco Bergwerf and Bartho Admiraal. First of all, I want to thank them for providing me with this thesis subject and the accompanying internship that I was able to follow. Together with their expertise in the foundation sector and their specific knowledge, they gave me great support during my thesis. Additionally, I would like to thank VSF for the opportunities they gave me to gain experience in the field. I was able to visit multiple project sites and also worked with VSF on one of their projects. This was an amazing experience.

I would like to thank my supervisors from the TU Delft, Vagelis Kementzetzidis and Luca Flessati. With their in-depth knowledge of soil-structure interactions and finite element models, they were able to provide me with the required guidance to support me during this thesis.

I would like to thank my family and friends for the support and patience they have had with me over the past years. Also, I would like to thank Sabine and Diederik for their support and kindness in letting me carpool with them to the office. I enjoyed the conversations in the car. Lastly, I would like to thank my study buddy, Jesper. We supported each other since the start of our student time.

B.A.W. (Benjamin) Witmer
Delft, December 2024

Abstract

This thesis investigates the soil-structure interaction and corresponding stability of pneumatic caisson foundations compared to monopile foundations for offshore wind turbines. The monopile foundation has been the industry standard for years, yet pneumatic caisson foundations are being investigated as a possible alternative. This research applies finite element analysis with the software Plaxis 3D to explore the monotonic and cyclic behaviour of the two foundation types, analysing important properties including soil deformation, energy dissipation, and cyclic stability.

The results of the monotonic behaviour analysis show that caissons are experiencing non-linear soil behaviour at lower forces than monopiles. However, their elastic capacity is sufficient to support the environmental loads, resulting in lower displacements under these loads. Monopiles exhibit greater flexibility, energy dissipation, and a tendency to increase soil stiffness over cycles. At the same time, caissons maintain structural stability with small permanent deformation and low energy dissipation, as demonstrated by cyclic loading tests. Pneumatic caissons demonstrate potential as viable alternatives to monopiles, as they offer increased initial rigidity and reduced displacements. Additionally, the pneumatic caisson foundation can provide a solution in environmentally sensitive areas because the pneumatic caissons can be installed with low noise and vibration impacts on the environment. As the load increases to its maximum capacity, the caisson shows a more abrupt failure compared to the monopile. Beyond the load tipping point, where the caisson shows non-linear behaviour, it undergoes significantly more deformations as force increases. The monopile shows a more gradual increase in deformations with an increase in force. As a result, the monopile shows a more gradual failure behaviour.

Practical challenges in the caisson's production, transportation, and installation need to be overcome. For the production of the big caisson structures, specialised production facilities are required with direct access to the sea. Due to the caisson dimensions used in this thesis, it is too heavy to float and must be transferred using large cranes and barges or semi-submersible vessels. Although this study did not look into it, dimension optimisation or the use of different materials to construct the caisson might save money on transport, particularly if the caisson can float. In order to install the caisson at the correct depth, water must be pumped into its hollow chamber to produce enough downward force to counteract buoyant forces and wall friction.

In summary, the pneumatic caisson foundation offers a viable alternative with advantages in terms of stiffness and lower displacements compared to monopiles. Pneumatic caissons are a promising foundation solution for offshore wind turbines. However, the economic feasibility of the pneumatic caisson method in the offshore environment remains to be examined.

Keywords: Pneumatic caisson, Offshore foundation, Offshore wind turbine, Soil structure interaction, cyclic loading, monotonic loading

Contents

List of Figures

List of Tables

Nomenclature

Abbreviations

Abbreviation	Definition
CPT	Cone Penetration Test
DNV	Det Norske Veritas
FEM	Finite Element Method
FFT	Fast Fourier Transform
GBS	Gravity-Based Structures
HS	Hardening Soil
HSS	Hardening Soil with Small-Strain Stiffness
IEA	International Energy Agency
JONSWAP	Joint North Sea Wave Project
MLE	Maximum Likelihood Estimation
EVA	Extreme Value Analysis
OWT	Offshore Wind Turbine
POT	Peak Over Threshold
PSD	Power Spectral Density
RNA	Rotor Nacelle Assembly
VSF	Volker Staal en Funderingen

Symbols

Symbol	Definition	Unit
E	Young's modulus	[kN/m^2]
V	Velocity	[m/s]
E_{50ref}	Reference secant stiffness modulus	[kN/m^2]
$E_{ur,ref}$	Reference unloading/reloading stiffness modulus	[kN/m^2]
E_0	Initial stiffness modulus	[kN/m^2]
G_0	Initial shear modulus	[kN/m^2]
E_0/E_{ur}	Ratio of initial stiffness to unloading/reloading stiffness	[-]
R_{inter}	Interface strength reduction factor	[-]
M/H	Eccentricity ratio for horizontal force application	[5D]
E_s	Strain energy stored during a cycle	[J]
ΔW	Energy dissipation per cycle	[J]
ξ	Damping ratio	[-]
$G_s(\gamma)$	Secant shear modulus	[kN/m^2]
$G_t(\gamma)$	Tangent shear modulus	[kN/m^2]
α	Rayleigh damping coefficient	[-]
β	Rayleigh damping coefficient	[-]
δ	Dilatancy angle	[deg]
γ	Unit weight	[kN/m^3]
$\gamma_{0.7}$	Shear strain at 70% of maximum shear modulus	[-]
κ	Bulk modulus	[kN/m^2]
λ	Active horizontal soil pressure coefficient	[-]
μ	Friction coefficient	[-]

Symbol	Definition	Unit
ν	Poisson's ratio	[-]
ω	Angular frequency	[rad/s]
ϕ	Angle of internal friction	[deg]
ρ	Density	[kg/m^3]
σ	Stress	[Pa]
ϵ	Strain	[-]

1 Introduction

1.1. Research Context

Offshore wind turbines are a vital part of the world's transition to renewable energy sources. In the upcoming years, there is expected to be a major growth in the demand for offshore wind energy [66]. Recently, the number of wind turbines in the offshore wind sector has been growing. To support these taller structures, longer towers and monopiles with a larger diameter and length have been needed [4]. This trend is likely to continue since the demand for offshore wind energy will increase. For example, the government of the Netherlands raised the target for offshore wind capacity from 11 gigawatts in 2022 to 21 gigawatts by 2030 and it aims to produce between 38 and 72 gigawatts of cumulative offshore wind capacity by 2050 [54]. Figure 1.1 shows the Dutch wind parks that are currently installed and which are planned for installation.

The most used foundations for offshore wind turbines are monopiles [63]. Monopiles represent the most economically viable foundation alternative and are effective at depths of up to 55 meters of water [23]. Monopiles are frequently employed due to their affordability and simplicity of installation in comparison to other foundations. Their design is optimal for transportation, with a straightforward construction process and well-established theoretical foundation [42].

Most monopiles are installed with the technique of impact pile driving. This technique for installing monopiles has significant drawbacks. For example, a 1000-kilojoule hydraulic hammer used for pile driving produces noise levels of about 237 decibels at a distance of one meter. The frequency range of the noise that the hammer blows produces is primarily between 100 and 1000 hertz [31]. The increasing size of these monopiles and driving them to greater depths bring challenges with it. These challenges include assessing and controlling construction peak noise levels and managing noise level exposure [59]. Due to the increasing size of the monopiles, the rated energy range of the hydraulic hammer increases up to 4000 kilojoules, which increases the noise emissions [64].

This noise may kill, hurt, or confuse marine life due to the emerging pressure waves [64]. For example, porpoises stay away from pile driving for an average of 17.8 kilometers. Porpoise avoidance of pile driving has been observed up to 22 km from the drilling site. The behaviour of porpoises may not recover to pre-piling levels for up to two days following the termination of piling noise [11]. According to Bruintjes et al. [14], Spiga, Caldwell, and Bruintjes [58] and Roberts et al. [50] seabream and blue mussels displayed stress indicators as a result of the pile driving. Additionally, pile driving had a similar effect on the sprat and mackerel's swimming and schooling behaviours in juvenile sea bass [30], sprat and mackerel [29], and cod and sole [43].

The pneumatic caisson may offer a less wildlife-intrusive foundation technique. This technique involves constructing reinforced concrete caissons with an internal working chamber near the shore. These caissons are then transported to the desired location. The working chamber is pressurised with air to keep water out during soil excavation. Once the excavation is complete, the caisson will have been submerged to the appropriate depth. The benefits of this technique include vibration-free installation and strong mechanical resistance [2]. Recent developments in remote-controlled immersion and excavation technology have made pneumatically immersed caissons more practical and safe [47].

The purpose of this MSc thesis is to evaluate if utilising pneumatic submerged caissons as the foundation for an offshore wind turbine could be an appropriate alternative to monopile foundations with lower noise and vibration levels.

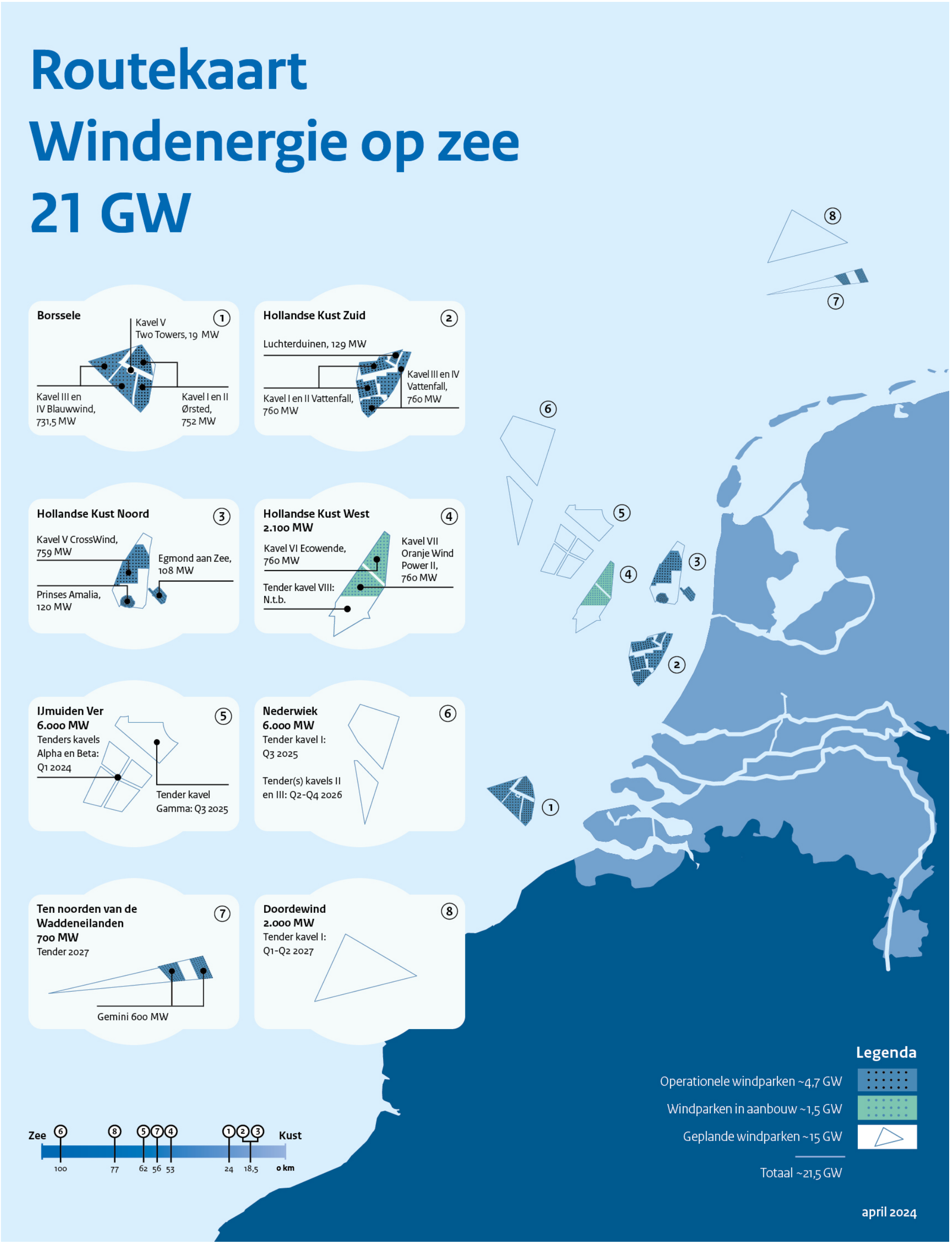

Figure 1.1: Current and planned offshore wind parks in the Dutch North Sea from RVO [53]

1.2. Research Problem

The research problem examined in this thesis is the feasibility of pneumatically submerged caissons as an alternative foundation for offshore wind turbines. This field has not yet been extensively researched, despite its successful implementation in land-based projects such as the Noord-Zuidlijn in Amsterdam and at the inner and outer heads of the sea-lock in IJmuiden. [48]. It is important to examine several critical elements to develop a more thorough knowledge of the offshore implementation of this technique. Initially, it is important to ascertain the most suitable dimensions for the caissons. Furthermore, it is important to identify and resolve any obstacles that may impede their offshore effectiveness. The effectiveness and stability of pneumatic caissons utilised in the offshore environment must also be taken into account concerning the soil conditions. This emphasises the need for a thorough examination of pneumatically submerged caissons as offshore wind turbine foundations.

The caissons' capacity to endure the various, severe, and cyclic loads experienced offshore, such as wind, waves, and currents, as well as logistical difficulties like fabrication and transportation, is still uncertain. Although there is a numerous amount of information regarding offshore wind turbine foundations, there is a knowledge gap regarding the suitability and functionality of pneumatic caissons in offshore environments.

1.3. Research Objective

This thesis aims to investigate the geotechnical technical aspects of pneumatic caissons for offshore wind turbine foundations in order to determine their overall viability and potential obstacles, as well as to identify the obstacles that must be overcome in order to be a viable alternative to a monopile foundation. The objective is to fill this knowledge gap and provide new perspectives to the field of offshore foundations.

1.4. Research Questions

To be able to reach the stated research objective the following research question together with corresponding sub-questions have been formulated.

Research question:
To what extent is a pneumatically submerged caisson a viable and feasible alternative as a foundation of an offshore wind turbine compared to the monopile foundation?

In order to answer the research question, a series of sub-questions were formulated:

- What are the forces acting on the wind turbine that are transmitted to the foundation, and what is the magnitude of these forces?
- What is the structural response of the combination of the wind turbine and its foundation under the applied forces?
- What is the monotonic behaviour of the soil as a result of the forces applied to the structure?
- What is the cyclic behaviour of the soil as a result of the forces applied to the structure?
- What obstacles must be addressed concerning the production, installation, dismantling, and reuse of the pneumatic caisson to serve effectively as a foundation, and what potential solutions exist for these obstacles?

1.5. Research Scope

This MSc thesis is concentrated on the interactions between soil and structure concerning a monopile and a pneumatic caisson as foundations for an offshore wind turbine. Due to the time constraints, the design of the caisson is conducted at a preliminary stage and relies on some assumptions. The objective is to determine the preliminary dimensions of the caisson based on the analysis conducted in this thesis and assess how realistic these dimensions are. The specific design of the caisson and the interface between the caisson and the transition piece fall outside the scope of this thesis.

The interactions between soil and structure are assessed during the operational phase of the caisson. The caisson and monopile are examined with respect to their monotonic and cyclic load behaviour. The installation phase, wherein the caisson will be positioned into the seabed, is not included within the scope of this thesis.

1.6. Research Outline

This section describes the outline of this thesis. This study includes nine chapters, each of which is briefly described below. The literature review chapter reviews existing literature on offshore foundations, pneumatic caissons, and offshore wind turbines and introduces key environmental load factors. Also, the theories necessary for calculations made in this thesis are described, including theories about wave and wind loads, soil models, and dynamic system analysis. In the research methodology, the research approach is detailed. The chapter on input parameter determination for the numerical model covers site selection, CPT interpretation, and the calculation of the input parameters for the Plaxis 3D software for modelling and analysing the soil structure interactions. The numerical model chapter discusses the setup of numerical simulations, including the choices made for setting up the models, mesh sensitivity, and the application of the staged construction phases. In the results chapter the results of the different analyses are discussed and reflected on. The Practical Considerations in the Construction and Installation of the Caisson Chapter explores the construction, transport, and installation challenges of caisson foundations. In the conclusion, key insights are summarized. The final chapter, the discussion, addresses uncertainties and limitations in the study, offering reflections on this study and making recommendations for future research and practical applications.

2 Literature Review

In this chapter, the theoretical background and theory required for this thesis are covered. First, a reflection on the different types of offshore wind turbine foundations will be given. Next, a more detailed explanation of the pneumatic caisson method will be given together with general information about the production, transportation, installation, and decommissioning. Furthermore, the theories necessary to determine the forces on the offshore wind turbine and its foundation will be elaborated on. These are theories about the JONSWAP spectrum, Morison's equation, linear wave theory, and the aerodynamic loads acting on the structure. Furthermore, the theory behind the Hardening Soi Small Strain Model will be covered, whereafter the wind turbine as a dynamic system and the relevance of the natural frequency of the system will be elaborated on. The chapter ends with information about the Fast Fourier Transform and the logarithmic decrement method.

2.1. Offshore Foundations

In order to highlight the importance of investigating new foundation types for offshore wind turbines, it is important to identify the deficiencies of existing techniques. Through an investigation of these deficiencies, one can gain a deeper understanding of the constraints imposed by current techniques and highlight the need for new methods.

The most used foundation types are:

- Monopile foundation
- Jacket foundations
- Suction buckets foundation
- Gravity-Based Structures (GBS)

In Table 2.1 an overview of the advantages and disadvantages, as well as the typical depths at which the four foundation types are installed, are given.

Table 2.1: Comparison of the four offshore wind turbine foundation types

Foundation type	Advantages	Disadvantages	Typical depths [m]
Monopile	• Simple design • Adaptable • Established supply chain • Low cost	• Limited to certain seabed types • Limited depth range	5 - 55
Jacket/Tripod	• Suitable for deeper waters • Less steel than monopiles • Advanced fabrication	• Higher cost • Complex production and installation • Requires piles	40 - 100
Gravity-Based	• Low noise installation • No piling needed • Corrosion-resistant • Utilizes local labour and materials	• High cost in deep water • Large construction facilities needed	15 - 40
Suction Bucket	• Cost-effective • Easy decommissioning • Quick and noiseless installation	• Relatively new • Site-specific constraints	5 - 50

In figures 2.1a and 2.1b a schematisation of the four foundation types is given.

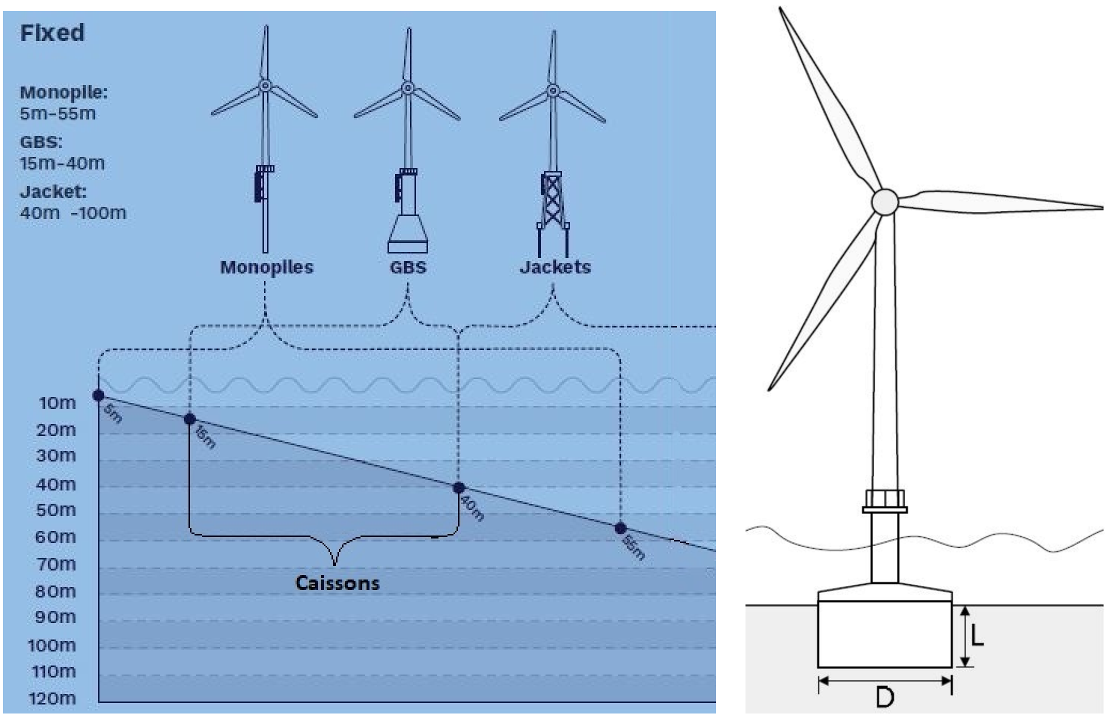

(a) Overview of the three foundations types [23]

(b) Suction bucket foundation [32]

Figure 2.1: An overview of the four most common bottom founded foundations for offshore wind turbines

In the following subsections, each foundation type will be briefly elaborated on.

Monopile Foundation

Steel monopile foundations are currently used in more than 60% of offshore wind installations around the world [65]. The main advantages of monopiles are simplicity and adaptability. The most common design has been a cylindrical monopile driven into the seabed first, followed by a cylindrical transition piece mounted over it and grouted into place. A circular foundation is more easily designed and analysed compared to other types. Also, the technology is well-established and has an advanced supply chain. It can be mass-produced and transported using existing vessels [23]. The transition piece is designed to allow access and level the tower base interface. Increasingly large designs, with XL units weighing up to 2.000 tonnes or more, are now being deployed in deeper waters of 60-70 meters [65]. In general, the depth ranges from about 5 to 55 meters [23].

Monopiles are currently used in almost all European developments due to their relatively low cost and ability to be hammered or vibrated deeply into the seabed. Monopiles can be installed in seabeds consisting of sand, silt, medium to hard clays, or a combination of these. However, some parts of the world with promising areas for offshore wind energy lack a suitable seabed. Here, the soil layers consist of soft marine clays, hard volcanic and sedimentary rocks, and loose deposits with liquefaction potential. This means that in some cases, alternative foundations are required, such as piled jackets, suction buckets, or gravity-based structures [65].

Jacket foundation

Jacket structures are widely used in the oil and gas sector due to their ability to withstand diverse geotechnical conditions and their ability to operate in deeper waters. These features also make the jacket suitable as a foundation for offshore wind turbines. Jacket structures are stiffer and require less steel than monopiles in deeper water locations [23]. The design of jackets includes a transition piece platform at the top, while the main structure is made up of legs and braces. The structure is established on the seabed through the utilisation of piles. It could have either four or three legs [65]. Jackets require a greater investment of time and resources in their production and installation processes when compared with monopiles. Recent advancements in fabrication enable more reliable serial production for large-scale projects. Typical depths for jacket structures range from 40 meters to 100 meters. Jacket structure can be combined with a suction caisson anchoring system, resulting in quieter and faster installments[23].

Gravity-Based Structures

Gravity-Based Structures (GBS) are the oldest and most basic foundation type. These structures rely on the weight of the concrete base for stability [23]. Gravity-based structures are built onshore and installed without the need for piling. This results in lower noise levels during installation. This can avoid some of the noise restrictions that some projects are facing to limit the impact on marine mammals [65]. Manufacturing requires large quayside or dry dock facilities with heavy lifting capabilities. These are made of concrete or steel-concrete hybrids. Gravity-based structures, which do not require piles or specialised installation vessels, make the best use of both local labour and materials [65]. When installed in deep-water sites gravity-based structures are more costly due to the high volume of materials required for depths greater than 35m. An advantage is that the concrete foundations are being resistant to corrosion. Depths typically range from around 15 to 40 meters [23]. An overview of the different bottom-founded foundations, monopiles, jackets, and gravity-based structures can be found in Figure 2.1a.

An example of gravity-based foundations that were transported floating is the Blyth wind farm, one kilometer off the coast of Blyth in England. The installation was shown to be more cost-effective than a drilled foundation in the seabed. Five wind turbines, each with a tip height of 191.5 meters and a production capacity of 8.3 MW, have been installed utilising this foundation [8].

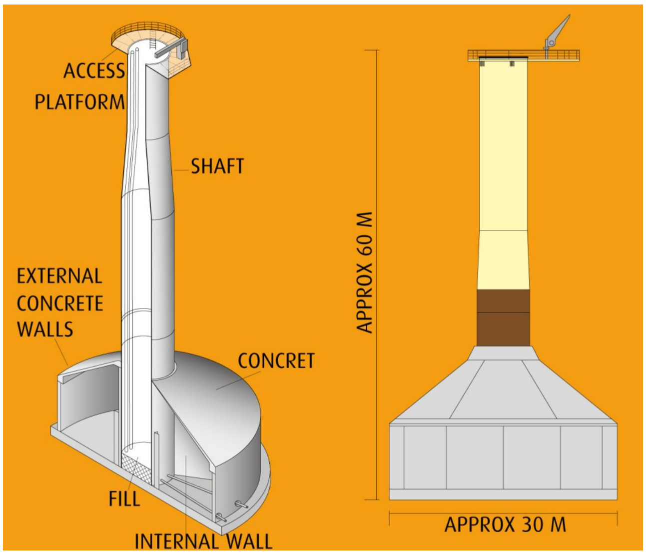

Figure 2.2: Concrete base for offshore wind turbines off the coast of Blythe from *Betonvoet voor windturbines op zee* [7]

It is expected that the pneumatic caisson foundation will have properties comparable to those of the gravity-based foundation. elements like dimensions, materials, and the connection with the transition piece with the foundation structure. Consequently, the installation of the pneumatic caisson foundation should be considered in a manner comparable to that of a gravity-based foundation.

Suction Bucket Foundation

The suction bucket foundation is a relatively new form of foundation used in the offshore wind sector. The suction bucket creates a hoover that secures the foundation to the sea floor. This foundation has the potential to save costs because of its mono-tubular design. This design is relatively inexpensive to fabricate, approximately three times less expensive than jackets. Pumping air back into the bucket reverses the suction process and helps to remove the structure, which makes future decommissioning easier. Furthermore, suction bucket foundations offer quick and noiseless installation. Suction buckets allow for single-piece installation up to the work platform. Suction buckets are gaining popularity as foundation for offshore wind turbines due to their relatively low installation costs and minimal impact on wildlife [65]. A sketch of an wind turbine founded on a suction bucket foundation can be seen in Figure 2.1b. This method is expected to share similarities with the pneumatic caisson in terms of deployment and stability.

2.2. Pneumatic Caissons

In this section, the technique of pneumatically sinking of caissons will be further elaborated upon. First, an outline of the pneumatic caisson method will be given. Secondly, the principle behind the method will be briefly discussed. Lastly, the installation of the caisson will be discussed.

Outline of the Method

The pneumatic sinking of caissons can be seen as a method of transporting a structure vertically through the ground. Particularly, in civil engineering for the realisation of underground structures. This method involves constructing reinforced concrete caissons with a designated working space for excavation, where groundwater is pushed out of the working space by pumping compressed air at a pressure corresponding to the hydraulic head immediately below the caisson to facilitate continuous excavation and sinking of the caisson in a dry environment [3]. The construction process typically entails multiple rounds of excavation, and sinking until the desired depth and soil support are achieved [19]. After the desired depth and support are reached the working space will be filled with concrete. In Figure 2.3 an example of a pneumatic caisson configuration is given.

Common applications of the pneumatic caisson method, according to Oyake et al. [46] include:

- Foundations for bridges, viaducts and dams

- Pumping stations and underground water discharge reservoirs
- Working shafts or launch shafts for machines used in tunnel boring
- Subterranean train stations and tunnels for urban transportation
- Facilities for energy and electricity storage
- Seawalls, quay walls, and port facilities

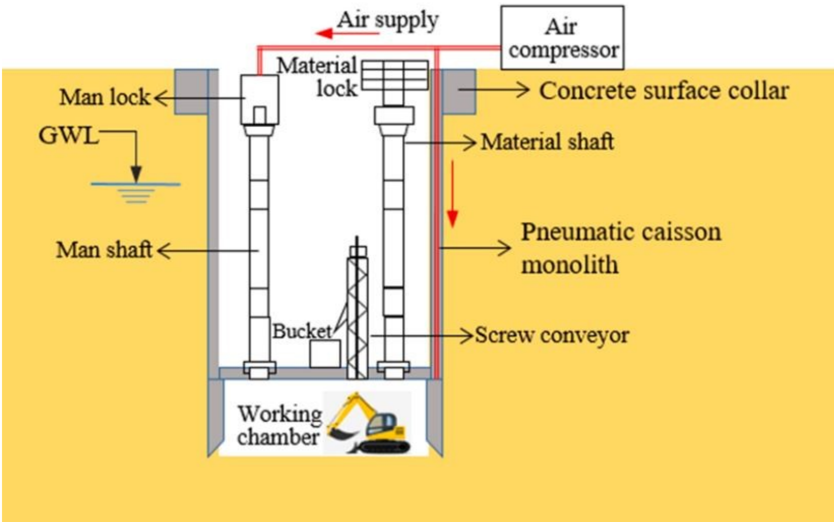

Figure 2.3: Pneumatic caisson-sinking from Lai et al. [39]

Principle of the Method

The pneumatic caisson method works according to the same principle as that of turning a glass upside down in water. The air pressure in the glass prevents the water from entering. When extra air pressure is created in the glass, the water will be pushed out to a level where there is an equilibrium between the water pressure and the air pressure. Similarly, an airtight working space is created at the bottom part of the caisson. Pumping air in the working space will prevent groundwater from entering the working space and allow for excavations in a dry state. The working space is enclosed by the cutting edges of the caisson, similar to the edge of the glass [19]. In Figure 2.4 this concept is visualised. The air pressure increases proportionally with the caisson's depth, aligning with the hydraulic head of water directly beneath it.

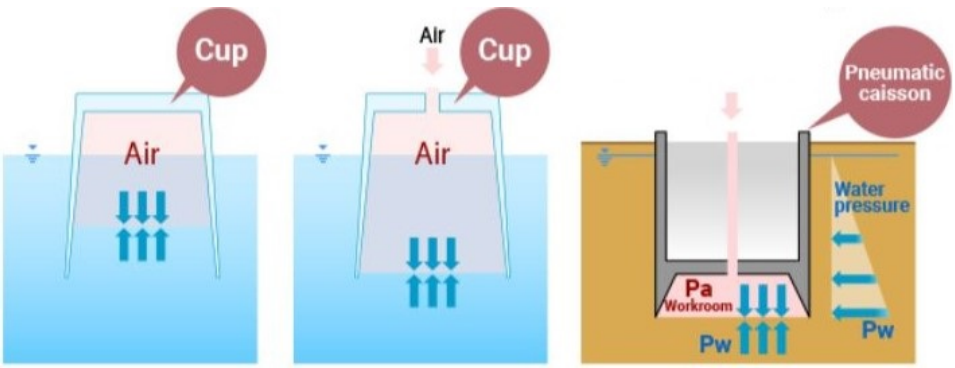

Figure 2.4: Schematisation of the principle, adapted from Daiho Corporation [19]

Utilising air overpressure to establish a dry working space beneath the caisson constitutes the primary characteristic of this method. The secondary principle is the process of caisson sinking. When the soil is excavated under the caisson the weight pressure on the remaining soil, which is the support berm, increases. As a result, every time the failure-bearing capacity is reached, slip circles form, causing the caisson to sink several centimeters [3]. This process unfolds gradually: initially, the slope of the ground berm steepens through excavation at its toe. Substantial deformations along the berm's sliding surface result in temporary loss of caisson support, as can be seen in region I of Figure 2.5. Activation of deeper sliding surfaces, induced by the interaction between the cutting edge of the caisson and the remaining ground berm, initiates caisson sinking. This can be seen in region II in Figure 2.5 Following minor settlement, the caisson floor finds support on the deformed ground berm/slope, relieving pressure on the deeper sliding surfaces and preventing further sinking. By continuing excavation at the slope's toe, the deformation resumes and the process will start again. This incremental deformation process drives sinking under stress conditions nearing collapse [2].

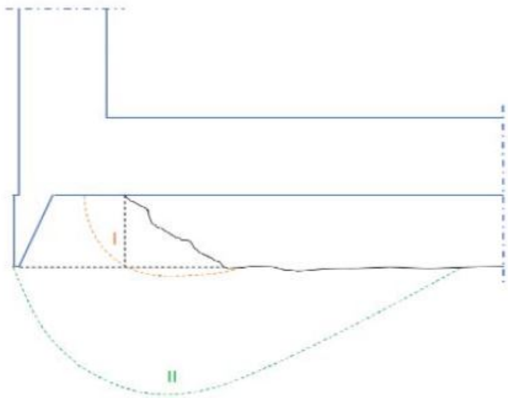

Figure 2.5: Failure mechanism of the berm in the working space from Admiraal and Feddema [2]

Installation of the Caisson

A pneumatic caisson is constructed as a closed box at surface level. First, the bottom of the caisson is constructed together with the cutting edges. Hereafter, the remaining of caisson structure can be built [10]. Until at least the 1930's personnel excavated the ground beneath the caisson with shovels and buckets. Nowadays, remote-controlled water jets and excavators are used to remove the ground beneath the caisson [3]. Shafts need to be installed to be able to install this equipment and then remove the excavated soil from underneath the caisson. Also, an airlock and compressors need to be installed to make sure the pressure underneath the caisson remains on the required level. After the caisson is sunken in the right place, the equipment will be removed and the working space will be filled up with concrete. In the offshore environment, it is unlikely that the working chamber will be filled with concrete after the caisson is brought to depth. This is because of the high volume of concrete that would be needed to fill the working chamber and the impracticalities that come with the production and transport of the concrete offshore. It is most likely the working chamber of the caisson will be filled with sand when utilised in the offshore environment. This would also be more favourable for the possible decommissioning of the caisson after its lifetime. In Figure 2.6 a schematisation of the installation process is shown.

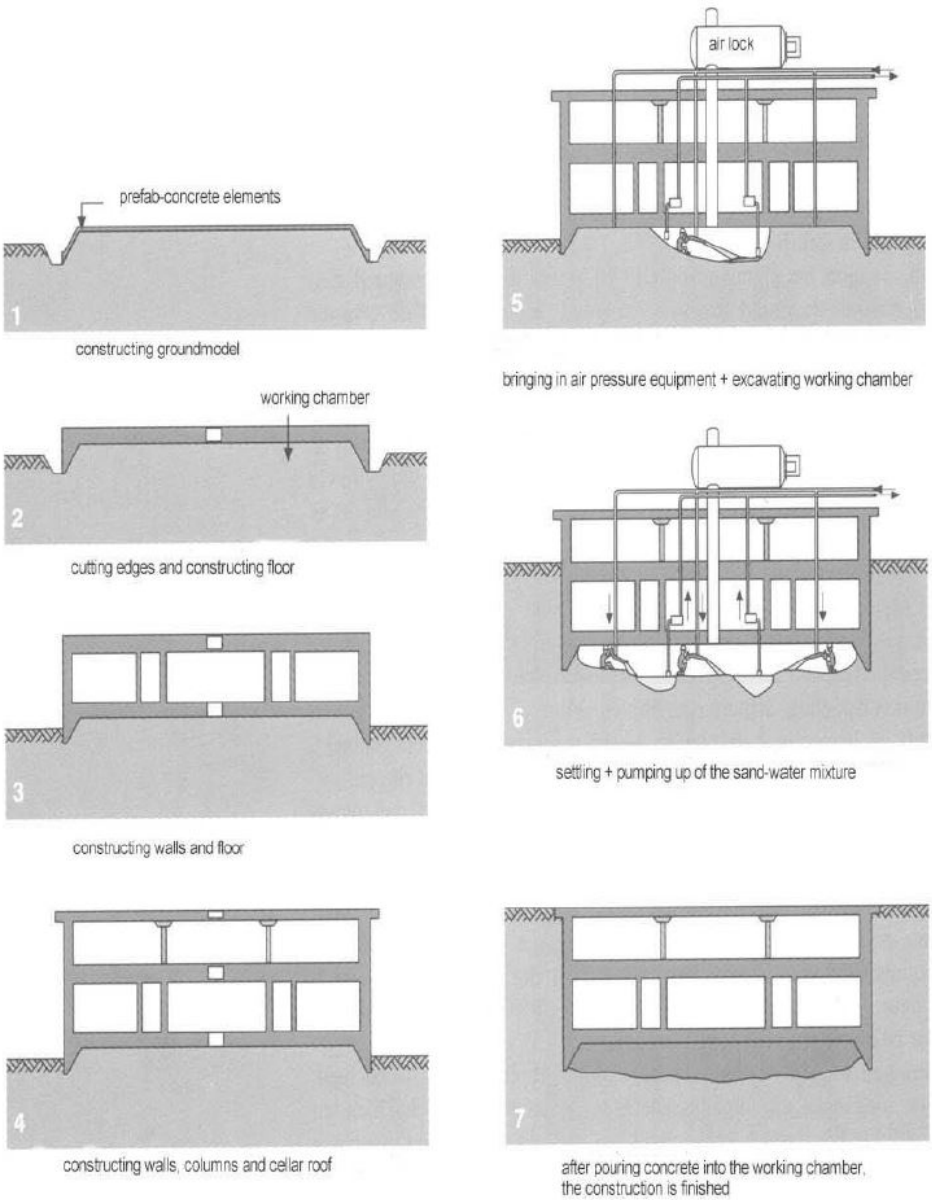

Figure 2.6: Schematised phases during excavation of pneumatic caisson from Bosch, Arends, and Broere [10]

Often a bentonite solution is injected along the caisson surfaces to reduce the lateral friction between the caisson and the soil. The resisting forces at the cutting edges of the caisson are reduced by excavating the soil beneath the caisson from within the working chamber [46].

The air pressure in the working chamber, also known as workload, is adjusted to balance pore water pressure. During caisson construction, the air pressure is typically 1.5 kPa higher than the pore pressure to prevent leakage into the working chamber [47]. Also, the compressed air is working on the floor of the working chamber. This pressure ensures that groundwater is not excluded from the underground around the pneumatic caisson. No seepage force is generated towards the floor of the working chamber, nor is the water level in the ground surrounding the Caisson affected. Therefore, the groundwater flow is not disturbed. Another advantage of the compressed air in the working chamber is that the pressure also causes an upward response force on the working chamber's roof slab. This results in a more evenly distributed caisson weight load over the structure. Therefore, the magnitude of the reaction forces under the cutting edge decreases, and the surrounding soils are less affected [46].

2.3. Production

2.3.1. Production Site

The production site of the caisson needs to have enough space to be able to construct a large number of caissons. Also, the production site needs to have direct access to open water and a suitable connection to the sea to be able to transport the caissons. Three possible production sites have been found based on a conversation with Admiraal [1]: the Verolme shipyard at the Port of Rotterdam, the Bougainville yard in the Grand Port Maritime of Le Havre, and the construction dock at Barendrecht.

The Verolme shipyard at the Port of Rotterdam features multiple dry docks of various lengths and capabilities. One dry dock measures 230 meters in length, 34.4 meters in internal width, and has a maximum draft of 8.0 meters. The dry dock features two cranes, each capable of lifting 20 tonnes. Another dry dock measures 275 meters in length, 40.36 meters in internal width, and has a maximum draft of 10.3 meters. The dock is equipped with two cranes, one capable of lifting 20 tonnes and the other 40 tonnes. Lastly, a third dry Dock, the largest dry dock, measures 405 meters in length, 90 meters in internal width, and has a maximum draft of 11.6 meters. This dock features three cranes with lifting capacities of 20 tonnes, 30 tonnes, and 80 tonnes, respectively [20]. These docks would provide sufficient space to construct the caissons.

The Bougainville yard in the Grand Port Maritime of Le Havre, France, could be another production site for the caissons. The 71 gravity-based foundations for the 500 MW Fécamp offshore wind farm have been constructed and put onto a cargo barge at this yard. This indicates that it is possible to construct big concrete offshore foundations at this yard. Each foundation had a mass of 5000 tonnes and a base diameter of 31 meters, with heights varying from 48 to 54 meters depending on the installation location [41]. This yard offers sufficient facilities to produce the caissons.

Lastly, the construction dock at Barendrecht, situated on the Oude Maas, could be an option the produce the caisson. The construction dock is a facility engineered for the fabrication of components for immersed tunnels. This construction port covers approximately 10 hectares, offering sufficient room for the fabrication of substantial tunnel components. The construction dock offers convenient access to the Oude Maas river. A trench 35 meters deep was dug around the dock. The dock has a depth of 10 meters. The construction pier in Barendrecht has a significant history and has been utilised for the production of several major tunnel projects, including the Heinenoord Tunnel, the Second Coentunnel, and the Second Beneluxtunnel. These projects show the significant size of construction that can be produced at this yard [5]. Therefore, this could be a place for the construction of the pneumatic caissons.

Figure 2.7 shows a sketch of the caisson that is modelled in this thesis. This sketch shows a simplification of the different parts, the caisson itself, the cutting edge, and the transition piece that is connected to the caisson and on which the wind turbine will be mounted.

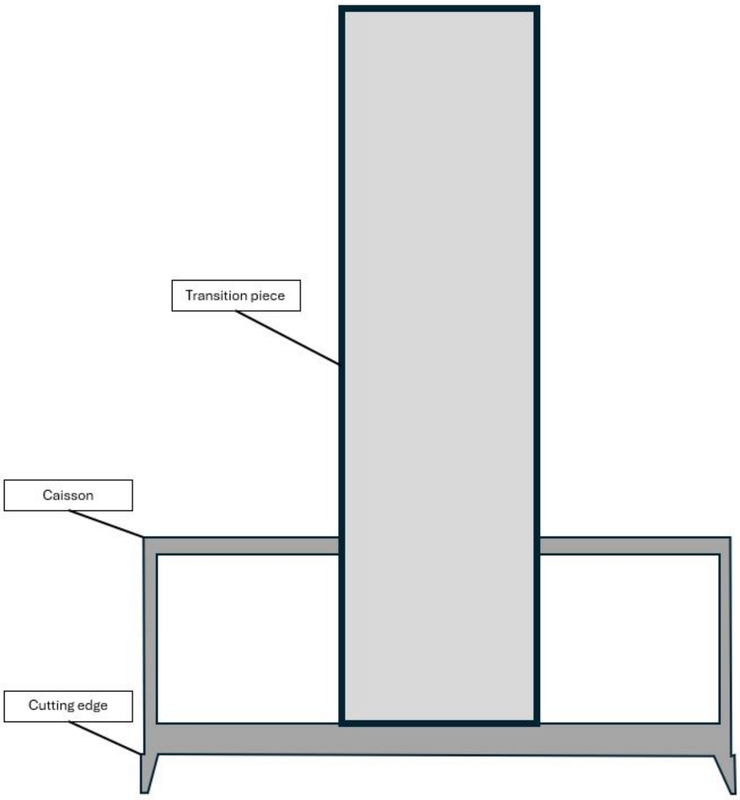

Figure 2.7: Sketch of the pneumatic caisson

2.3.2. Installation of the Equipment

Two shafts for passenger lifts and one for a material lift are necessary, together with a stair tower. One passenger shaft serves as an access route, while the other operates as an escape route. Passages for dredging equipment, the dredging robot and water jets for excavation are necessary, ideally located on the interior of the transition piece. In Figures 2.8 and 2.9 a cross-section and a top view of the caisson and the equipment that is required to sink the caisson into place can be found.

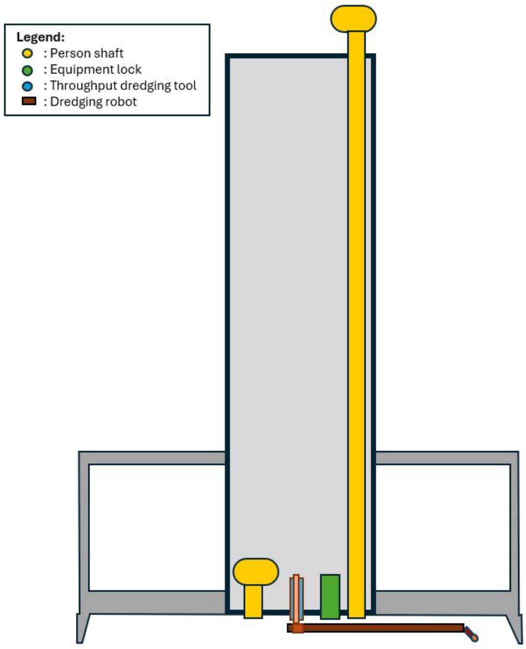

Figure 2.8: Cross-section of the caisson with an overview of the required equipment for installation

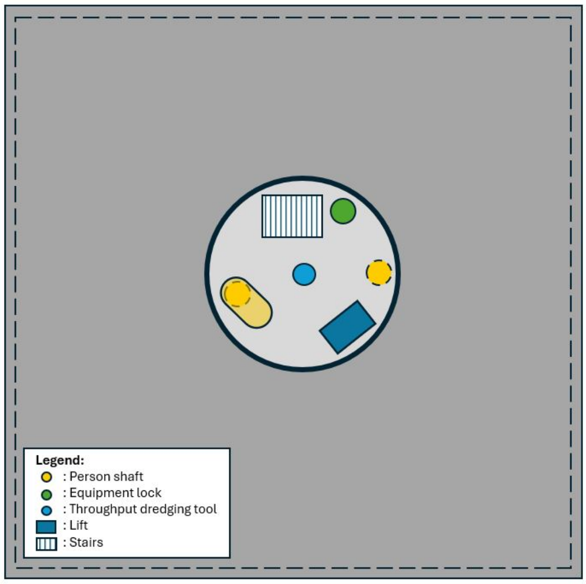

Figure 2.9: Top view of the caisson with an overview of the required equipment for installation

2.4. Transport

Multiple techniques exist for the transportation of substantial offshore structures. One common method is to float the caisson and then use tugboats to tow it to the destination. This method makes use of the caisson's natural buoyancy, making transfer relatively straightforward and inexpensive. An alternative approach would be the transportation of caisson with barges. This method provides better control and stability when travelling, especially in rougher sea conditions. However, when transporting the caisson on a barge, a heavy lift crane is needed to lift the caisson of the barge onto the seabed. The last transportation discussed is transportation via a semi-submersible ship or barge. After transporting the caisson to the desired location offshore, the semi-submersible vessel can partially immerse. The buoyant force of the caisson in the water prevents the use of costly heavy lift cranes, and smaller cranes can be used due to the lowering of the force that is needed for lifting up the caisson. Each technique has particular advantages and disadvantages, and the choice of transport method depends on factors like the distance from the offshore location, the weather, and the availability of transport equipment, all of which must be taken into account.

2.4.1. Decommissioning

Most of the time, the monopile is cut off near the seabed. The embedded part of the monopile remains in the seabed. This is now the most economical and environmentally friendly way. It would be possible to decommission the caisson after its lifetime is surpassed. Decommissioning requires the workroom to be emptied again. The sand in the working chamber can be dissolved in water and sucked out of the chamber. The vertical equilibrium should be tipped upward to lift the caisson out of the seabed. This can be done by pumping out the water from the caisson's hollow section and pressurising the working chamber again to lift the caisson [1].

2.5. Offshore Wind Turbine

At the time this thesis was written, there were ten active wind farms in the Dutch North Sea that generate approximately 4.7 GW of electricity [55]. In Table 2.2 an overview can be seen of the installed wind farms.

Table 2.2: Current installed wind turbines in the Dutch North Sea from RVO [55]

Name wind farm	**In use since [Year]**	**Amount of turbines [-]**	**Turbine output [MW]**	**Wind farm output [MW]**
Hollandse Kust Noord	2023	69	11	759
Hollandse Kust Zuid	2023	139	11	1529
Borssele I and II	2020	94	8	752
Borssele III and IV	2020	77	9.5	731.5
Gemini windpark	2016	150	4	600
Luchterduinen	2015	43	3	129
Prinses Amalia Windpark	2008	60	2	120
Egmond aan Zee (OWEZ)	2007	36	3	108

There are several new wind farms planned in the Dutch North Sea. However, the details about the amount of turbines and individual turbine output for most of the new wind farms are still unknown. For the planned wind farm ”Hollandse Kust (west)” the details are known. The wind farm is expected to be operational in 2025 or 2026. The total wind farm production is estimated to be 1516 MW, generated by 108 14-MW wind turbines.

For this thesis, a reference turbine has been chosen to make the necessary calculations. As reference turbine, the ”IEA Wind 15-Megawatt Offshore Reference Wind Turbine” has been chosen. Gaertner et al. [27] wrote a report with the motivation to provide design standards and open benchmarks for future research into new innovations and design methodologies. The report describes a 15-megawatt offshore wind turbine with a hub height of 150 meters and a rotor diameter of 240 meters that is supported by a fixed-bottom monopile foundation [27]. Based on the trend that can be seen in Table 2.2 of increasing wind turbine output, a wind turbine with an output of 15 MW is seen as realistic for the near future.

In Table 2.3, the key parameters of the wind turbine are shown. These parameters will be used for the calculations further on in this thesis. In Figure 2.10 a schematisation of the reference turbine is shown.

Table 2.3: Key parameters for the IEA 15-MW reference turbine from Gaertner et al. [27]

Parameter	Units	Value
Power rating	MW	15
Turbine class	-	IEC Class 1B
Specific rating	W/m^2	332
Rotor orientation	-	Upwind
Number of blades	-	3
Control	-	Variable speed
	-	Collective pitch
Cut-in wind speed	m/s	3
Rated wind speed	m/s	10.59
Cut-out wind speed	m/s	25
Design tip-speed ratio	-	9
Minimum rotor speed	rpm	5.0
Maximum rotor speed	rpm	7.56
Maximum tip speed	m/s	95
Rotor diameter	m	240
Airfoil series	-	FFA-W3
Hub height	m	150
Hub diameter	m	7.94
Hub overhang	m	11.35
Rotor precone angle	deg	-4.0
Blade prebend	m	4
Blade mass	t	65
Drivetrain	-	Direct drive
Shaft tilt angle	deg	6
Rotor nacelle assembly mass	t	1,017
Transition piece height	m	15
Monopile embedded depth	m	45
Monopile base diameter	m	10
Tower mass	t	860
Monopile mass	t	1,318

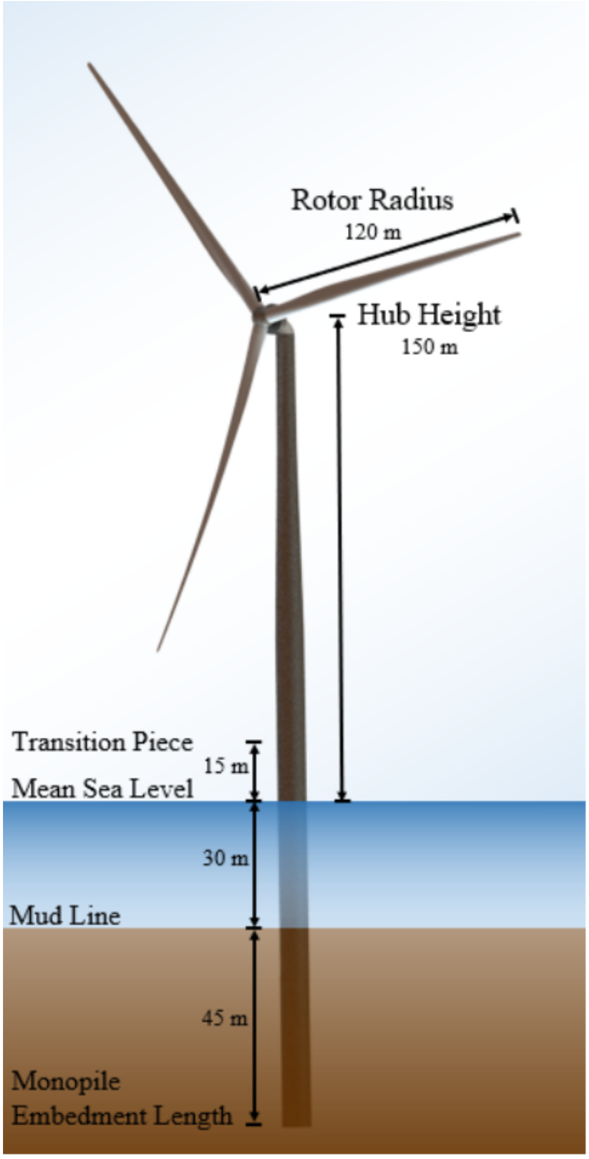

Figure 2.10: The IEA 15-MW reference turbine from Gaertner et al. [27]

2.6. JONSWAP Spectrum

Joint North Sea Wave Project (JONSWAP) spectra are an empirical connection that characterises the ocean's energy distribution with frequency and are a key advance in the understanding and modelling of ocean wave spectra [17]. This spectrum offers a more accurate representation of the energy distribution in wind-generated waves, particularly in the North Sea, and was developed from extensive field data collected during the JONSWAP project. By adding more parameters to account for the peaking of the wave spectrum observed in fetch-limited waters, the JONSWAP spectrum improves on the previous Pierson-Moskowitz spectrum [28].

The spectral density function $S_j(\omega)$, which describes the distribution of wave energy across different frequencies, gives the mathematical description of the JONSWAP spectrum. The JONSWAP spectrum's general form can be found in equation 2.1.

$$S_j(\omega) = \frac{\alpha g^2}{16\pi^4}\,\omega^{-5}\,exp[-\frac{5}{4}(\frac{\omega_p}{\omega})^4]\,\gamma^r \tag{2.1}$$

Where:

- $\alpha =$ the Phillips constant
- $\omega =$ the angular frequency
- $\omega_p =$ the peak frequency
- $\gamma =$ the peak enhancement factor
- $r =$ defined in equation 2.2

$$r = exp[-\frac{(\omega-\omega_p)}{2\sigma^2\omega_p^2}] \tag{2.2}$$

Where σ is a parameter that controls the peak's width. In order to reflect the increased energy concentration observed in real sea states, the JONSWAP spectrum adds the peak enhancement factor γ, which increases the spectral density near the peak frequency [28].

The coefficients α and γ are empirical values. Typically, α is approximately 0.076, which is shown by equation 2.3.

$$\alpha = 0.076(\frac{U_{10}^2}{Fg})^{0.22} \tag{2.3}$$

Where F is the fetch length and U_{10} is the wind speed at 10 meters above the sea surface. For North Sea conditions, the peak enhancement factor γ typically has a value of 3.3, but it can range from 1 to 7 [28].

The JONSWAP spectrum is especially helpful for engineering applications where precise wave modelling is essential, such as designing offshore structures. It gives a better understanding of the sea condition by taking into account the non-linear wave growth as well as the effects of fetch and wind duration. The spectrum is more accurate than the Pierson-Moskowitz spectrum for fetch-limited conditions because it can recreate the peak position of the wave energy distribution [28].

The JONSWAP spectrum is frequently used in real-world applications to generate artificial time series of sea surface elevations. Summing sinusoidal components with amplitudes a_j and random phases ϵ_j is how this is accomplished. This is shown in equation 2.4.

$$\eta(t) = \sum_{j=1}^{N} a_j \sin(\omega_j t + \epsilon_j) \tag{2.4}$$

Here the amplitudes a_j are derived from the spectral density function as in equation 2.5

$$a_j = \sqrt{2S(\omega_j)\Delta\omega_j} \tag{2.5}$$

This method allows the simulation of realistic sea states for a variety of engineering enquiries, such as the evaluation of wave-induced motions and the assessment of wave loads on offshore structures Tucker, Challenor, and Carter [60].

Important for the design of an offshore wind turbine and its foundation is the peak in the JONSWAP spectrum. Since this is the main excitation frequency of the wave loads on the structure and should not coincide with the natural frequency of the structure. Based on the wave data of the location where the caisson will be constructed, the JONSWAP spectrum can be constructed.

2.7. Forces on the Structure

Multiple forces are active on an offshore wind turbine. The most dominant forces are the wave, current, and aerodynamic loads. This section explains how these forces are calculated.

2.7.1. Hydraulic Loads

Hydraulic loads on a structure come from the interaction of waves and currents with the structure. The diameter of a structure, the wave height, and the wavelength determine which flow regime should be used to calculate the loads and therefore how the forces on the structure are calculated. These regimes are seen in Figure 2.11. For slender structures such as an offshore wind turbine regime 2, the diffraction region, will most likely not be used since the diameter is small compared to the wavelength. If an object falls in this regime, diffraction theory should be used to calculate the wave forces [16]. For all other regimes, the Morison equation can be used. The Morison equation takes into account two main contributors to calculate the hydraulic load, the drag force and the inertia force. Depending on the wave height the inertia part, drag part or both should be used. Equation 2.6 shows this Morison equation.

$$F_{Morison} = \frac{1}{2}\rho_w C_d D u|u| + \frac{1}{4}\pi D^2 C_m \rho_w \dot{u} \tag{2.6}$$

Here ρ_w is the water density, C_d is the drag coefficient, D is the diameter, u is the wave velocity, C_M is the mass and the added mass coefficient, sometimes noted as $(m+C_a)$ and $\dot{u}$ is the wave acceleration.

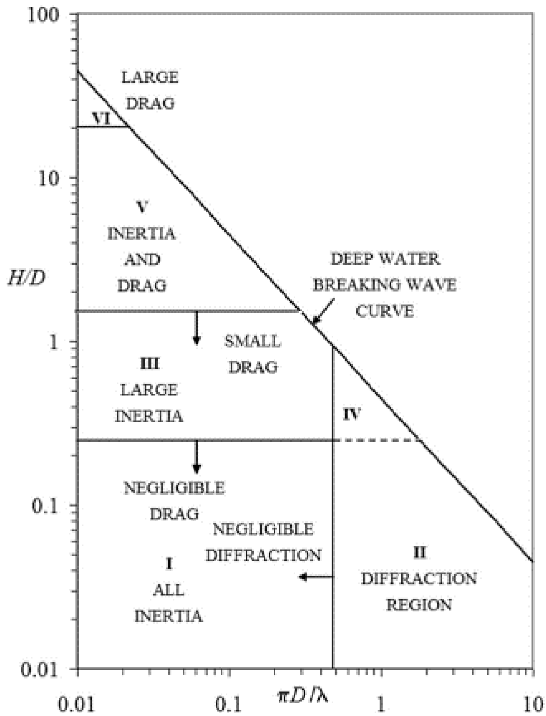

Figure 2.11: Force regimes from [16]

2.7.2. Linear Wave Theory

In this thesis, the waves are assumed to be regular. The wave velocity and acceleration necessary for Morison's equation are determined by using Airy's linear wave theory. This is a simplification of reality, but this simplification is sufficient for determining the preliminary wave forces on the structures assessed in this thesis [35]. Linear wave theory is typically used to describe ocean waves that have a small amplitude relative to their length. The wave kinematics can be represented by the linear wave theory, also known as the Airy theory. The regular wave theory assumes that the wave is sinusoidal. In offshore technology, the Airy theory is frequently employed. The theory is a first-order wave theory, sometimes referred to as linear or small-amplitude wave theory. Airy theory is frequently used to estimate wave behaviour in engineering applications since it has been demonstrated to provide reliable approximations of the kinematics and dynamic features of ocean waves [35]. An overview of the linear wave theory is shown in Figure 2.12.

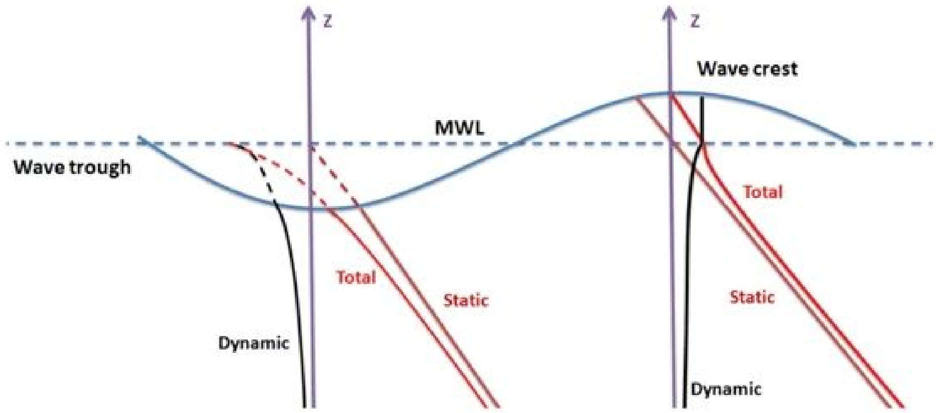

Figure 2.12: Overview of the linear wave theory from Karimirad [35]

The wave velocity and acceleration of the propagating waves are determined based on equations 2.7 and 2.8 respectively.

$$u = \omega\zeta_a \frac{\cosh k(z+h)}{\sinh kh} \cos(kx - \omega t), \tag{2.7}$$

$$\dot{u} = \omega^2\zeta_a \frac{\cosh k(z+h)}{\sinh kh} \sin(kx - \omega t), \tag{2.8}$$

Equations 2.9 and 2.10 are used to formulate the associated velocity potential and dispersion relation, respectively.

$$\phi = \frac{\omega\zeta_a}{k} \frac{\cosh k(h+z)}{\sinh kh} \cos(\omega t - kx), \tag{2.9}$$

$$\omega^2 = gk \tanh kh, \tag{2.10}$$

In the equations above, k is the wave number, z is the observation depth, h is the water depth, ω is the angular frequency, t is the observation time, x is the observation space, ϕ is the velocity potential and ζ is the wave elevation according to the Airy wave theory and is calculated with equation 2.11.

$$\zeta = \zeta_a \cos(kx - \omega t) \tag{2.11}$$

Where $\zeta_a =$ the amplitude of the wave.

The Airy wave theory is applicable only up to the mean seawater level (MSL) and unable to characterise the wave kinematics above this level. It is important to define wave kinematics above the water surface up to the wave crest to determine the wave loads. A commonly used method to determine the wave kinematics is the Wheeler stretching method [35].

$$z' = d\left(\frac{d+z}{d+\zeta} - 1\right) \tag{2.12}$$

Where z' is the new z-coordinate in the Wheeler stretched model, d is the water depth and z is the coordinate of the observation depth in the original coordinate system.

In Figure 2.13 the Wheeler stretched profile is shown compared to the Airy wave profile. The stretched profile goes up to the wave crest, where the Airy wave profile stops at MSL. The stretched profile allows to take the elevation above the MSL into account when the forces are calculated.

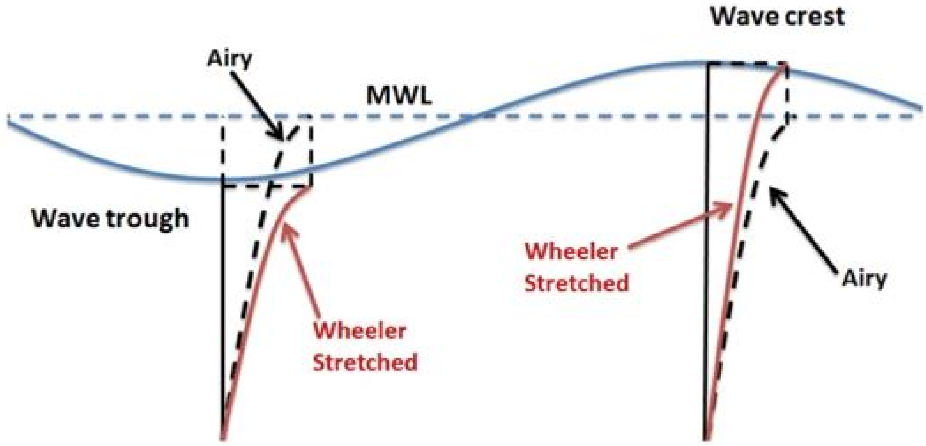

Figure 2.13: Wheeler stretched profile compared with the Airy profile from Karimirad [35]

2.7.3. Aerodynamic Loads

This section details how wind forces on wind turbines are calculated. To understand this, it is important to know the key wind speeds at which turbines operate: cut-in wind speed, rated wind speed, and cut-out wind speed. First, the wind forces that occur when the turbine is in operation will be described. Afterwards, the wind forces when the turbine is idle are pointed out.

The cut-in wind speed refers to the minimum wind velocity required for the turbine to start rotating its blades and begin generating power. As the wind speed increases, the turbine reaches the rated wind speed, at which point a control system is activated. This system regulates the aerodynamic forces on the blades to maintain a constant power output by adjusting the blade pitch angle, preventing excessive power generation. Finally, the cut-out wind speed marks the threshold at which the turbine shuts down to prevent damage, with the blades turned out of the wind.

While these wind speeds may vary slightly between turbine models, they generally follow a similar pattern. Figure 2.14 illustrates the relationship between wind speed and power production, showing the rated wind speed, beyond which the turbine cannot produce more power than its rated capacity. Exceeding this capacity could lead to potential damage. The thrust curve is also shown, indicating that the maximum thrust force occurs at the rated wind speed. This is due to the activation of the pitch control system, which reduces the force acting on the rotor as the wind speed increases.

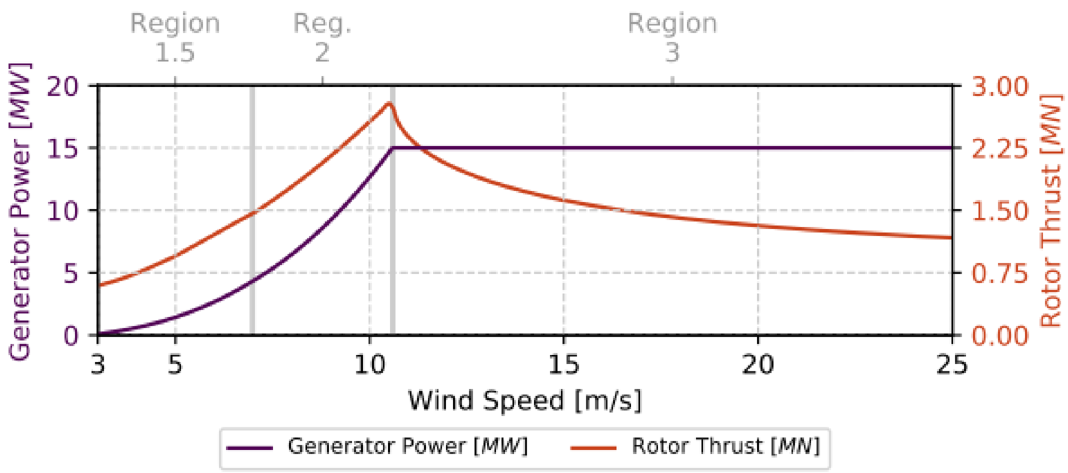

Figure 2.14: Power thrust curve from Gaertner et al. [27]

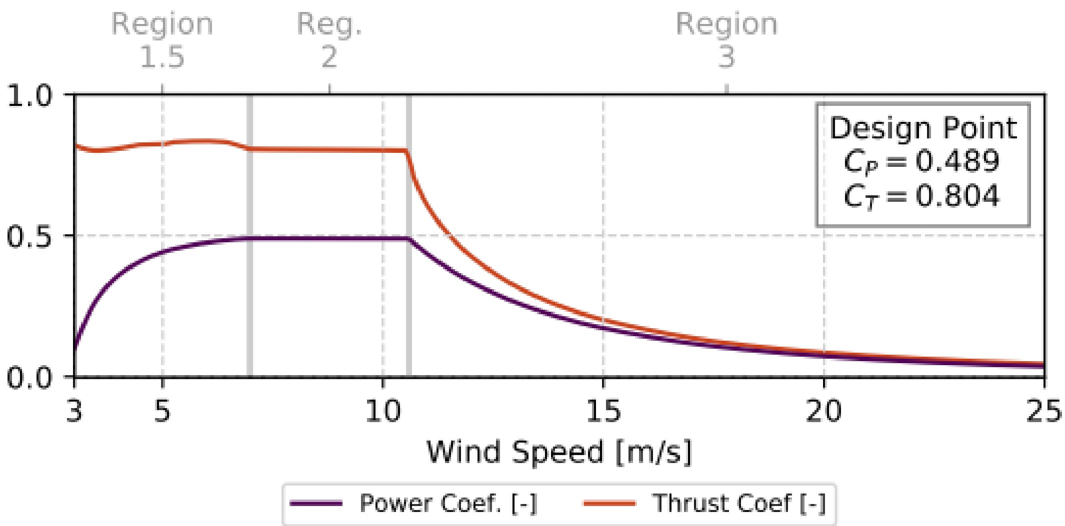

Figure 2.15: Aerodynamic performance coefficients from Gaertner et al. [27]

Wind turbines convert the kinetic energy of wind into electrical energy using a rotor and a generator. The wind exerts two primary forces on the turbine: a thrust force on the nacelle via the rotor blades and a drag force on the tower. The thrust force can be derived using the one-dimensional momentum theory, which applies the laws of conservation of mass and energy:

$$E = \frac{1}{2}\rho U^2 + p + \rho g h = constant \tag{2.13}$$

$$\dot{m} = \rho A U = constant \tag{2.14}$$

By using these principles, the thrust force and extracted power, resulting from the reduction in wind speed and the pressure difference, can be expressed as:

$$T = \frac{1}{2}\rho A_D C_T U_\infty^2 \tag{2.15}$$

$$P = T U_D = \frac{1}{2}\rho A_D C_P U_\infty^3 \tag{2.16}$$

Here U_D represents the difference in wind speed in front and behind of the rotor. C_T and C_P are the thrust coefficient and power coefficient, respectively. These coefficients depend on the axial induction coefficient a, and are related through the following equations:

$$C_T = 4a(1-a) \tag{2.17}$$

$$C_P = 4a(1-a)^2 \tag{2.18}$$

The force on the tower is calculated similarly to the hydraulic drag force. Equation 2.19 shows how the force is calculated.

$$q_{wind} = \frac{1}{2}\rho_a C_a D v^2 \tag{2.19}$$

Where:

- $\rho_a =$ density of air: $1.225kg/m^3$
- $C_a =$ drag coefficient
- $D =$ diameter
- $v =$ rated wind speed

Since wind speeds generally increase over the height of the tower the wind profile is not constant. Ideally, the wind speeds are known over the whole height of the tower. Often, there are no long-term wind speed measurements available on several heights. A popular method for estimating wind speeds at different elevations is the power law. This law uses a power law exponent to correct for surface roughness and atmospheric stability, and it describes the wind speed at a given height as a function of the wind speed at a reference height [34]. The power law can be seen in equation 2.20.

$$v(z) = v_{\text{ref}} \left(\frac{z}{z_{\text{ref}}}\right)^{\alpha} \tag{2.20}$$

Where:

- $v(z) =$ the wind speed at height h,
- $v_{\text{ref}} =$ the wind speed at the reference height h_{ref},
- $\alpha =$ the power law exponent

The power rule allows for good prediction of the wind speed at different heights and therefore is often used to describe the wind profile acting on the tower.

2.8. Hardening Soil Small Strain model (HSS)

The high initial stiffness that soils display at low strain levels is referred to as small-strain stiffness in soil mechanics. The reduction in stiffness as shear strain develops and the partial recovery of stiffness when the loading direction reverses are both captured by the Hardening Soil small strain model. This strain is important in cyclic soil behaviour, where soils show hysteretic behaviour, a type of energy dissipation caused by internal friction and plastic deformation. [12].

The secant shear modulus is defined as in equation 2.21 and describes the reduction of stiffness with increasing strain.

$$G_s(\gamma) = \frac{G_0}{1 + a\left(\frac{\gamma}{\gamma_{0.7}}\right)} \tag{2.21}$$

Where G_0 represents the small-strain shear modulus, $\gamma_{0.7}$ is the shear strain at which the modulus is reduced to 70% of G_0, and a is a model constant. This equation allows the model to accurately predict soil behaviour under cyclic loading by predicting the decrease of stiffness as the cyclic loading progresses.

The tangent shear modulus is defined as in equation 2.22 and is the rate at which shear stress changes in relation to shear strain at a specific location on the stress-strain curve. It represents the material's instantaneous stiffness under shear loading.

$$G_t(\gamma) = \frac{d\tau}{d\gamma} = \frac{G_s(\gamma)}{1 + \left(\frac{\gamma}{\gamma_{0.7}}\right)} \tag{2.22}$$

Hysteretic damping, which happens when the soil deforms and returns under cyclic loading, is one of the main mechanisms of energy dissipation in the HSS model. In the force-displacement or stress-strain environment, the area defined by the hysteresis loop determines the energy dissipation for each cycle [12]. The damping ratio ξ is defined by this energy loss and can be written as in equation 2.23.

$$\xi = \frac{E_D}{4\pi E_s} \tag{2.23}$$

In Figure 2.16 hysteretic behaviour in the small strain model is visualised.

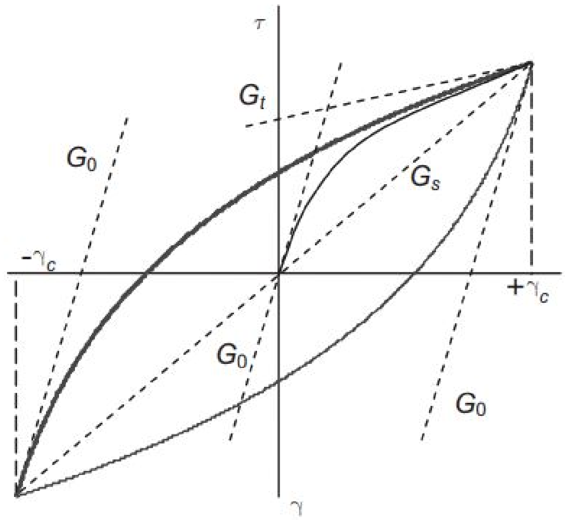

Figure 2.16: Hysteretic behaviour in the small strain model from Brinkgreve, Kappert, and Bonnier [12]

The amount of damping that is obtained depends on the amplitude of the strain cycles. Considering very small vibrations, even the Hardening Soil model with small-strain stiffness does not show material damping as well as numerical damping, whereas real soils still show a bit of viscous damping. Hence, additional damping is needed to model realistic damping characteristics of soils in dynamics calculations. This can be done by means of Rayleigh damping. The HSS model is a useful model for predicting dynamic soil behaviour since it accurately captures both stiffness degradation and hysteretic energy dissipation. The model can be used for dynamic and cyclic calculations. However, it is not intrinsically a dynamic model. It is useful in situations where cyclic behaviour and energy dissipation are the main concerns since it shows the non-linear response of soils under cyclic loading while taking into account the impacts of small-strain stiffness [6]. This does bring some limitations to the model, which are elaborated on next.

2.8.1. Limitations of the HSS Soil Model

The Hardening Soil Small Strain model is frequently used in finite element analyses because it can represent nonlinear soil behaviour with comparatively easy calibration of the parameters. But in dynamic or cyclic stress, its limitations are noticeable [6].

One limitation is overshooting, which occurs when the model resets its material loading memory following small cycles of unloading and reloading. This can result in inaccurate cyclic loading results [18]. Figure 2.17a shows the overshooting limitation schematically. Figure 2.17b shows an example of the overshooting problem where the strain response is not closed. This figure originates from calculations made by Niemunis and Cudny [45]. They showed the results if reloading is interrupted by a mini unloading-reloading loop of $\Delta\sigma_a = 10kPa$.

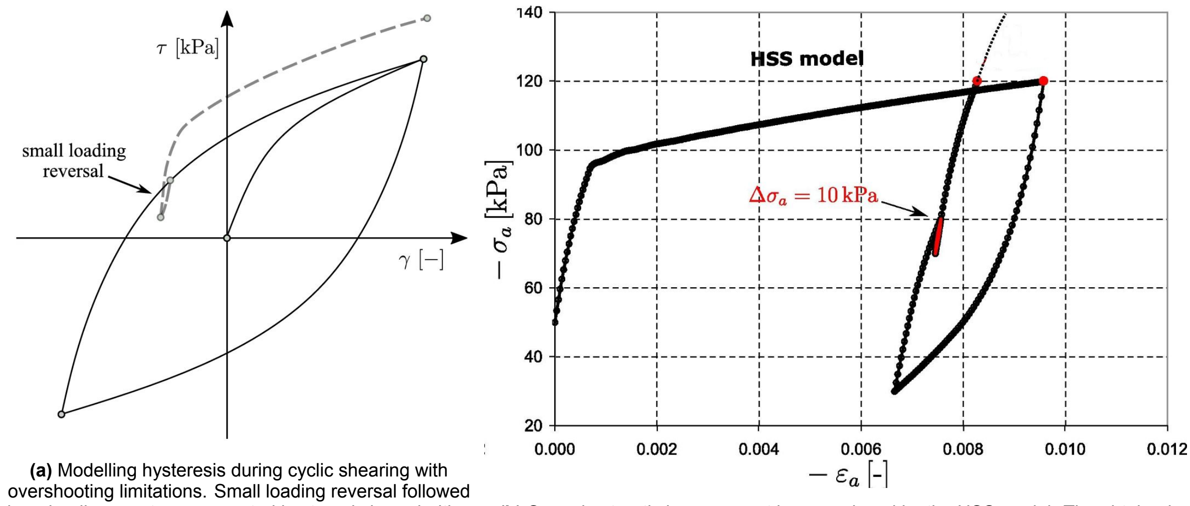

(a) Modelling hysteresis during cyclic shearing with overshooting limitations. Small loading reversal followed by reloading creates unexpected hysteresis irregularities from Cudny and Truty [18].

(b) Some hysteretic loops cannot be reproduced by the HSS model. The obtained response is not closed in strain from Niemunis and Cudny [45].

Figure 2.17: Two examples of the overshooting limitation in the HSS model

Furthermore, the HSS model is best suited for calculations of SLS situations. Although some accumulation may happen in the model, it does not take into consideration the accumulation of irreversible volumetric strains or pore water pressures [13]. For dynamic soil-structure interaction, alternatives like the SANISAND-MS model might offer greater accuracy. However, the determination of the parameters would be more challenging due to the absence of specific guidelines for their selection. Understanding these limitations makes it possible to critically assess the modelling results.

2.9. Offshore Wind Turbine as a Dynamic System

Basic structural models may serve to approximate the dynamic characteristics of the offshore wind turbine system. For various practical considerations, the tower-RNA system can be represented as a vertical Euler-Bernoulli beam with a concentrated mass at its tip. An offshore wind turbine is typically characterised as a dynamical system exhibiting high slenderness and low stiffness properties. Simplified models follow the responsiveness of the foundation-soil system by using springs to illustrate a range of freedom. The design guarantees that the system frequency remains different from both wind and wave frequencies, in addition to the operational range of the turbine. Figure 2.18 presents the coordinate system and the degrees of freedom of the wind turbine. The vibration modes of wind turbines are influenced by the distribution of stiffness and mass within the superstructure and foundation system. Offshore wind turbines typically show two fundamental modes of vibration, sway-bending and rocking. Sway bending is the lateral bending of the wind turbine tower due to the horizontal forces causing deformations along the height of the tower. This bending mode is primarily influenced by the flexible modes of the tower-RNA system, particularly when the foundation displays sufficient axial stiffness in relation to the tower. Rocking is the rotational tilting of the entire system caused by limited axial stiffness at the base. In the scenarios where an offshore wind turbine is founded on a shallow foundation, the rocking mode comes as the main type of behaviour due to the axial deformation of the foundation [61].

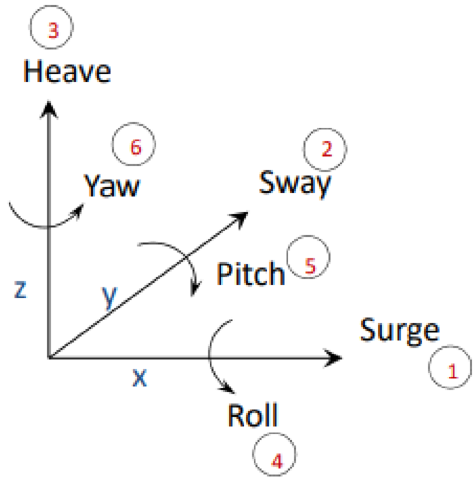

Figure 2.18: Degrees of freedom of the wind turbine from Varghese, Pakrashi, and Bhattacharya [61]

2.10. Natural Frequency of Offshore Wind Turbines

To prevent resonance with different excitation frequencies, such as wind, waves, rotor rotational frequency (1P), and blade passing frequency (3P), for three-bladed wind turbines, the natural frequency of an offshore wind turbine and foundation needs to be carefully taken into account throughout the design phase. Resonance could arise from the system's natural frequency matching the excitation frequencies, which can lead to a significant increase in fatigue and possible structural damage [62]. As shown in Figure 2.19, three different frequency ranges are specified: soft-soft, soft-stiff, and stiff-stiff. The soft-soft range includes natural frequencies below 1P. Structures in this range are too flexible, making them vulnerable to resonance with the wave frequencies. The soft-stiff range is between 1P and 3P frequencies. This range is preferred in offshore wind turbine design because it balances rigidity and flexibility. The construction is rigid enough to prevent resonance yet flexible enough to avoid over dimensioning. The stiff-stiff range covers designs with natural frequencies above 3P. This method rules out resonance but typically produces rigid, over dimensioned structures. These designs are costly due to greater material and construction costs [33]. These ranges should be taken into account during the design phase in order to reduce the risk of resonance.

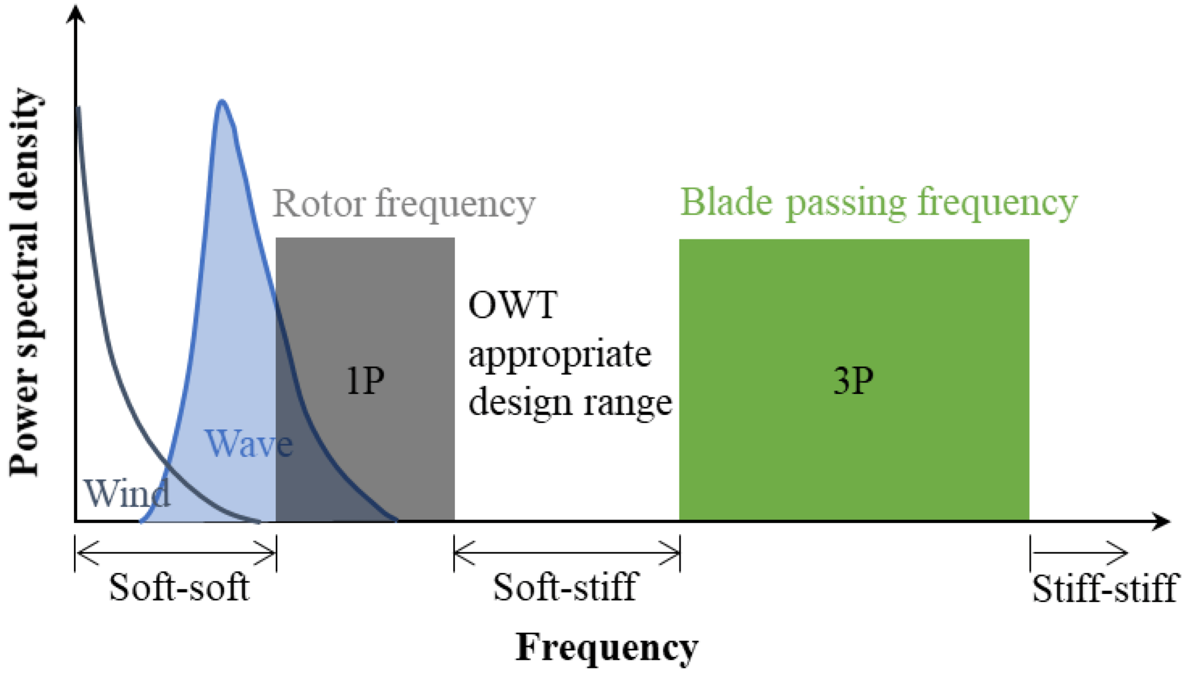

Figure 2.19: Frequency ranges for a three-bladed offshore wind turbine from Wan et al. [62]

2.10.1. Wind Turbine Operational Frequencies

The rotor rotational frequency and the blade passing frequency are the main operational frequencies for offshore wind turbines. These frequencies originate from the rotating rotor and are associated with a number of harmonic loading effects, such as tower shadow, yaw misalignment, wind shear, and gust slicing. The rotor frequency corresponds to the 1P frequency, while the blade passing frequency is corresponding to the 3P frequency. These frequencies, which are directly derived from the turbine's rotor speed, are crucial for determining the aerodynamic loading of the wind turbine. The first fore-aft, side-to-side, and torsional modes of vibration usually have the lowest natural frequencies for turbines with steel substructures [24].

2.10.2. Wind and Wave Frequencies

Wave spectra that correspond to the anticipated changes in sea conditions can be applied to represent the frequency range of the waves. These spectra, such as JONSWAP or Pierson Moskowitz, have a lengthy tail at higher frequencies, with the maximum energy at the peak frequency. The frequency region between the 1 and 3P bands is often covered by this tail. The frequency of waves exerted on offshore structures has a frequency between $0.1 - 0.2Hz$. For the wind spectra, the Kaimal spectrum is most commonly used to determine the frequency peak. The frequency of wind loading on an offshore structure is most of the time lower than $0.1Hz$ [62].

2.11. Fast Fourier Transform

The Fast Fourier transform is used to transform a signal from the time domain to the frequency domain. The Fast Fourier Transform (FFT) is a fast computational algorithm to perform the Discrete Fourier Transform (DFT). The concept of the FFT is to transform an array of time-domain waveform samples into an array of frequency-domain spectrum samples. By using zero-padding and windowing techniques, the frequency resolution can be improved and spectrum leakage is limited. Often, the FFT data is concentrated on a specified frequency range, and undesirable frequencies are filtered out. The natural frequencies of a system can be identified by performing an FFT from a free vibration signal. In Equation 2.24 the key equation for the FFT is given [57]. In this thesis, the FFT has the goal of determining the natural frequencies of the combination of the offshore wind turbine and the foundation.

$$X[k] = \sum_{n=0}^{N-1} e^{-2\pi j \frac{kn}{N}} x[n] \tag{2.24}$$

Windowing functions such as the Blackman window are used to reduce spectral leakage in FFT results. Windowing improves frequency resolution by smoothing the transition at the outer boundaries of the signal. The formula used for the Blackman windowing that SciPy [56] is used can be found in equation 2.25.

$$w(n) = 0.42 - 0.5\cos\left(\frac{2\pi n}{N-1}\right) + 0.08\cos\left(\frac{4\pi n}{N-1}\right) \tag{2.25}$$

2.12. Logarithmic Decrement Method

The logarithmic decrement method is a recognised technique for determining the damping ratio from the free decay response of a system. By analysing the amplitude decay over multiple oscillations of the free vibration, the method provides an effective way to calculate how quickly the vibrations reduce over time. [40]. In this thesis, the logarithmic decrement method will be applied to calculate the damping ratio and the logarithmic decrement of the system of the wind turbine and the foundation. This will be done with the aim of describing the damping behaviour of the system. The equations to determine the logarithmic decrement and damping ratio are shown in equations 2.26 and 2.27 and are achieved from Carswell et al. [15].

$$\delta = \frac{1}{n} \ln \frac{x(t)}{x\,(t+nT)} \tag{2.26}$$

Where:

- δ = logarithmic decrement
- n = number of oscillation cycles between two amplitude measurements
- $x(t)$ = displacement (or amplitude) of the system at time t
- $x(t+nT)$ = displacement (or amplitude) of the system after n oscillation periods
- T = period of oscillation

$$\zeta = \frac{1}{\sqrt{1 + (2\pi + \delta)^2}} \tag{2.27}$$

Where:

- ζ = damping ratio
- δ = logarithmic decrement

The damping ratio represents how fast a system dissipates energy and returns to a state of no oscillations. The interpretation of the damping ratio:

- $\zeta = 0$: Represents undamped systems where no damping occurs in the system. This is common for idealised systems but rarely occurs.
- $0 < \zeta < 1$: Represents systems that are underdamped and whose oscillations decrease over time. This is typical for the majority of mechanical systems and engineering constructions.
- $\zeta = 1$: Represents systems which are critically damped and that oscillate for as little as possible before coming to rest.
- $\zeta > 1$: Represents overdamped systems that gradually return to rest without experiencing oscillations.

A system typically oscillates at its natural frequency in free vibration, with damping causing the amplitude to gradually decrease. The logarithmic decrement method performs well when calculating how fast these free vibrations stop [40].

3 Research Methodology

In this chapter, the research methodology is explained in order to address the research questions. This thesis investigated the soil-structure interaction of a pneumatic caisson foundation compared to a monopile foundation for offshore wind turbines, combining theoretical research, numerical modelling, and a practical evaluation. The methods that are described below have been used to address the research questions.

Determination of the hydraulic and aerodynamic loads

The hydraulic loads exerted on the offshore wind turbine were ascertained using MetOcean data and the theories outlined in the literature review. The MetOcean dataset contains wave, wind, and current data from 1979. An Extreme Value Analysis (EVA) was employed to determine the design loads, guaranteeing the structure's resilience against severe environmental circumstances. A comparable methodology was employed to assess the aerodynamic loads exerted on the structure, which provided the necessary information for subsequent modelling and analysis.

Determination of the soil characteristics

Cone Penetration Test (CPT) data was examined to define the soil conditions at the location and provide the parameters necessary for the Plaxis 3D model. To illustrate the behaviour of the soil, the Hardening Soil Small Strain (HSS) model was selected. The CPT data was used to determine the relevant parameters for the HSS model to make sure that the numerical model accurately represented soil-structure interaction.

Initial dimensioning of the pneumatic Caisson

The initial dimensions for the pneumatic caisson were determined based on the literature review findings. These dimensions were used as the initial dimensions of the caisson in the Plaxis 3D model.

Quantitative modelling and evaluation

The numerical model was created via Plaxis 3D, a finite element modelling software commonly employed in geotechnical engineering, to assess the soil-structure interaction. To model the different conditions and carry out in-depth analyses of the caisson's and monopiles' performance, four models were created. Multiple evaluations were performed to assess the structural and dynamic performance of the pneumatic caisson and monopile foundation. A push-over analysis was conducted to ascertain the maximum force the structures could withstand and to find the potential failure modes. An investigation of free vibrations was conducted to investigate the natural oscillations of the structures, with natural frequencies and damping ratios obtained by the Fast Fourier Transform (FFT) and the logarithmic decrement method.

Furthermore, two cyclic loading analyses were conducted to evaluate the performance of the monopile and caisson under different loading situations. A cyclic load with increasing amplitude was implemented to investigate the soil-structure interaction throughout various deformation ranges, from minor deformations to near-failure deformations. A cyclic loading analysis with constant amplitude was performed to simulate the maximum environmental force, assessing the structure's performance under sustained environmental loading.

Analysis and reflection of results

The performance of the pneumatic caisson compared to the monopile foundation was shown by the finite element analyses. Stability, deformation, and load-bearing capacity were among the factors that were examined. Based on these findings, conclusions are made.

Practical considerations in the construction and installation of the Caisson

To determine feasibility, the practical considerations regarding installing the pneumatic caisson foundation were investigated. To determine whether the caisson could be transported to the site, a buoyancy assessment was carried out. To calculate whether the downward forces on the caisson were enough to embed the caisson to the required depth, a sinking calculation was carried out.

4

Input Parameter Determination for the Numerical Model

4.1. Input Parameters for the Numerical Model

In this chapter there will be elaborated on the forces used in the models together with the soil properties used in the models. The wave, wind and current data used to calculate the forces was retrieved from the Metocean Data Portal by DHI Group [21]. The CPT used for determining the soil parameters was retrieved from soil data from windpark Hollande Kust Noord by Fugro [26]. First, the force parameters used for the different analyses are determined. Then the ground parameters are derived using the CPT. Lastly, the dimensions of the caisson that is used in the models will be introduced.

In Table 4.1 the coordinates of the location on which the forces and soil properties are based on. This location was chosen for two main reasons. Firstly, there was sufficient ocean and soil data available for this location, especially a CPT was available from which soil parameters could be derived. Secondly, there is already a windpark at this location. Therefore, the environmental data of this location that is retrieved represents realistic data on which the force calculations can be based.

Table 4.1: Coordinates and mean sea level of the chosen location

Location	Longitude [deg.E]	Latitude [deg.N]	Mean sea level [m]
Point 1	4.275617	52.759843	25

4.1.1. Forces on the Structure

Here the steps taken to calculate the forces that are exerted on the models are given. The more detailed calculations can be found in Appendix A.

For the determination of the design loads, an extreme value analysis (EVA) was conducted on the wave, wind, and current data. The return period was chosen to be 50 years. Typically, the design lifetime for which a wind turbine support structure is planned for is 20 to 30 years [22]. To be on the more conservative side and take some safety into account due to the preliminary nature of this thesis, the design lifetime was chosen to be 50 years. The EVA was implemented using the pyextremes Python library. This Python library is aimed at performing univariate EVA's [9]. The extremes are selected with the peak over threshold (POT) method. A threshold of 4.3 meters for wave height and 22.5 m/s for wind speed were used. The thresholds are chosen as they mark the 99% quantile of the database. A declustering time of 72 hours was used to distinguish between different storms. The generalised Pareto distribution was found to be a good fit for the data, on which the values of significant wave height and wind speed belonging to the return period of 50 years were determined. The results of the EVA can be found in Table 4.2. The peak period corresponding to the return period is calculated with the empirical formula as can be seen in equation4.1, which uses the calculated significant wave height.

Table 4.2: Results EVA analysis with a return period of 50 years

Parameter	Value
Significant Wave Height [m]	7.2
Current Speed [m/s]	2.0
Wind Speed [m/s]	37.7
Peak Period T_p [s]	14.2
Maximal Wave Height [m]	13.9

$$T_p = 5.3\sqrt{H_s} \tag{4.1}$$

According to DNV [22] the maximum wave height can be calculated according to equation 4.2.

$$H_{max} = 1.94 H_s \tag{4.2}$$

Wave number and rotational frequency were calculated to determine the kinematics of water particles based on wave parameters. Using linear wave theory and modifying it to account for wave-current interactions, water particle velocities and accelerations at the various depths were calculated. Drag and inertia forces were calculated at each depth using the Morison equation.

In Figure 4.1 the Wheeler stretched profile can be seen and the height at which the different equations are exerted.

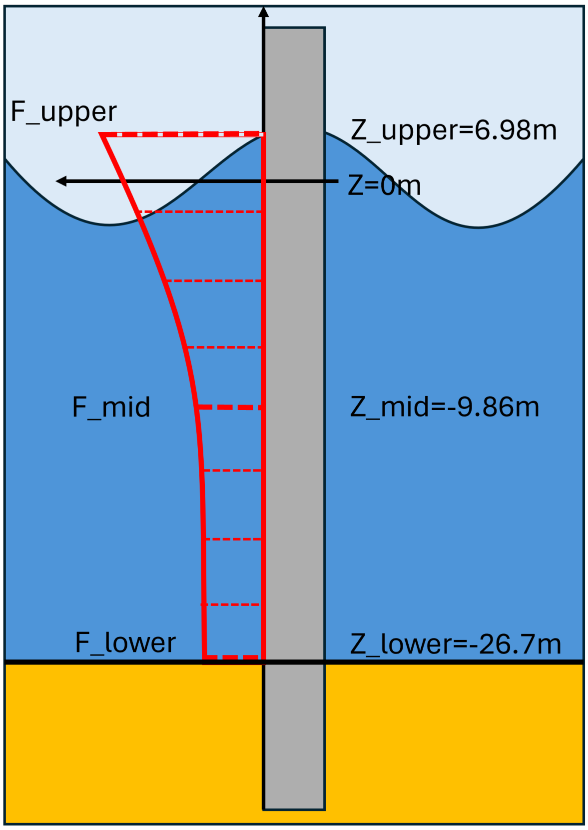

Figure 4.1: Profile of the hydraulic forcing profile and the reference heights of the stretched profile

In Table 4.3 the sum of the calculated drag and inertia forces can be found for the different heights.

Table 4.3: Calculated forces at the different heights representing the forcing profile

Location	Total Force [kN/m]
Upper	459.72
Mid	428.71
Lower	337.69

Simpson's rule is used to integrate the forces at the different levels and to determine the base shear force and the overturning moment at the base of the structure. The hydraulic shear force and the overturning moment resulting from the hydraulic forces are shown in Table 4.4.

Table 4.4: Hydraulic shear force and the overturning moment at the base

Parameter	Value
Base Shear	11.45 MN
Overturning Moment	487.38 MNm

Since during storm conditions the tower will not be in service and the rotor blades will be pitched to feather, so there will be no thrust force on the tower. The wind force during storm conditions is calculated according to equation 2.19. The rated wind speed used is $37.72m/s$ at a height of $100m$. Since the wind profile is not constant the power rule as can be seen in equation 2.20 is used to calculate the wind speed.

The power rule provided the wind profile. By integrating the profile the wind load on the tower was achieved. The wind force is exerted at the reference height of 100 meter. The results of the base shear and the overturning moment caused by the wind load can be found in Table 4.5.

Table 4.5: Wind shear force and the overturning moment at the base

Parameter	Value
Base Shear	0.8 MN
Overturning Moment	80 MNm

Adding the hydrodynamic and aerodynamic components results in the total base shear and overturning moment due to environmental loading. The total shear force and overturning moment due to the environmental loads can be found in Table 4.6.

Table 4.6: Total shear force and the overturning moment at the base due to environmental loads

Parameter	Value
Base Shear	12.45 MN
Overturning Moment	567.38 MNm

The calculated forces are applied in the different models. Due to the fact that the models make use of symmetry to lower the computational times of the calculations, the force from Table 4.6 are divided by two to account for the correct force being applied in the models. In this thesis, the total force acting on the structure will be used for consistency in documentation, rather than the half force employed in the symmetric model.

4.1.2. Soil Layers and Parameters

Here the soil parameters that are used to define the different soil layers in the model are determined. The soil layers are defined based on the cone penetration test executed by Fugro [26] at the 'Hollandse Kust Noord' wind farm constructed in the Dutch North-Sea. The HKN20 location from the report provided by Fugro [26] has been chosen to function as the reference location because it has similar conditions as where the caisson would be placed if it were constructed. The build up of the soil layers is based on the CPT in Figure 4.2 and can be found in 4.7.

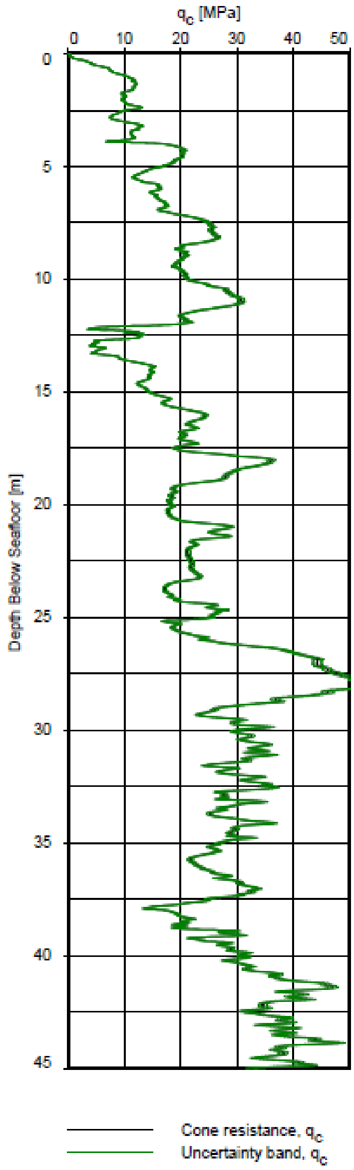

Figure 4.2: Cone resistance q_c against depth below seafloor from Fugro [26]

In Table 4.7 the relevant soil parameters that originates from the CPT at location HKN20 from the site investigation done by Fugro [26] can be found.

Table 4.7: CPT analysis results for the location HKN20 from Fugro [26]

Soil layer	Depth (m)	Cone Resistance (qc) [MPa]	Sleeve Friction (fs) [MPa]	Unit Weight (γ) [kN/m³]	Net Cone Resistance (qc1N) [MPa]	Lateral Earth Pressure (K0)	Relative Density (Dr) [%]	Friction Angle [deg]
1	0 - 4	8	0.08	19.3	10	1.4	80	38.5
2	4 - 12	20	0.2	19.7	16	1	80	38.5
3	12 - 25	18	0.15	19.5	25	0.5	70	38
4	25 - 40	30	0.27	20.3	30	0.5	70	38.5
5	40 - 50	35	0.3	20	30	0.5	65	38

Based on the formulas provide by Robertson [51] and Robertson and Cabal [52], the soil parameters for the hardening soil small strain soil model from the CPT in Figure 4.2 were calculated. The soil parameters used in the Plaxis models can be found in Table 4.8.

In order to model the strength bonding at the interfaces between the soil and the structure, the reduction factor, R_{inter}, was set to 0.7 after taking into account the anticipated interaction roughness between the soil and the structure. Realistic adhesion and friction are balanced by this number, which is frequently used in modelling practice to represent a somewhat rough interface. Additional consultation with Feddema [25] supported the choice for this number. The value chosen is consistent with usual values for modelling soil-structure interactions, where interface strength is often lower than the surrounding soil mass. This provides accurate yet cautious modelling of the interface behaviour.

The small-strain stiffness modulus $E_{0,ref}$ is estimated using the cone resistance q_c:

$$E_{0,ref} = \alpha \cdot q_c \tag{4.3}$$

where α is an empirical coefficient, typically ranging from 2.5 to 5 for sands. α is chosen to be 4 in this thesis.

The reference moduli are derived from the cone resistance q_c using empirical relationships from Robertson [51] and Benz [6]:

Reference secant stiffness ($E_{50,ref}$):

$$E_{50,ref} = \beta \cdot q_c \tag{4.4}$$

where β is an empirical coefficient, typically around 2 to 5 for sands. β is chosen to be 3 in this thesis

Reference tangent stiffness for unloading/reloading ($E_{ur,ref}$):

$$E_{ur,ref} \approx 3 \cdot E_{50,ref} \tag{4.5}$$

Reference oedometer stiffness ($E_{oed,ref}$):

$$E_{oed} = \left(\frac{1-\nu}{1-\nu-2\nu^2} \right) \cdot E_{50} \tag{4.6}$$

The reference pressure is assumed as atmospheric pressure of $p_{ref} = 100kPa$.

The small-strain shear modulus is estimated as:

$$G_0 = \frac{E_{0,ref}}{2(1+\nu)} \tag{4.7}$$

where ν is the Poisson's ratio, typically taken as 0.2 to 0.3 for sands. Base on the data from Fugro [26] ν is 0.2.

These formulas were used to calculate the soil parameters for the Hardening Soil Small Strain model of the different soil layers. The soil parameters used in the model can be found in Table 4.8.

Table 4.8: Input parameters for the HS small model for different soil layers

Soil layer	Depth [m]	E_{50ref} [MPa]	$E_{ur;ref}$ [MPa]	E_0 [MPa]	nu	G_0 [MPa]	$\gamma_{0.7}$	R_{inter}	ϕ' [deg]	δ [deg]	c' [kPa]
1	0 - 4	32	96	192	0.2	80	0.0002	0.7	38.5	8.5	0.1
2	4 - 12	80	240	480	0.2	200	0.0002	0.7	38.5	8.5	0.1
3	12 - 25	72	216	432	0.2	180	0.0002	0.7	38	8	0.1
4	25 - 40	120	360	720	0.2	300	0.0002	0.7	38.5	8.5	0.1
5	40 - 50	140	420	840	0.2	350	0.0002	0.7	38	8	0.1

As stated in Section 2.8 the hardening soil model with small strain does not capture material damping as well as numerical damping, so one other soil parameter needed to be defined, the Rayleigh damping of the soil. Since the determination of these damping parameters is outside the scope of this thesis, it was determined from a conversation with Kementzetzidis [36] that the Rayleigh damping parameters as shown in 4.9 would suffice for the purpose of this thesis. This range covers standard operational and dynamic frequencies important for soil-structure interactions in offshore structures, ensuring a balance between numerical stability and realistic damping.

Table 4.9: Damping percentages and target frequencies

Parameter	Value
Chi_1	1%
Chi_2	1%
f_1	0.1 Hz
f_2	5 Hz

4.1.3. General Dimensions of the Caisson

A gravity-based construction was used as a starting point for the pneumatic caisson's dimensions, as it is partially similar to the pneumatic caisson in terms of material, functioning, and weight. However, the pneumatic caisson will be embedded into the seabed. This will also generate a frictional force on the outside of the pneumatic caisson, which will improve its overall stability. This is similar to the suction caisson foundation. There are some examples of wind turbines that are founded on suction caisson foundations and gravity-based foundations in the literature. The dimensions of these are also known. Nevertheless, these foundations are for wind turbines that are smaller in size than the one that is the subject of this thesis. Using this information, an engineering guess has been made for the pneumatic caisson's preliminary dimensions, which will be applied in the Plaxis model.

The preliminary dimensions of the caisson that are used in the model are shown in Table 4.10 and a sketch of the caisson with its dimensions can be found in Figure 4.3.

Table 4.10: Dimensions of the Pneumatic Caisson

Component	Size
Length	$30\,\mathrm{m}$
Width	$30\,\mathrm{m}$
Height	$10\,\mathrm{m}$
Wall Thickness	$1\,\mathrm{m}$
Floor Thickness	$2\,\mathrm{m}$
Ceiling Thickness	$1.5\,\mathrm{m}$
Transition Piece Diameter	$10\,\mathrm{m}$
Transition Piece Thickness	$0.055\,\mathrm{m}$
Transition Piece Height	$10\,\mathrm{m}$
Cutting Edge Height	$2\,\mathrm{m}$
Cutting Edge Width	$1\,\mathrm{m}$

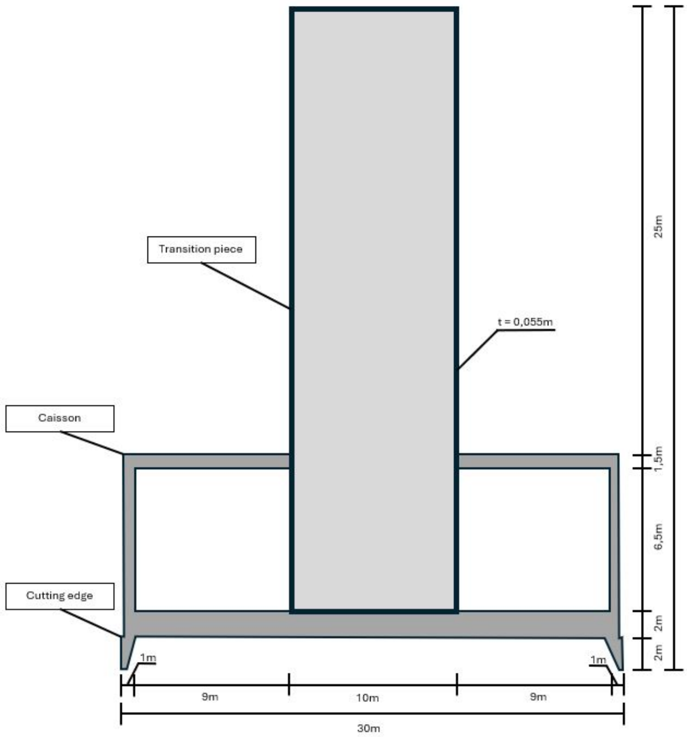

Figure 4.3: Sketch of the dimensions of the pneumatic caisson

5 Numerical Model

In this chapter, the Plaxis 3D models used for calculations will be elaborated on. This chapter is structured in a similar way to Plaxis. The structure is, namely: soil, structures, mesh, and staged construction. First, the soil parameters will be defined. Secondly, there will be elaborated on how the models are constructed. Thirdly, the mesh is constructed, and lastly, the staged construction is discussed in which the loading phases are determined. Figures of the different models and analyses from PLAXIS 3D are provided in Appendix B to visually support the interpretation and understanding of the models and analyses discussed.

5.1. Modelling Choices for the Monopile and Caisson Structures

In total, four different models are used to make the calculations done in this thesis. All models make use of symmetry, so only half of the model needed to be created. This significantly reduced the computational time. To gain an understanding of the structural behaviour and stability, pushover and free vibration analyses were performed using the whole tower model, which includes the whole wind turbine. Two of these models were made, one with the monopile and one with the caisson as a substructure.

The other two models are based on a practicality often used in the preliminary calculations for the design of offshore foundations. This practicality is the eccentricity ratio of $M/V = 5D$, where M is the overturning moment and V is the shear force. This rule of thumb estimates the ratio between moment and shear force on the construction. Because it simplifies the load distribution by combining the hydraulic and wind loads along the pile and offers a start for evaluating the initial stability and load transfer from the wind turbine through the foundation into the seabed.

The principle behind the rule is that a force applied at $5D$ height will result in a proportionate distribution of moment and shear force that is representative of the actual loading conditions at the mudline. This height creates realistic stress patterns in the foundation and structure and acts as an efficient point of application for the lateral loads [38]. Also, not the whole height of the tower had to be modelled, which is beneficial for the computational time of the calculations. In this model, since the diameter at the tower base is ten meters, the height of the models and the point where the lateral force is exerted are 50 meters. Two of these models were made, one with the monopile and one with the caisson as substructure. These models were used to model the foundation behaviour under different cyclic loading conditions. Using lateral forces at $5D$ eccentricity, this model simplifies the representation of critical loading conditions while reducing the computational complexity of the model.

In Figures 5.1, 5.2, 5.3 and 5.4 the four different Plaxis 3D models used for calculations are shown.

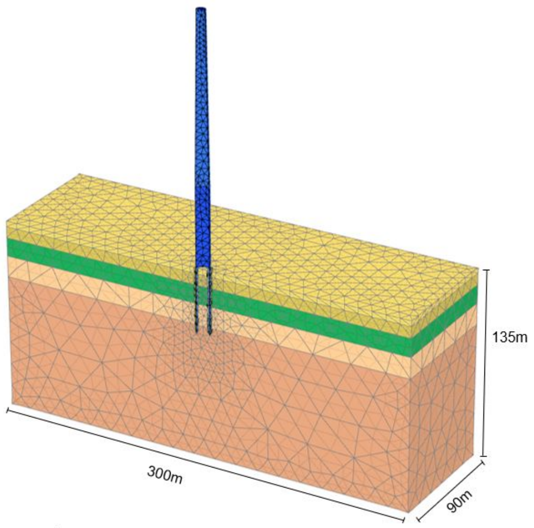

Figure 5.1: Monopile model with the complete tower

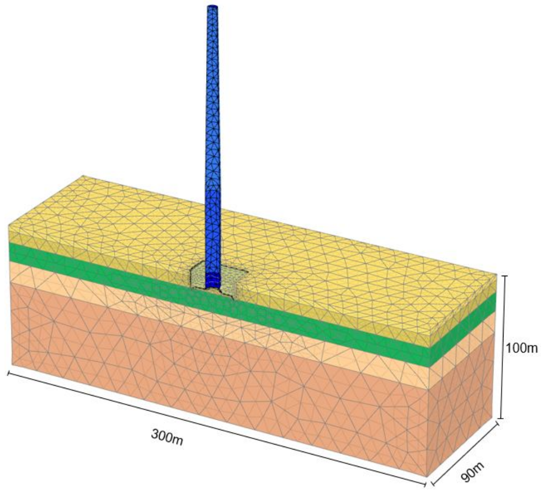

Figure 5.2: Caisson model with the complete tower

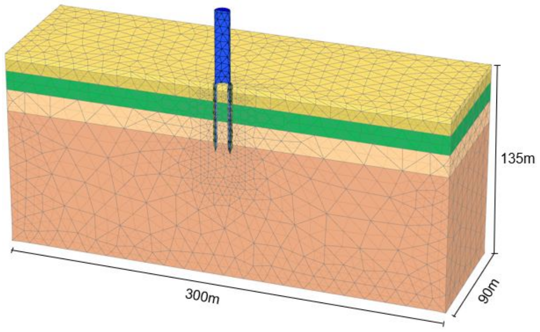

Figure 5.3: Monopile 5D model

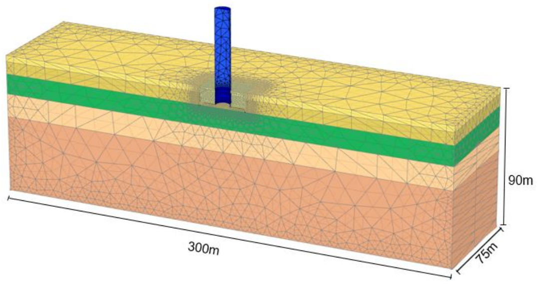

Figure 5.4: Caisson 5D model

Since this thesis has the goal of doing a preliminary comparison assessment between a monopile and a caisson, the forces are calculated on the preliminary level, and the model where an eccentricity of five times the diameter of the monopile at the mudline was chosen to be sufficient in modelling the different behaviour of the monopile and the caisson in cyclic loading conditions.

The force is applied in the models, where the behaviour under ULS conditions is calculated. It was chosen to apply the found base shear at 50 meters. However, this resulted in an overestimation of the overturning moment that was applied. In Equation 5.1 the corresponding moment to this horizontal force is calculated.

$$\frac{M}{H} = 5D \rightarrow M = 12.45 \cdot 50 = 622.5MNm \tag{5.1}$$

This is an overestimation of approximately 7.5%. This resulted in a more conservative approach to the calculations and can be seen as a safety factor.

By following this approach, only one horizontal force needed to be exerted on the model to represent the base shear and the overturning moment, simplifying and improving the application of the model. The equivalent force of $12.45MN$ exerted at 50 meters would be $3.55MN$ when it would be exerted at the top of the wind turbine, at a height of 175 meters. This value is used to compare the results of the push-over analysis to the governing environmental loading condition.

5.1.1. Models with the Complete Tower Length

Modelling of the Superstructure

The transition piece and tower were modelled as plate elements. A differentiation was made between the plate elements that were used to model the transition piece and the plate elements that were used to model the tower. Those elements were given the corresponding properties of the transition piece and the tower as given by Gaertner et al. [27]. The transition piece was modelled by creating half of a circle with a diameter of 10 meters using the polycurve tool. Next, the circle was extruded to the height of the transition piece as given by Gaertner et al. [27] and a surface element was created. This element was assigned with the transition piece plate. Since the tower tapers from the transition piece to the hub, this was modelled slightly differently. Namely with the lofted polygon option in Plaxis. This way, the tapered surface was created, after which the tower plate was assigned to this surface. The RNA mass was modelled by creating a plate at the top of the tower. This plate was given similar steel properties as the plates that represent the tower and transition piece. However, the unit weight assigned was higher to match the weight of the complete RNA mass, as given by Gaertner et al. [27].

The loads on the structure are also added in this model. The loads on the pile are modelled by distributed loads. A distributed load was chosen over a point load since this was judged to be more realistic and would prevent pile deformations due to the high forces exerted on the tower by a point load. The values were assigned to the loads in the staged construction phase. In Figure 5.5 a screenshot from Plaxis 3D of the tower with the elements as described before can be seen.

Figure 5.5: Screenshot of the tower as modelled in Plaxis 3D

Modelling of the Monopile

Next, the substructure was modelled. First, a model with a monopile was created. In Figure 5.6 a screenshot from Plaxis 3D of the monopile foundation can be found. The monopile is created by creating a half circle with a 10 meter diameter using the polycurve tool. The circle was extruded to reach a depth of 45 meters, similar to the depth of the monopile in Gaertner et al. [27]. On the surface elements, plates with the properties of the steel used for the monopile were created to model the monopile. A positive and negative interface was created at the plates that represent the monopile to make clear to Plaxis that it concerns a soil structure boundary.

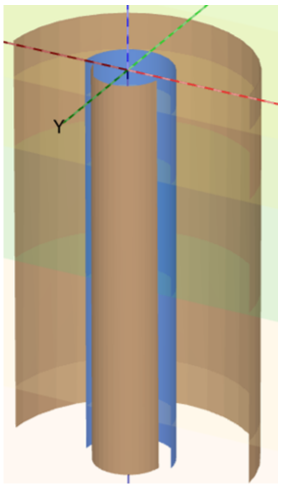

Figure 5.6: Screenshot of the monopile as modelled in Plaxis 3D

Modelling of the Caisson

The caisson is modelled by creating volume elements. The volume elements were given the dimensions as stated in Table 4.10. The volume elements were assigned linear elastic soil model properties that match the properties of reinforced concrete. This soil model uses Hooke's law of isotropic linear elasticity [49]. The linear elastic model is insufficient for simulating soil behaviour. However, it is generally utilised for modelling stiff constructions in the surrounding soil, like concrete slabs [37]. Also, the non-porous behaviour setting is chosen. In this setting, neither initial nor excess pore pressures are taken into account. The parameters can be found in Table 5.1.

Table 5.1: Parameter values concrete caisson

Parameter	Value	Unit
Soil model	linear elastic	-
Drainage type	non-porous	-
$\gamma_{concrete}$	25	kN/m³
ν	0.2	-
E_{ref}	29960000	kN/m²
E_{oed}	33290000	kN/m²
G_{ref}	12480000	kN/m²
R_{inter}	1	-

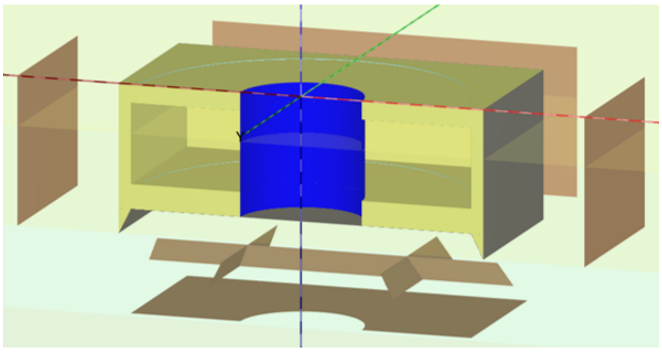

Figure 5.7: Screenshot of the caisson as modelled in Plaxis 3D

In Figure 5.7 a screenshot from Plaxis 3D of the caisson foundation can be found. Inside the caisson, a half circle was created using the polycurve tool and extruded to a height of 10 meters, forming a surface extending from the base to the top of the caisson. This surface was assigned plate elements with properties matching those of the monopile, resulting in a hollow caisson. The hollow space inside the caisson was filled with water in the Plaxis models. Additionally, interface elements were generated at all contact surfaces between the caisson and the surrounding soil.

5.1.2. Models with a Height of 50 meters

Modelling of the superstructure

For the models with a height of 50 meters the substructures are modelled in the same way as in Section 5.1.1. Instead of modelling the complete tower, only the tower up to a height of 50 meters is modelled. This is done in a similar fashion as before. Half a circle is drawn with the polycurve tool. This half circle is extruded to a height of 50 meters, and a surface element is created, which is assigned a plate element. According to Gaertner et al. [27] the tower has the same thickness and diameter up to a height of 55 meter. Therefore, the plate has the same properties as the transition piece. Since in this model the tower is cut off above 50 meters, the mass of the tower that is cut off needs to be taken into account. This tower and top mass are modelled as a plate at a height of 50 meters. This plate is given a thickness of 0.25 meter and an extremely heavy unit weight of $800kN/m^3$

5.2. Mesh Creation

This section elaborates on the mesh creation, local refinement, and sensitivity analysis of the finite element mesh used in Plaxis. After the structures were defined, the meshes of the different models were created. Plaxis has an option that automatically creates a mesh for the user. The user can adjust this automatic mesh-making to refine the mesh at certain critical points in the mesh. These are mostly places where high forces or stress are expected. In the models, the mesh was refined in expected critical areas by creating a volume element, which was given a lower coarseness factor. In this way, the mesh was locally refined around the critical points. All boundaries in the mesh are normally fixed. The mesh near the boundaries was also refined. This was done to prevent any unwanted boundary effects due to possible numerical issues. There were no dynamic boundaries defined. Therefore, the mesh needed to be big enough to dampen the waves before they act on the boundaries. This was made sure by performing an iterative sensitivity check on the generated meshes.

5.2.1. Sensitivity Analysis of the Mesh

A sensitivity analysis was performed to guarantee mesh sufficiency. A range of mesh sizes and mesh fineness levels were evaluated. First, large displacements were modelled in an initial calculation to evaluate if the mesh was sufficiently large and fine. The results were then analysed to look for displacements at the mesh boundaries. Mesh sizes were increased iteratively until boundary displacements were reduced.

The final mesh dimensions, number of soil elements, and nodes for each model are shown in Table 5.2. Due to spikes at the interface between the structure and the soil in the 5D caisson model, an extra refinement of the mesh around the caisson was made. This mitigated the problem. However, it resulted in a significant increase of soil elements and nodes in the mesh.

Table 5.2: Dimensions, number of soil elements and number of nodes of the mesh for the different models

Model	Width	Length	Depth	Number of soil elements	Number of nodes
Caisson with tower	300	90	100	9634	18248
Monopile with tower	300	90	135	7890	16479
Caisson 5D	300	75	90	50180	81969
Monopile 5D	300	90	135	8884	18398

5.3. Phased Construction

In this section, the phases in the staged construction tab of each model are elaborated on. The faces are different from each other depending on the type of analysis that is executed. First, this section elaborates on the different phases constructed for the pushover analysis. Secondly, the phases for the free vibration analysis are discussed. Lastly, the cyclic analyses are handled. The first phase, called the initial phase, is the same for every analysis conducted. Before any external loading or structure appears, the first phase in PLAXIS 3D is used to determine the initial stress state and equilibrium of the soil, taking into account elements like in-situ stresses and initial soil conditions. The second phase of each model, the installation phase, is also the same for each model. In this phase, all the structural elements are activated, and the soil reactions based on the weight of these structural elements are calculated. Generally, no forces are applied in the installation phase.

Multiple analyses were performed with the constructed models. In Figure 5.8 the schematisation of the different analyses that are conducted can be found. In the next subsection, each analysis will be elaborated on.

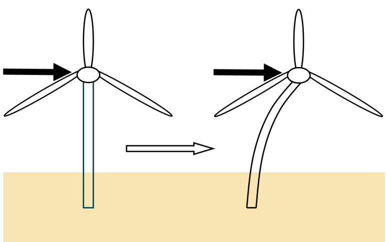

(a) Pushover analysis

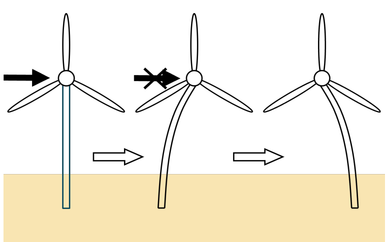

(b) Free vibration analysis

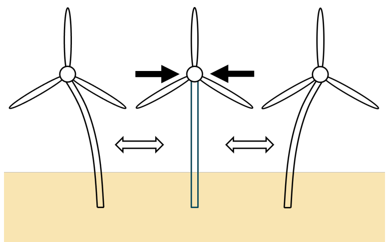

(c) Cyclic analysis

Figure 5.8: Schematisation of the different analyses that have been performed

5.3.1. Push over Analysis

The pushover analysis is done in every model. This analysis is done to determine what the maximal force of the structure can be before it fails. This phase is constructed by applying a force at the top of the model, in the full models with the tower as well as the 5D models, and keeps increasing this force until the structure fails. When analysing the results of the pushover analysis, the necessary force to achieve a certain location can be found.

5.3.2. Free Vibration Analysis

To be able to make a clear comparison between the free vibration behaviour of the monopile and the caisson foundation, it is important that the displacements of the top of the tower start from the same displacement. This displacement at the top is chosen to be $1m$. To achieve the free vibration of the structure, a small vibration will already suffice. A displacement of one meter at the top of the tower is big enough to capture a clear free vibration and small enough to prevent plastic deformations in the soil, which could interrupt the free vibration of the structures.

After this phase, a new phase is constructed. This phase is a dynamic calculation. In this phase, the dynamic time was defined to be $60s$ to achieve a long enough signal to capture the decay in the free vibration but not too long to prevent long computational times. The force from the previous phase is deactivated, and the phase is calculated. This results in the free vibration signal of both the tower founded on the monopile and the tower founded on the caisson.

5.3.3. Cyclic Loading

To prevent unwanted mass effects from coming into play during the analysis of the soil structure interaction and still be able to model the cyclic behaviour of the soil, it is chosen to exert the force on the structure in a static way. This is done by creating multiple loading and unloading phases. By exerting the structure in this way, the time element is removed from the analysis. However, it is still possible to model the different loading and unloading phases in order to capture the cyclic soil-structure behaviour.

Two cyclic analyses were carried out. Both are carried out on the $5D$ models. The first cyclic analysis consists of a sinusoidal loading, whose amplitude increases after every 2 cycles. The formula for this forcing can be found in equation 5.2.

$$F = A \cdot \sin(\Omega t) \tag{5.2}$$

After every two cycles, the amplitude of the force increases from $1A$ to $2A$, $3A$, until $6A$. For the $5D$ monopile model and the $5D$ caisson model, the starting amplitude was $3MN$. The forces were chosen based on the maximal environmental load that is calculated in Section 4.1.1. The cycles start with a lower forcing and increase to a forcing that is significantly higher than the maximal environmental load that was calculated. This is done with the aim to capture both the behaviour in lower forcing areas and the behaviour closer to failure. Starting from a force lower than the environmental loads acting on the structure and gradually increasing the amplitude of the forcing also aims to model possible preloading effects of the soil. Preloading can increase the density and alter the soil stiffness. This will provide a more realistic modelling of the soil structure interaction and will indicate the stability under cyclic loading. Figure 5.9 shows the increasing forcing on the model. The phases of the models were constructed in the following manner. After the installation phase a phase, the loading phase, was constructed where the forcing with amplitude A is exerted at the top of the model. The next phase is modelled with zero force exerted at the top, the unloading phase. In the next phase, a negative force with amplitude A is exerted on the top of the structure, the negative loading phase. This goes on until the second cycle of a force of $6A$ is exerted on the model.

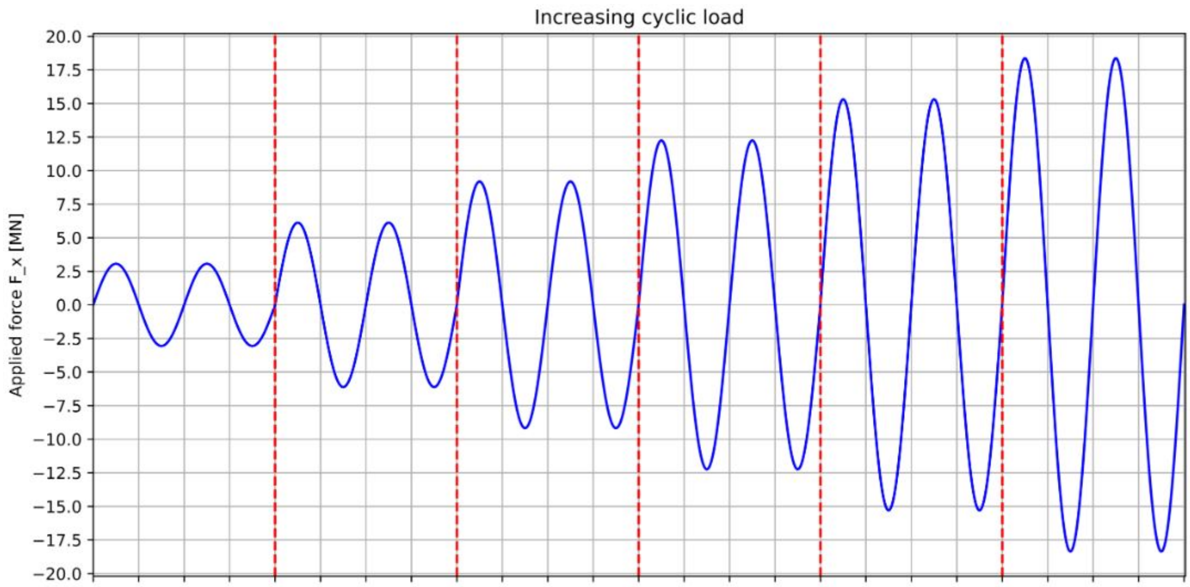

Figure 5.9: The increasing sinusoidal load in x-direction applied in the model

In the second cyclic loading analysis, the forcing was in the form of a constant amplitude sinusoidal loading. This force remained constant and had a duration of twelve cycles. The force exerted on the top of the structure is for both $5D$ models $12.45MN$. Figure 5.10 shows the constant amplitude forcing on the model. This cyclic analysis provides insights into the cyclic behaviour of the structures under extreme environmental conditions. The phases are created similarly to the phases created for the increasing cyclic load analysis.

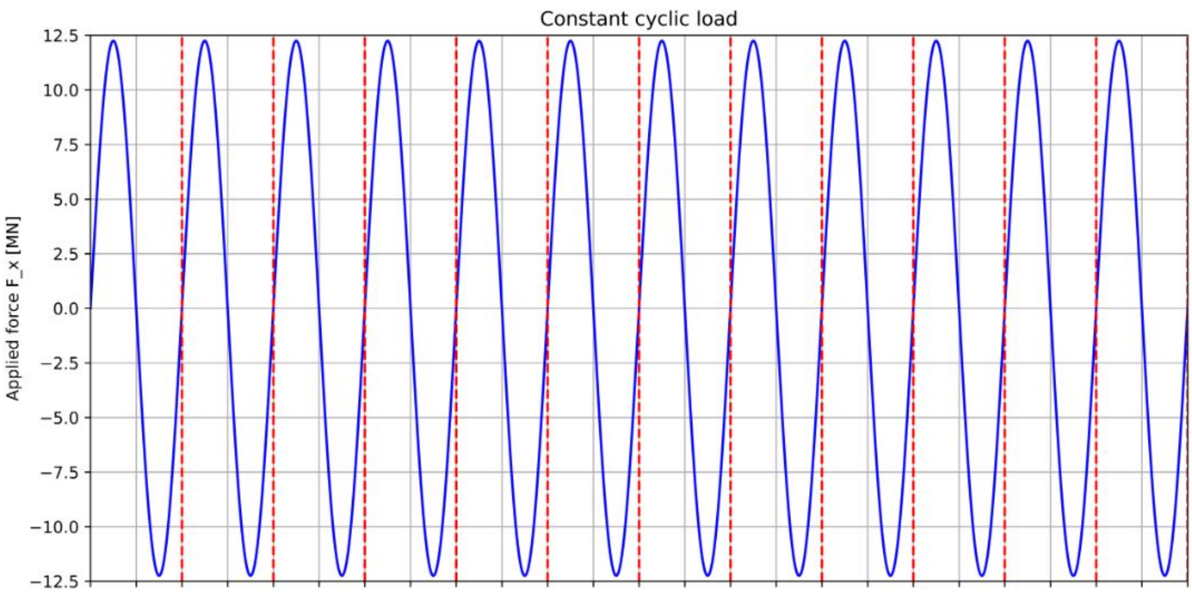

Figure 5.10: The constant sinusoidal load in x-direction applied in the model

The two cyclic analyses, one characterised by increasing amplitude and the other by constant amplitude, address complementary roles. The increasing amplitude loading shows the structure's response to deteriorating circumstances and possible cumulative effects. The constant amplitude analysis simulates an extended environmental loading scenario, focusing on cyclic stability and potential fatigue effects under endured extreme conditions. These analyses provide an understanding of the cyclic performance and resilience of the structure.

6 Results

In this chapter, the results of the different analyses will be given. Whereafter, these results will be interpreted. First, the results of the pushover analysis are discussed. Secondly, the results of the free vibration analysis together with the FFT and logarithmic decrement method are elaborated on. Lastly, the results from the two cyclic analyses are discussed.

6.1. Pushover Analysis

The results of the pushover analysis provide insight into how the deformations of the structure and soil develop as the force increases at the top of the tower. In Figure 6.1 the graph of the pushover analysis can be seen. From the results of the pushover analysis, insights are given into the structural capacity of the structure and the non-linear behaviour caused by the soil-structure interaction. Generally, in offshore engineering, a monopile-founded wind turbine is assumed to fail when the horizontal deflection at the mudline is more than the diameter divided by 10 [38]. In this thesis, the diameter of the monopile is ten meters, so according to this design guideline, failure is reached at a lateral displacement at the mudline of one meter. The pushover analysis shows what force must be applied to the top of the tower to achieve this displacement.

The monopile appears to be able to withstand a significantly higher lateral force compared to the caisson. In relationship with the displacement, the monopile seems to have a longer range, where the relationship between the increasing displacement and increasing force is almost linear. This range lies approximately from $0MN$ to $20MN$. The caisson has a smaller range compared to the monopile where this relationship stands, approximately from $0MN$ to $8MN$ of force. These forces are applied at the top of the tower, at a height of 175 meters above the mudline.

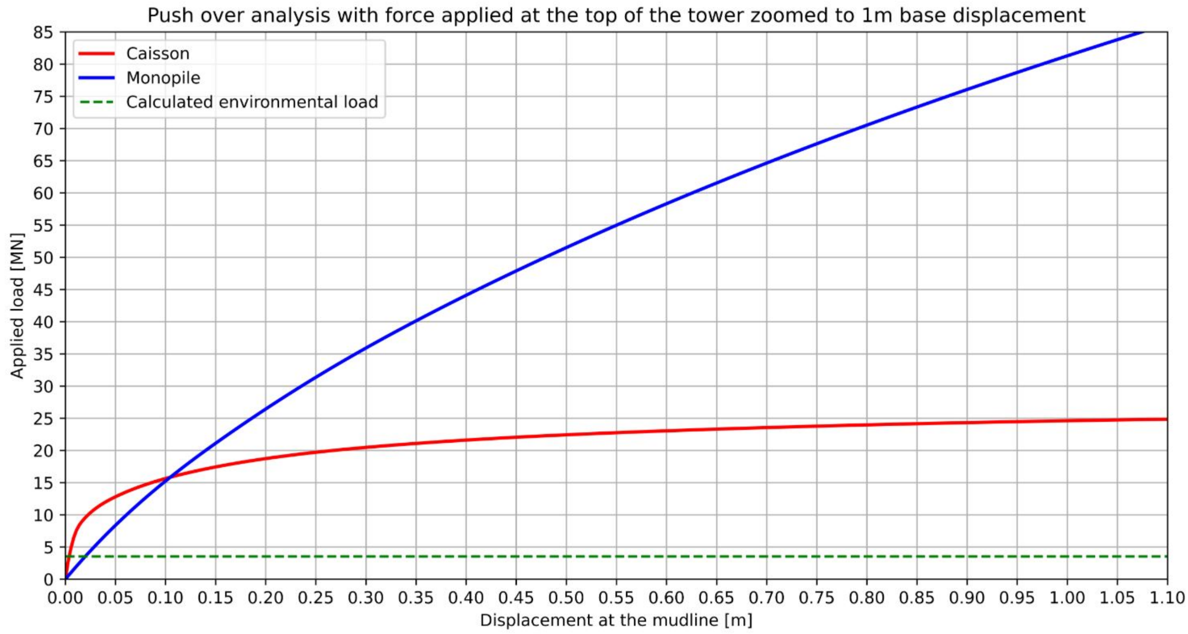

Figure 6.1: Results of the pushover analysis of the monopile and caisson zoomed to $1m$ base displacement

As can be seen in Figure 6.1 the displacement at a force of 82 MN for the monopile and a force of $25MN$ for the caisson result in a lateral base displacement of one meter. According to the design guideline, the structure fails when the lateral base displacement is more than one meter. The caisson fails at a significantly lower lateral force than the monopile. However, the caisson can still withstand the maximal forcing as calculated earlier, of $3.55MN$. This force is indicated as the green dashed line in the figure. Also, the caisson fails in a different way than the monopile would fail. As shown in Figure 6.1 the force-displacement curve of the monopile does not show as clear non-linear behaviour as the caisson does. The criterion for failure for the monopile appears to be not the same as for the caisson. At a base displacement of one meter, the caisson can be assumed to have already failed, since this is already far in the non-linear deformation part. It can be stated that the failure point of the caisson could be set at the point where the graph shows the transition between elastic deformation to elastoplastic and plastic non-linear behaviour. This point marks the tipping point from elastic to elastoplastic behaviour. This point is at a force of $8MN$. In Figures 6.2a, 6.3 and 6.4a the total displacement vectors at $1m$, $0.015m$ and $0.1m$ of base displacement are shown. These figures show the way the caisson displaces at the monopile failure criteria, the start of the elastoplastic zone, and the plastic deformation zone.

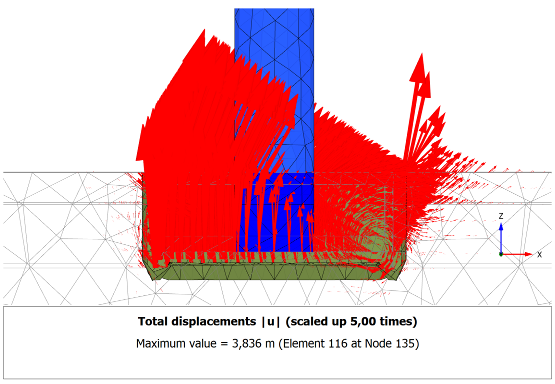

(a) Caisson: Vector plot of the total displacement at a base displacement of 1 meter, with a force exerted of $25MN$

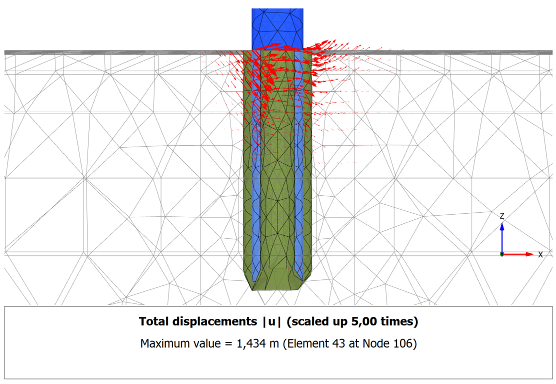

(b) Monopile: Vector plot of the total displacement at a base displacement of 1 meter, with a force exerted of $82MN$

Figure 6.2: Vector plots of the total displacement of the caisson and the monopile with a lateral base displacement of 1 meter

As can be seen in Figure 6.2a there is a high amount of soil that is activated around the structure, resulting in a nonlinear soil behaviour with plastic deformations. It can be seen that the caisson is tilting over. The rotation centre is around the right cutting edge. The caisson is pulled out of the soil. Also, the displacements are huge compared to figures 6.3 and 6.4a, a total displacement of $3.836m$ compared to a total displacement of $0.2885m$ and $0.1188m$. This indicates that the structure is already past failure and the failure criterion for the monopile, which states the monopile fails at a lateral base displacement of more than one meter, is not an accurate indication of a caisson's failure. For comparison in Figures 6.3 and 6.2b the vector plots of the total displacements of the monopile can be seen

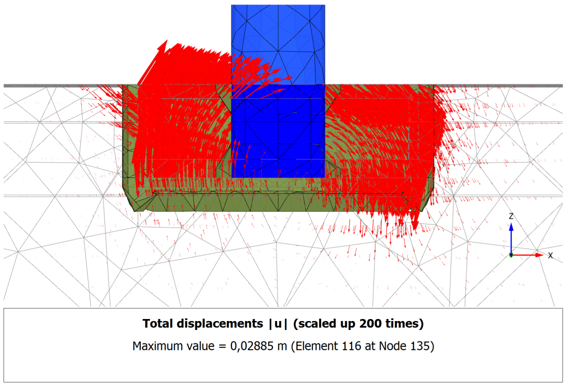

Figure 6.3: Caisson: Vector plot of the total displacement at a base displacement of 0.015 meters, with a force exerted of $8MN$

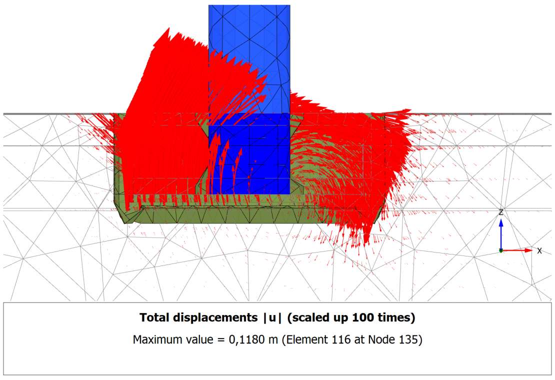

(a) Caisson: Vector plot of the total displacement at a base displacement of 0.1 meters, with a force exerted of $15.5MN$

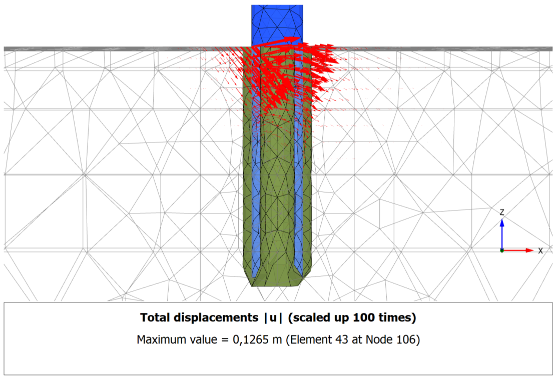

(b) Monopile: Vector plot of the total displacement at a base displacement of 0.1 meters, with a force exerted of $15MN$

Figure 6.4: Vector plots of the total displacement of the caisson and the monopile with a lateral base displacement of 1 meter

What is interesting to see in Figure 6.3 and 6.4a is that the rotation point around which the displacements seem to rotate is shifting to the right if the force is increasing more and the caisson enters the elastoplastic zone. This shift in rotation point indicates plastic deformation of the soil. These irreversible deformations are not desirable as a foundation for an offshore wind turbine. It can be stated that the caisson would fail when this rotation centre starts to shift away from the centre under the caisson.

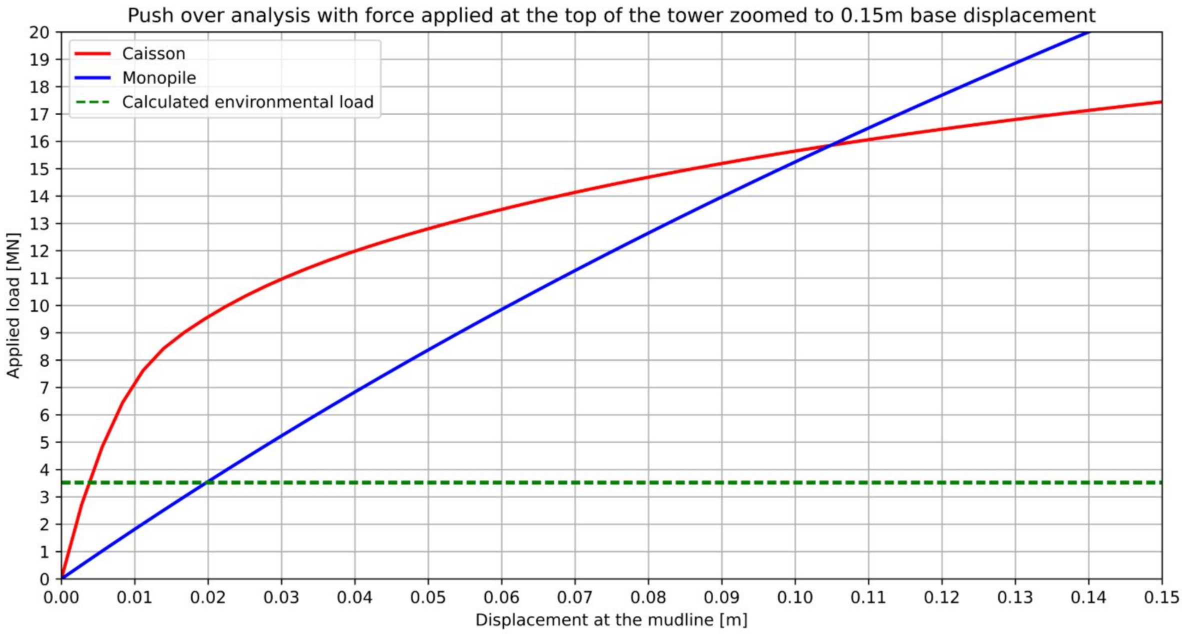

Figure 6.5: Results of the pushover analysis of the monopile and caisson zoomed to $0.15m$ base displacement

In Figure 6.5 the graph is further zoomed to show the intersection between the curve of the monopile and the caisson. When the force at the top increases to $15.5MN$ the displacement of the monopile and caisson at the base are the same. When the force increases further the caisson will have a higher displacement with an increase of force compared to the monopile. However, both the monopile and the caisson show elastic behaviour under the maximum calculated forcing. As can be seen in Figure 6.5 the caisson behaves stiffer and shows less deformation under this maximum loading compared to the monopile.

6.2. Free Vibration Analysis

The results of the free vibration analysis, starting from a lateral top displacement of one meter, of the monopile and the caisson can be found in Figure 6.6. The Figure shows that both oscillations start from the same initial displacement of 0.95 meter. This displacement is reached by exerting a force at the top of the tower of $1.20MN$ in the monopile model and $1.35MN$. It can be seen that the caisson oscillates slightly faster compared to the monopile. This indicated that the caisson is stiffer compared to the monopile. This corresponds to behaviour that was found from the pushover analysis.

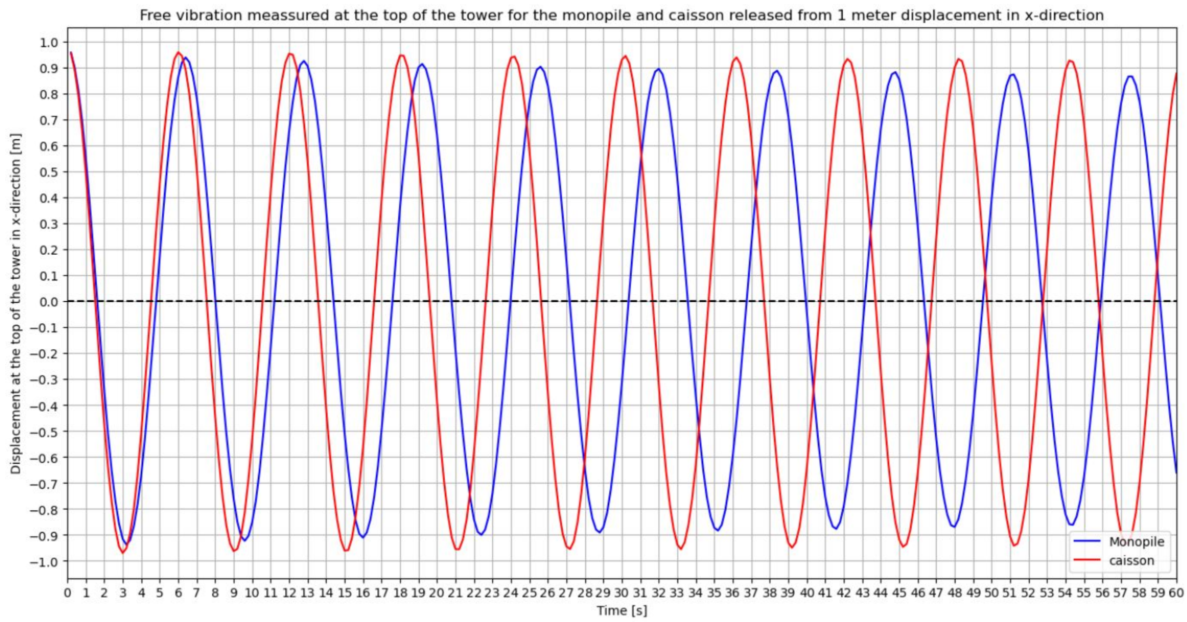

Figure 6.6: Free vibration of the caisson and the monopile starting from 1m top displacement

As time passes, the monopile shows a slightly greater decay in amplitude over the consecutive oscillations compared to the caisson. This implies that the monopile experiences slightly more damping compared to the caisson.

6.3. Fast Fourier Transform

Next, an FFT was conducted over the results of the free vibration analysis of the monopile and the caisson. To perform the FFT a Python code has been written. The results of the Fast Fourier transform can be found in Figure 6.7. From these results, the first natural frequencies of the monopile and caisson are achieved. The natural frequencies are found at the peaks of the graphs and the values can be found in Table 6.1.

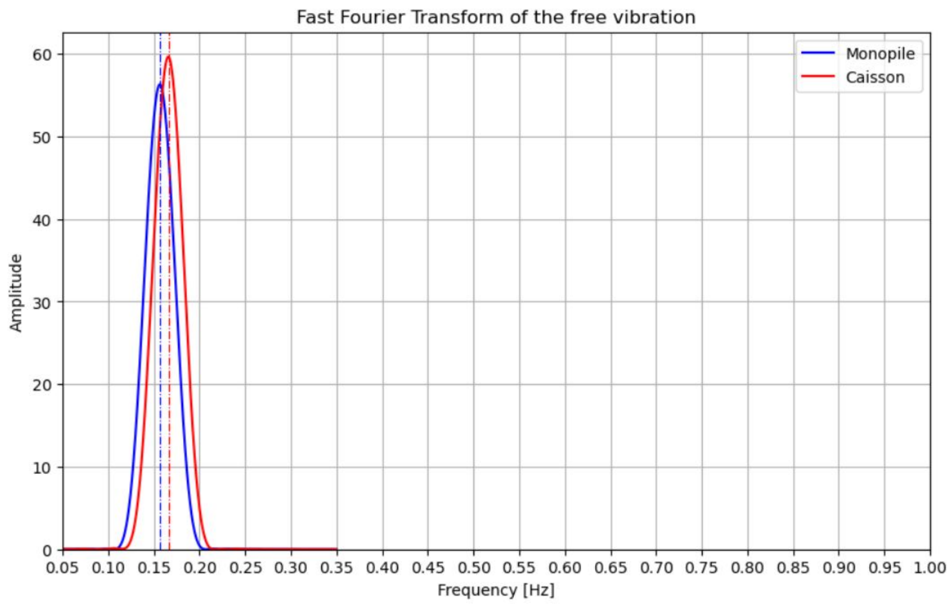

Figure 6.7: Result of the Fast Fourier transform of the free vibration

Table 6.1: First natural frequency for Monopile and Caisson

Structure	First natural frequency (Hz)
Monopile	0.157
Caisson	0.166

The natural frequency of the wind turbine founded on the caisson construction is slightly larger than the natural frequency of the wind turbine founded on the monopile. This difference is caused because the caisson is a stiffer construction compared to the monopile, hence the slightly higher natural frequency. However, the difference in natural frequencies is quite small. This is an indication that the superstructure, the wind turbine on top of the foundation, is the governing structure that influences the natural frequency of the system.

In Figure 6.8 the relevant frequencies are shown. The JONSWAP and Kaimal spectra are computed based on Metocean data of the North Sea at the described location. As can be seen in Figure 6.8 the natural frequencies of the monopile and the caisson do not coincide with the peak of the JONSWAP spectrum and fall in the soft-stiff range, between the 1P and 3P frequencies.

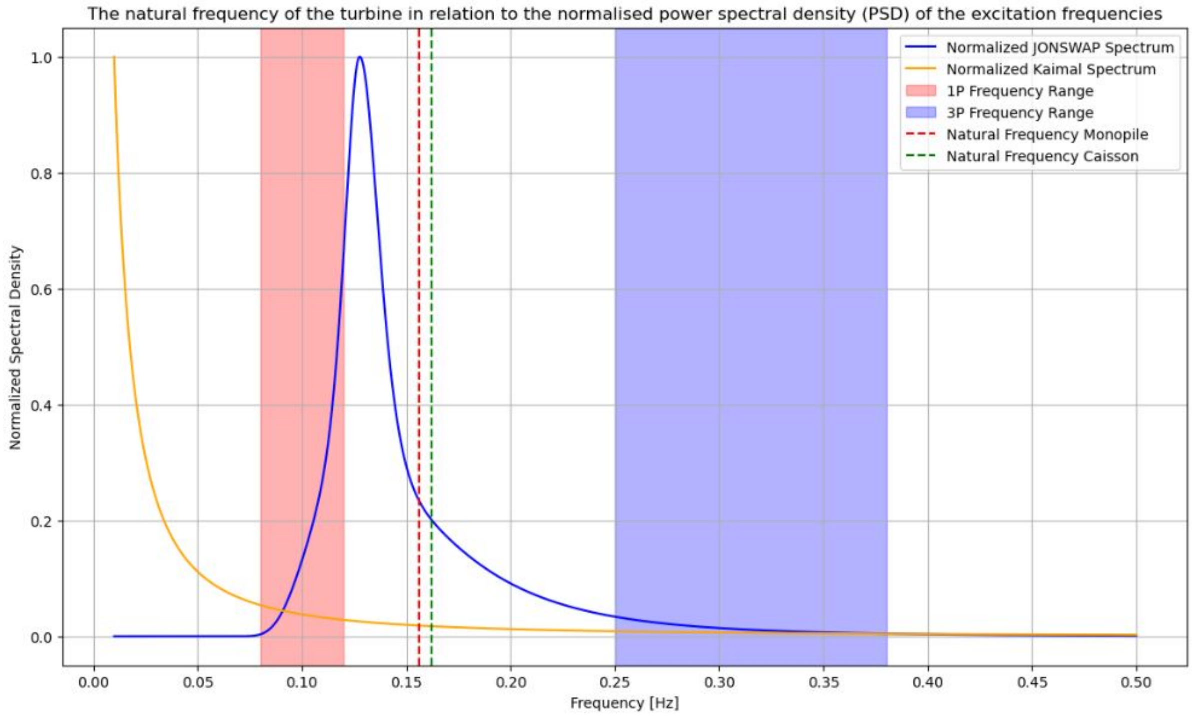

Figure 6.8: The natural frequency of the turbine in relation to the normalised power spectral density (PSD) of the excitation frequencies

6.4. Logarithmic Decrement Method

In this section, the results of the logarithmic decrement method that was performed on the free vibration of the monopile and the caisson are given. The logarithmic decrement was performed to estimate the damping ratio of the systems. In Figure 6.9 the free vibration with the logarithmic envelope is shown.

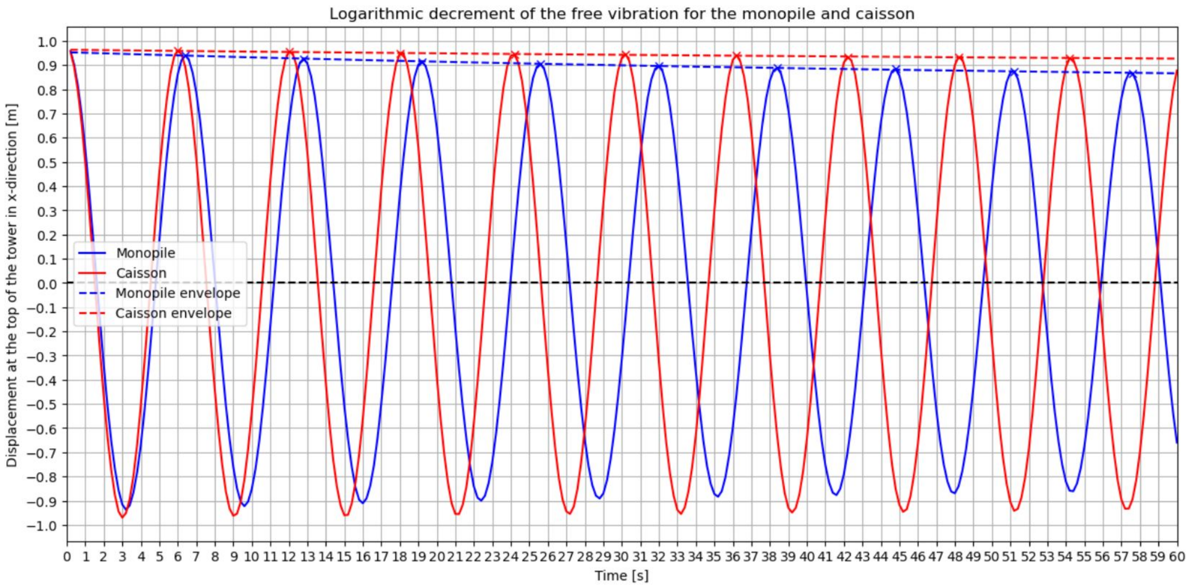

Figure 6.9: Free vibration with the logarithmic decrement envelope of the 1 meter top release free vibration

The results of the logarithmic decrement method calculations can be found in Table 6.2.

Table 6.2: Logarithmic Decrement and Damping Ratio for Monopile and Caisson

Parameter	Monopile	Caisson
Logarithmic Decrement	0.010	0.004
Damping Ratio (zeta)	0.002	0.001

As can be seen in Figure 6.9 and what the values in Table 6.2 show, there is a very small decay visible in the free vibration of the monopile and the caisson founded structures. This indicates that there is weak damping in both systems. The monopile shows a slightly higher damping compared to the caisson, indicating that it dissipates energy from the vibration slightly faster, but neither structure experiences significant energy dissipation. The slightly lower damping ratio corresponds to the stiffer behaviour of the caisson, but this difference is so small it is not significant. The little decay that is observed likely originates from the added Rayleigh damping assigned as a soil parameter in the different soil layers. In the models, there was no structural damping assigned to the material properties of the structural elements of the tower, monopile, and caisson. This explains the small decay in the free vibration. If the structural damping was added to the structural elements, the decay in the vibration would have been greater and more realistic.

6.5. Cyclic Loading Analyses

6.5.1. Force Displacement Curves

Monopile

In Figure 6.10 the force-displacement curve resulting from the cyclic analysis of the monopile is shown. Twelve forcing cycles were exerted in the model. The height of the force exerted in the model is equal to the maximal environmental load and exerted at 50 meters above the mudline. This force is equal to $12.45MN$. Clear hysteresis loops can be seen. The first cycle resulted in the biggest loop. The cycles gradually become smaller after more cycles. The shrinking size of the loops in this case may indicate a hardening action of the soil. The effective stiffness of the system appears to be increasing, possibly as a result of the compaction of the soil surrounding the monopile.

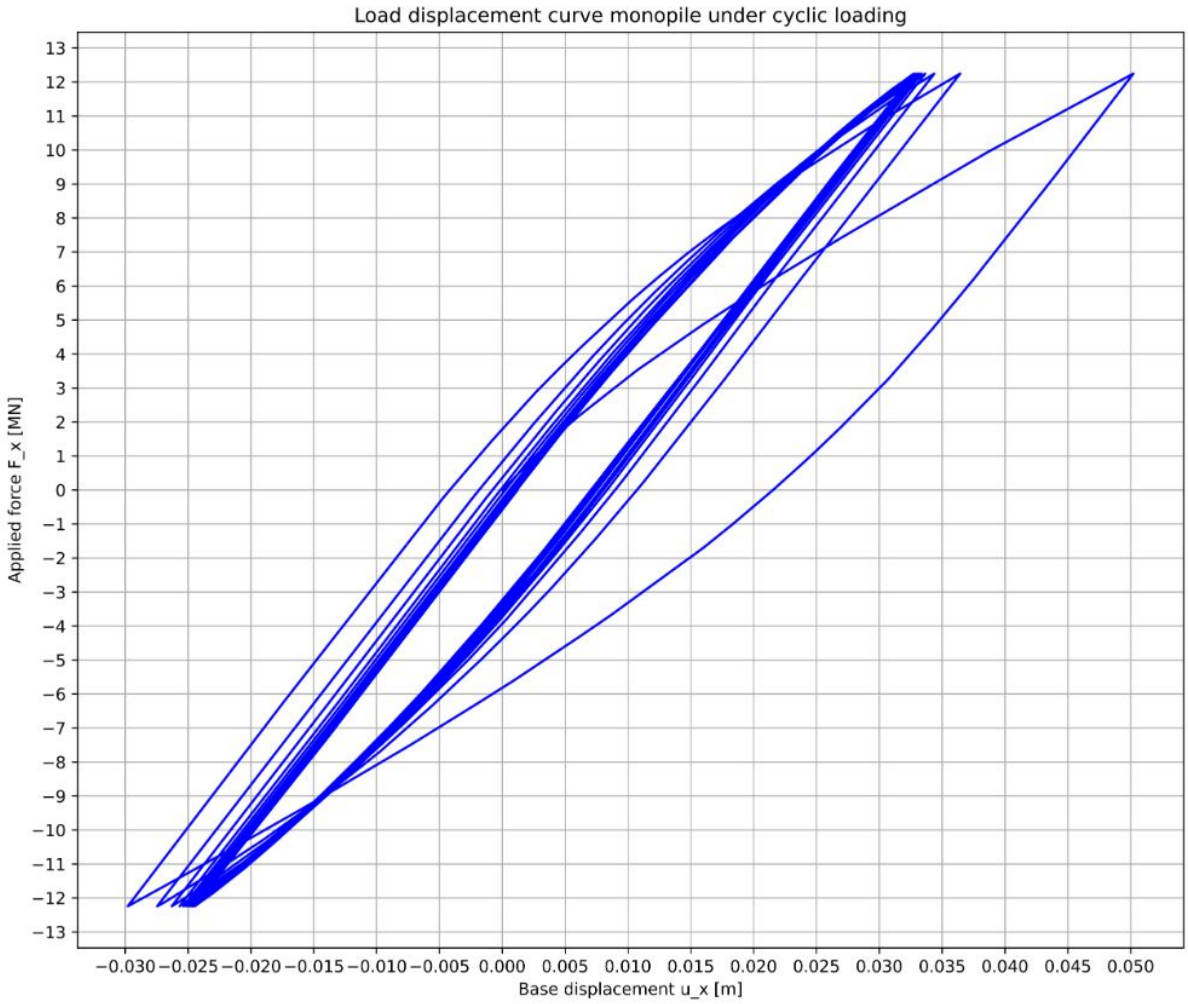

Figure 6.10: Force displacement curve at the base resulting from the cyclic loading analysis of the monopile model

A small accumulation of plastic deformations occurred during the analysis, as can be seen by the small shift to the right of the centre of the loops. However, this seems to decrease, which implies an increase in the stability of the system. This is beneficial for the long-term cyclic loading the system is subjected to. As the loops get smaller, less energy will be dissipated in each cycle. The response of the monopile will then be more elastic, which is beneficial for the wind turbine.

Caisson

In Figure 6.11 the force-displacement curve of the caisson is shown resulting from the cyclic analysis. Again, clear hysteresis loops can be seen. The first loop is the biggest loop, whereafter smaller loops follow. The loops are narrow, indicating a stiff response of the caisson and low energy dissipation over each loop. However, when zoomed in, a small increase in loop size appears as the cycles go on. This is a really small increase, which is insignificant.

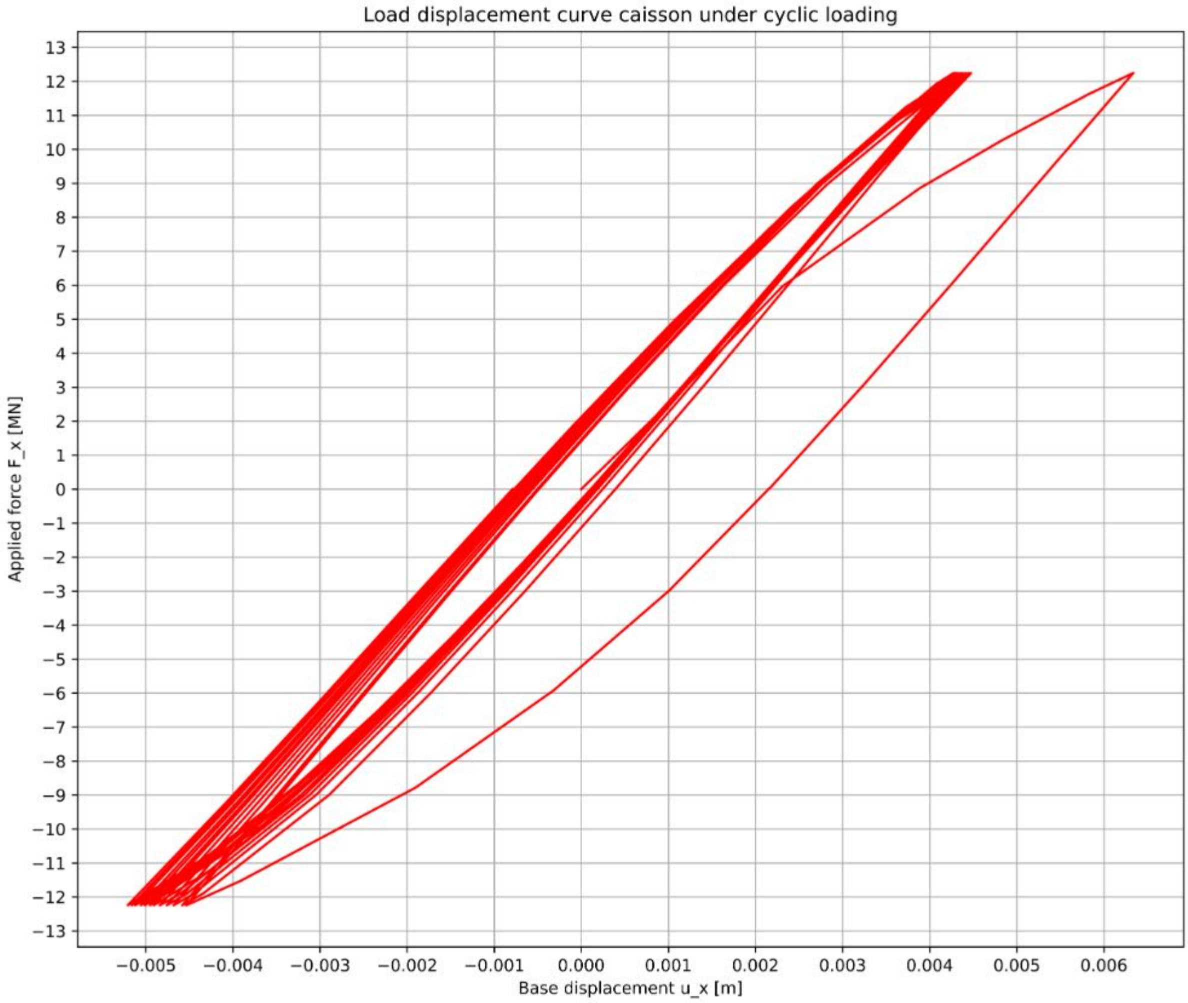

Figure 6.11: Force displacement curve at the base resulting from the cyclic loading analysis of the caisson model

This suggests that, despite some plastic deformation and energy loss, there are only slight changes in stiffness and structural behaviour. The caisson shows steady behaviour under cyclic loading with no development in deformations or softening of the soil.

In Figure 6.12 the force-displacement curves for the monopile and the caisson under cyclic loading are shown. In this Figure, the difference in stiffness between the caisson and the monopile is visible.

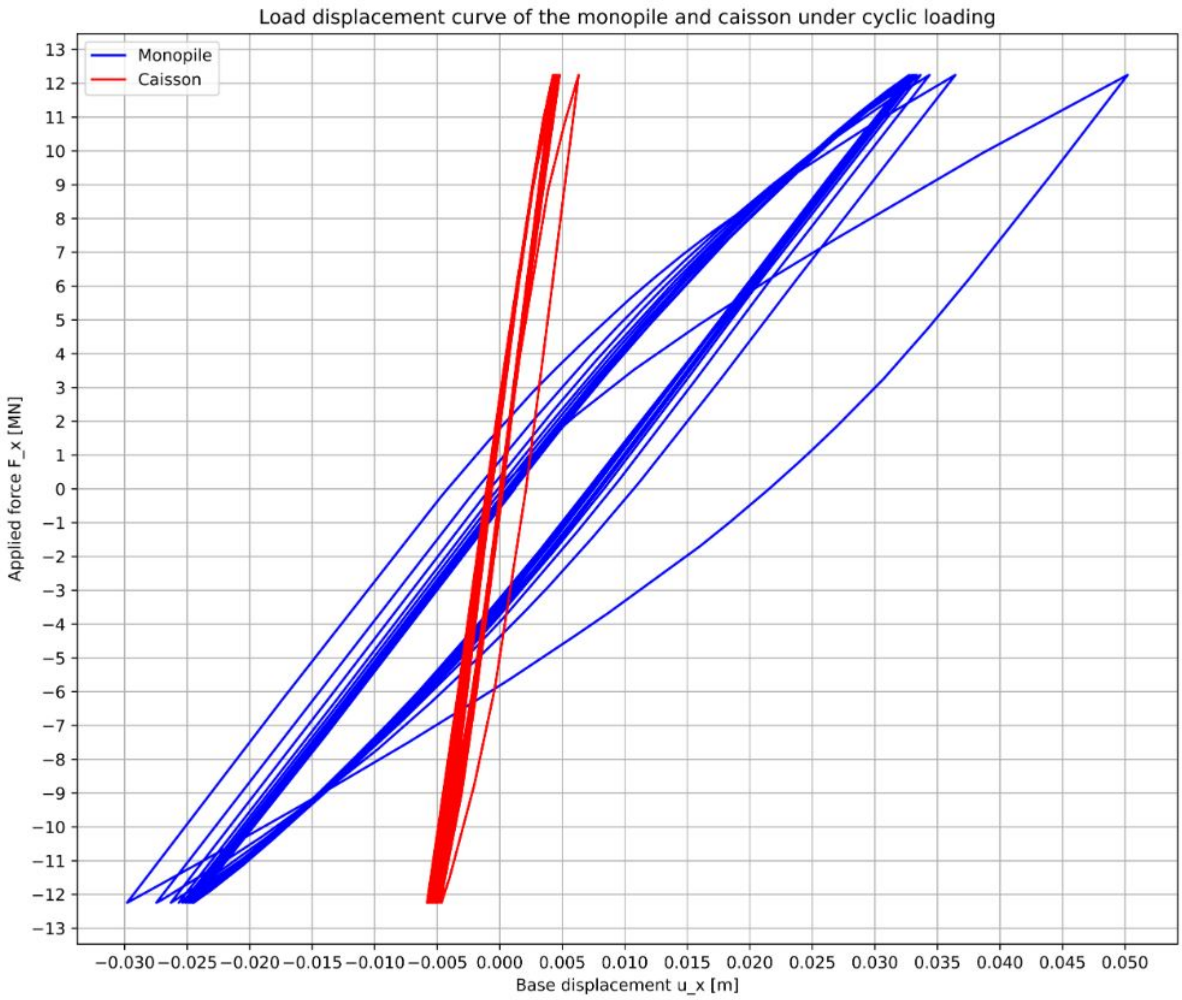

Figure 6.12: Force displacement curve at the base resulting from the cyclic loading analysis of the monopile and caisson model

Compared to the caisson, the monopile has a wider displacement range with the same forces, suggesting a higher flexibility. The caisson has more initial stiffness and lateral load resistance. As the cycles go on, the hysteresis loops of the monopile get a bit smaller, which reflects lower plastic deformation. However, as the caisson develops, the loops remain steady, besides a marginally small increase of the loops over the cycles. The caisson's stiffness appears to remain stable. The monopile loops show plastic deformation with a slight shift to the right with each cycle, but this shift reduces. When there is minimal residual displacement, the caisson maintains its centre and has minimal permanent displacement accumulation. The monopile's flexibility enables it to tolerate bigger displacements. The caisson provides a more stiff and rigid foundation reaction.

6.5.2. Shear-Stress Strain Curves

The effective shear-stress strain curves are computed on 4 points around the caisson and the monopile foundation. In Figure 6.13 the location of these points around the monopile and caisson is shown.

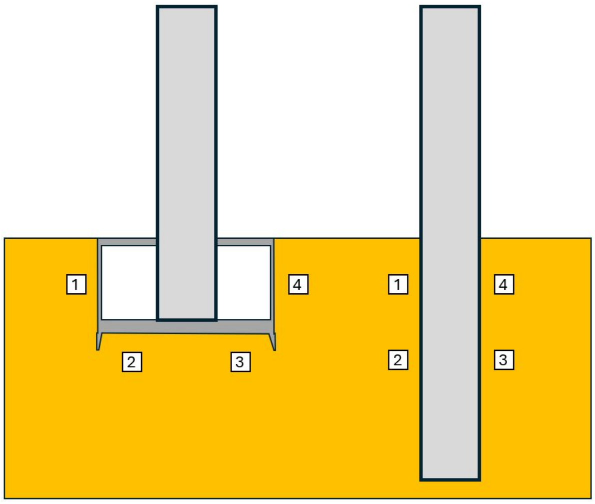

Figure 6.13: Locations of the points for which the shear-stress strain curves are computed

Monopile

Figure 6.14 shows the shear-stress strain curve of the monopile. The figure shows that points one and four, which are closer to the mudline, develop more strains because they are subjected to greater stress amplitudes. This implies that the impact of cyclic loading is lower deeper in the soil, leading to lower shear stresses and strains. While at points two and three, which lie deeper in the soil, the strains appear to recover during the unloading phases, the strains for points one and two continue to increase. Additionally, it can be claimed that points two and three have less accumulated strains because they are exposed to smaller stresses this is further supported by the fact that, in comparison to the top sand layers, the deeper sand deposit has a higher small-strain stiffness G_0 value. Following the applied loading scenario, points three and four on the right side are building positive strains, while the points on the left side are accumulating negative strains.

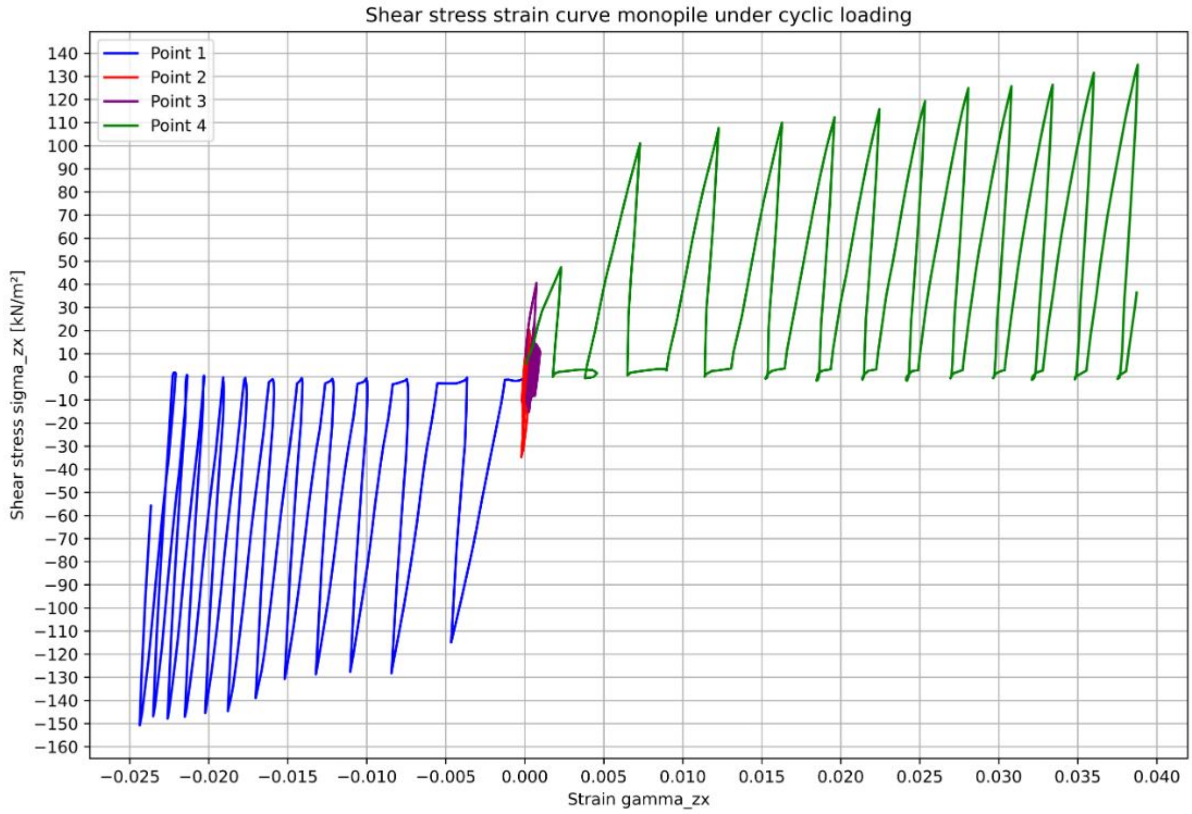

Figure 6.14: Shear-stress strain curve of the monopile under cyclic loading

A possible explanation for the fact that the strain increases when the shear stress is zero is a flaw in the soil model. This is the flaw of overshooting, uncontrolled reset of the loading memory, and regain of high initial stiffness after tiny unloading-reloading cycles. This needs to be researched further.

Caisson

In Figure 6.15 the shear-stress strain curve of the caisson is shown. For points one (blue) and four (green), the behaviour in the first cycles differs significantly from that in the following cycles. Permanent strains are produced in these cycles. After a couple of cycles, only very little difference exists between successive cycles, indicating a stabilisation of the stress-strain accumulation. Similar to the monopile, the points closer to the mudline develop more strains because they are subjected to greater stress amplitudes compared to the point deeper in the soil. The caisson shows lower overall shear-stress and strain values at the four points compared to the monopile. This implies a stiffer and more rigid reaction to lateral forces than the monopile. The cyclic loops at the mudline at points one (Blue) and four (Green) only increase slightly. The shear stress and strain are significantly smaller in comparison to the monopile. The loops at points one and four lose less energy and don't change much in shape. This indicates that the caisson near the mudline does not appear to have broken down or become more flexible over the cycles. Deeper in the soil, points two (Red) and three (Purple) show even smaller loops, indicating low stresses and strains and few cyclic effects. This implies that the caisson experiences almost no cyclic degradations.

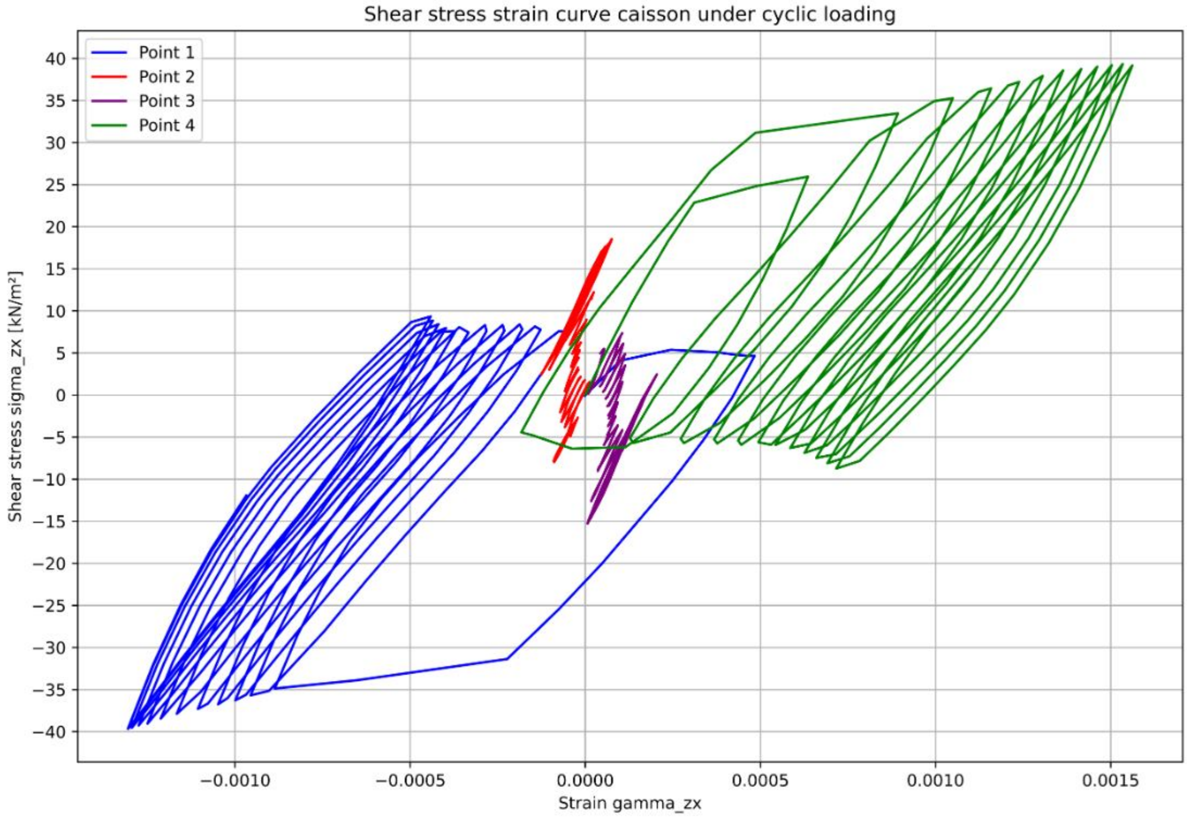

Figure 6.15: Shear-stress strain curve of the caisson under cyclic loading

A big difference is the shape of the shear-stress strain curves of the monopile and the caisson. The monopile shows a saw-tooth-like graph, while the caisson shows a more circular graph, more similar to the hysteresis loops. It implies that the caisson experiences a more stable plastic deformation with a soil-structure interaction that has a more even distribution of stresses and strains. The monopile foundation's stress-strain curve has rapid stress increases and decreases with corresponding strain changes. This pattern implies that under cyclic loading, the monopile foundation experiences consecutive stages of plastic and elastic deformation, resulting in sudden decreases after a sharp increase in stress. The non-linear reaction of the surrounding soil adds to the energy dissipation and possible stiffness degradation over time. However, this needs to be researched further.

6.5.3. Increasing Cyclic Loading

In this section, the results of the analysis where the amplitude of the loading increased after two cycles are given.

Figure 6.16 shows the force-displacement curve of the monopile under cyclic loading, of which the amplitude of forcing increased after every two cycles. As the cyclic load amplitude increases, the curve shows that the hysteresis loops gradually widen. Energy dissipation caused by soil damping and plastic deformation is indicated by the hysteretic behaviour. The nonlinear relationship between displacement and applied force is reflected in the geometry of the loops, indicating that the monopile experiences both plastic and elastic deformations. The displacement increases parallel with the load with each cycle, suggesting that the soil surrounding the monopile is accumulating deformations.

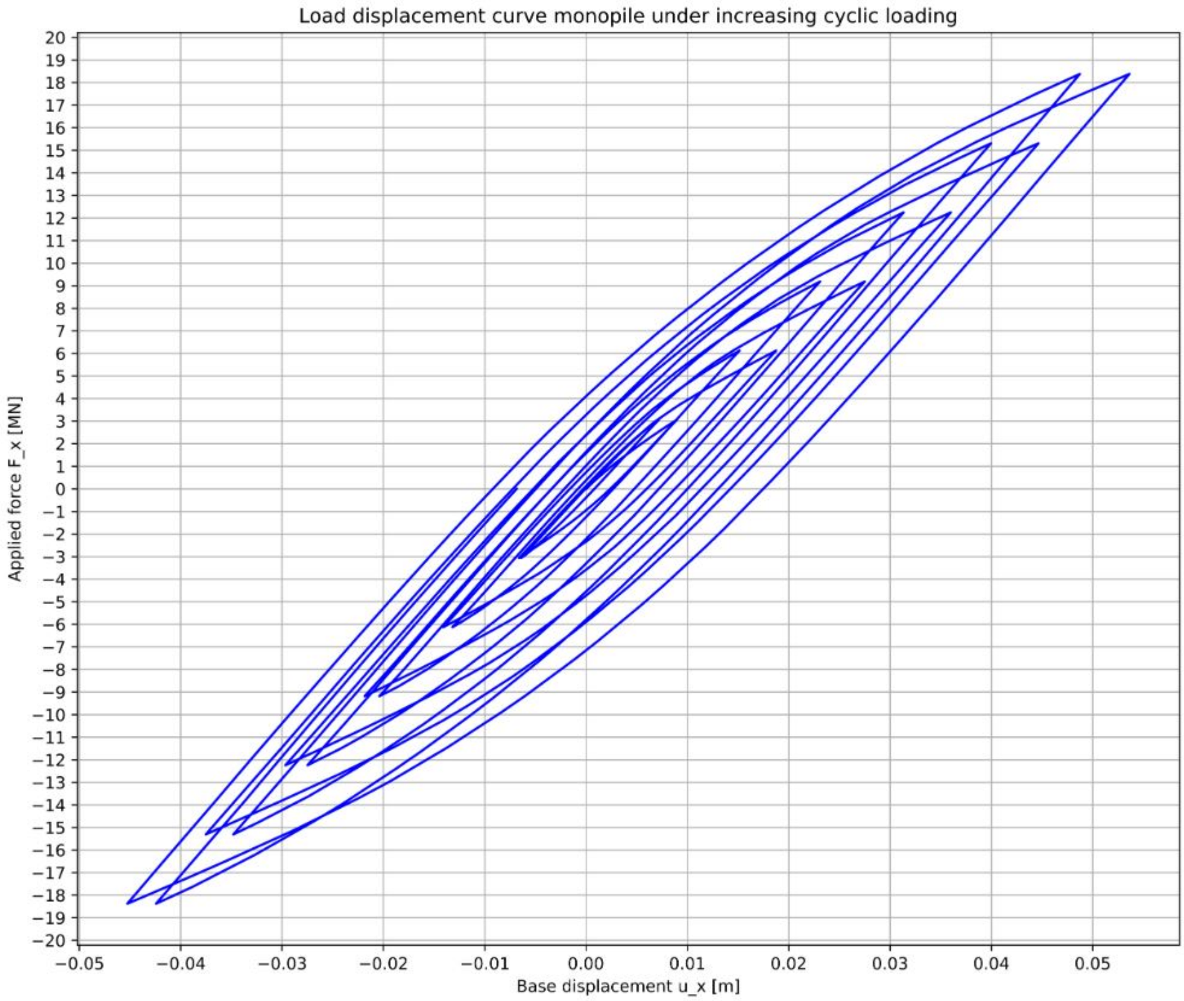

Figure 6.16: Force displacement curve of the monopile under increasing cyclic loading

Figure 6.17 shows the caisson's force-displacement curve under cyclic loading, of which the amplitude of forcing increased after every two cycles. The caisson shows similar hysteresis loops. However, these loops are tighter. In comparison to the monopile, the tighter loops suggest less energy dissipation and less plastic deformation. Since fewer displacements occur with the same force magnitude, the caisson's reaction suggests a higher stiffness. It appears that the caisson foundation offers more stability under cyclic loads since the accumulation of displacement is lower.

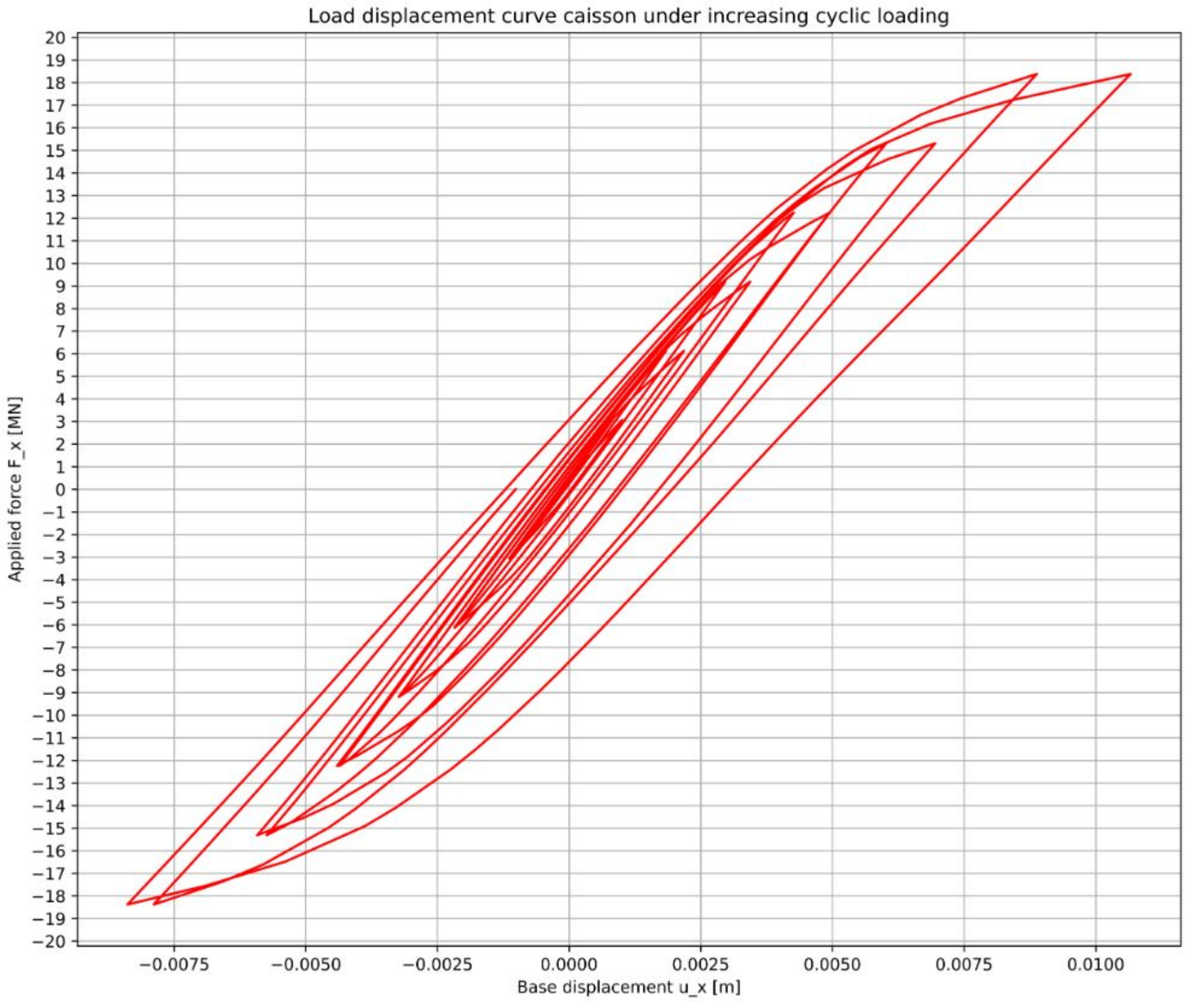

Figure 6.17: Force displacement curve of the caisson under increasing cyclic loading

Figure 6.18 shows the force-displacement curves of the monopile and caisson combined under cyclic loading, of which the amplitude of forcing increased after every two cycles. As can be seen in the figure, the cycles under higher forces show an asymmetric shape. In the unloading phases, the curves are linear. The asymmetric linear shape in later cycles indicates progressive plastic deformation and soil degradation. The differences between the two foundations are visible. Wider loops and larger displacements in the monopile suggest more plastic deformation and energy dissipation in the surrounding soil compared to the caisson. Under similar forcing, the caisson's steeper and smaller loops show increased rigidity and decreased displacements compared to the monopile.

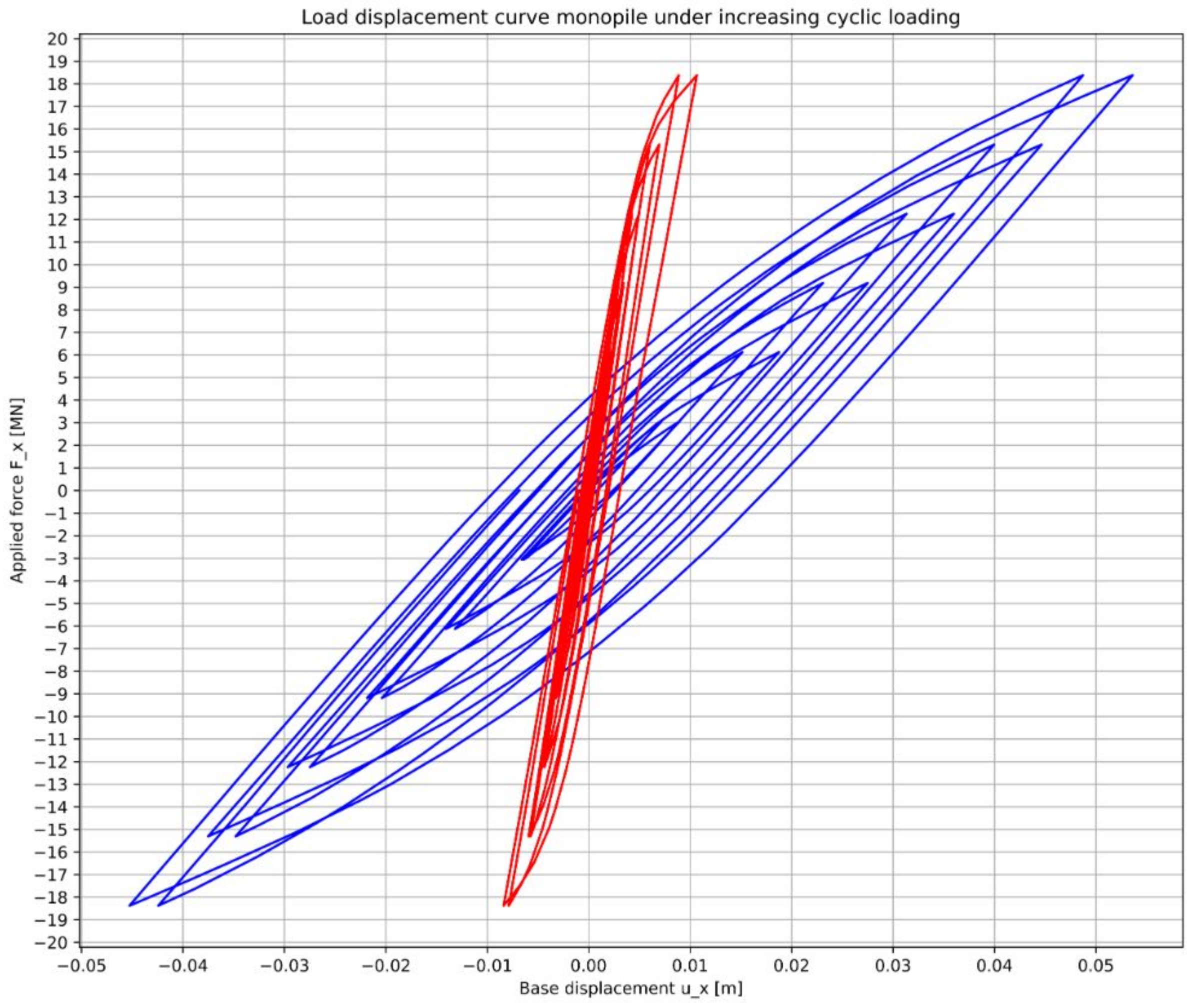

Figure 6.18: Force displacement curve of the monopile and caisson under increasing cyclic loading

The caisson foundation shows higher rigidity and stability, making it more resistant to cyclic loading of these amplitudes, whereas the monopile foundation experiences considerable plastic deformation and energy dissipation.

7

Practical Considerations in the Construction and Installation of the Caisson

In this chapter, the practical considerations of the caisson with its calculated dimensions are considered. First, an assessment is made about the buoyancy of the caisson. Second, the equations needed to figure out if it is possible to bring the caisson to the desired depth are made. Lastly, the limitations of the caisson are discussed. In this chapter, the dimensions of the caisson as stated in section 4.1.3 are used for the calculations since they appeared to be sufficient to withstand the applied forces according to Chapter 6.

7.1. Buoyancy of the Caisson

Here an assessment is made to see if the caisson would be able to float. The caisson will float if the downward force of the weight of the caisson is lower than the upward buoyant force of the water. The buoyant force is calculated according to the Archimedes principle. The total downward force of the caisson is equal to the volume of the concrete times the unit weight of concrete and the volume of steel used in the transition piece times the unit weight of steel.

$$F_{caisson} = V_{Concrete} \cdot \gamma_{Concrete} + V_{Steel} \cdot \gamma_{Steel} = 3898.7 \cdot 25 + 65.3 \cdot 78.5 = 102.6MN \tag{7.1}$$

To calculate the upward force, the Archimedes principle is used, as can be seen in equation 7.2. The buoyancy force is equal to the weight of the displaced water or seawater, depending on where the caisson will be produced. The volume of the displaced water is equal to the outer volume of the caisson plus the volume of the cutting edges. This displaced volume is equal to $9754m^3$.

$$F_a = \rho_{water} \cdot g \cdot V \tag{7.2}$$

Following equation 7.2 above, this results in an upward force of $98.1MN$ in seawater and $95.7MN$ in fresh water. Since the downward force of the caisson and transition piece, $102.6MN$, is higher than the upward force, $98.1MN$ or 95.7, the caisson will not float. Therefore, transporting by towing it into location is not an option, and the option to place it on a barge or semi-submersible needs to be used for transportation of the caisson, whereafter it will be lifted into place by cranes.

It could be favourable to research the option to lower the weight of the caisson since it would greatly decrease the transportation cost of the caisson if it can be towed into place by tugboats. An option could be to make the dimensions of the caisson bigger, so a higher upward force will be achieved. Here an optimisation can be helpful. Another option would be to investigate the option of using lightweight concrete. This will reduce the weight of the caisson and so the downward force.

7.2. Bringing the Caisson to Depth

After the caisson is transported to the desired location and placed on the seabed, the sinking of the caisson into the seabed needs to be done. In this section, a preliminary sinking calculation is made to give an overview of the important aspects during the sinking operations and to research if the caisson would be able to achieve the desired depth. Hereafter, an overview is given of the required materials that need to be installed to facilitate the sinking process.

7.2.1. Sinking Calculation

In this subsection, the sinking calculation is elaborated on. Here the necessary steps are elaborated on to investigate if the caisson will be able to reach the desired depth. The driving force of the sinking process, the force due to the self-weight of the caisson, is calculated first. Secondly, the forces that need to be overcome in order to sink the caisson are calculated. These are the friction forces between the wall of the caisson and the soil, the tip resistance at the cutting edges of the caisson, and the buoyant force due to the heightened air pressure in the working chamber. Lastly, a vertical equilibrium check is carried out to investigate if extra ballast is necessary to bring the caisson to the desired.

Self-Weight of the Caisson at the Moment of Sinking

First, the self-weight of the caisson is calculated. In Table 7.1 the volumes and calculated forces can be found.

Table 7.1: Self-weight of the caisson at the moment of sinking (Gc)

Part Name	Dimensions (m)			Volume (m³)	Quantity	Volumetric Weight (kN/m³)	Weight (kN)
	Height	Length	Width				
Roof	1.50	30.00	30.00	1350.0	1	25	33750
Space for the transition piece	1.50	8.86	-8.86	-117.7	1	25	-2944
Walls	6.50	29.00	1.00	188.5	4	25	18850
Floor	2.00	30.00	30.00	1800.0	1	25	45000
Transition piece	38.00	0.055	10.00	65.3	1	78.5	5126
Cutting edges	0.83	2.00	29.00	48.1	4	25	4814
Openings for shafts, etc.							-2000
Total self-weight of the caisson:							**102596**

Friction During Sinking

Here the wall friction of the caisson during the sinking process of the caisson is calculated. A lubricant such as bentonite is typically used to reduce skin friction, with the exception of the deepest two meters of the caisson. In this part, lubricant cannot be used to prevent soil blow-in during the sinking process. The active horizontal soil pressure coefficient λ_a, necessary to calculate soil stress in table 7.3, is calculated using the following formula according to NEN [44]:

$$\lambda_a = \frac{\cos^2(\varphi+\alpha)}{\cos\left(1+\sqrt{\frac{\sin(\varphi+\delta)\sin(\varphi-\beta)}{\cos(\alpha-\delta)\cos(\alpha+\beta)}}\right)} \tag{7.3}$$

For the wall friction during sinking, the maximum value of the friction angle (ϕ) is important. It is given by the following formula:

$$\delta_{\text{max}} = -\phi \tag{7.4}$$

In tables 7.2 and 7.3 the values for the maximum friction angle values and the stresses at critical levels can be found. In Table 7.4 the total calculated wall friction force is shown.

Maximum Friction Angle Values

Table 7.2: Maximum friction angle values

Layer Definition	ϕ (deg.)	a (deg.)	b (deg.)	δ (deg.)	λ_a	$\lambda_a \times \tan(\delta)$
Ground level to groundwater:	0	0	0	Bentonite lubricant		0.10
Groundwater level to top of cutting edge:	0	0	0			
Along the cutting edge:	38	0	0	-38	0.62	0.49

Stresses at Critical Levels

Table 7.3: Stresses at critical levels

Level Definition	Level (m)	γ (kN/m³)	h (m)	$\gamma \times h$ (kN/m²)	$\lambda_a \times \tan(\delta)$	q_w (kN/m²)
Ground level:	0.0	0.0	0.0	0.0	0.0	0.0
Groundwater level:	0.0	0.0	0.0	0	0.10	0.0
Top of cutting edge:	-10.0	10.0	10.0	100	0.10	10.0
	-10.0	10.0	10.0	100	0.49	48.5
Bottom of cutting edge:	-12.0	10.0	2.0	120	0.49	58.2

Total Wall Friction Force

Table 7.4: Total wall friction force

Level Definition	Level (m)	Length (m)	Width (m)*	h (m)	q_w (kN/m²)	Q_w (kN)
Ground level:	0.0	0.0	0.0	0.0	0.0	0.0
Groundwater level:	0.0	30.00	30.00	0.0	0.0	0
Top of cutting edge:	-10.0	30.00	30.00	10.0	10.0	6000
	-10.0	30.10	30.10	10.0	48.5	0.0
Bottom of cutting edge:	-12.0	30.10	30.10	2.0	58.2	12848
Total:						18848

The total wall friction force is equal to $F_{ww} = 18848kN$. This is a force that needs to be overcome during the sinking of the caisson

Resistance Against the Bottom of Cutting Edges

Here the resisting force at the tip of the cutting edges of the caisson is calculated. The effective length and width of the cutting edges are used for calculation since the cutting edge had a cut-out of $5cm$, these can be found in table 7.5. Here is the force calculated with a standard value of $100kN/m$ along the bottom of the cutting edges.

Table 7.5: Effective length and width of the cutting edge

Parameter	Value
Effective length	29.85 m
Effective width	29.85 m

The resistance against the bottom of the cutting edges (Fs) is calculated using the following formula:

$$Fs = 100 \cdot (\text{effective length} + \text{effective width}) \cdot 2 = 12040kN \tag{7.5}$$

Buoyancy Due to Water Pressure

In the working chamber, the water level is maintained by air pressure at approximately $20cm$ above the bottom of the cutting edges. This results in an upward buoyant force at the floor of the caisson. The effective length and width on which this buoyant force acts can be found in Table 7.6. The effective water height for upward water pressure is $11.8m$.

Table 7.6: Effective length and width for water pressure

Parameter	Value
Effective length	29.60 m
Effective width	29.60 m

The upward water pressure Fw at the desired depth of the caisson is $Fw = 102690kN$.

Vertical Equilibrium Check

In this section, the vertical equilibrium check is carried out to investigate if extra ballast needs to be added to bring the caisson to the desired depth. The equilibrium of force can be found in table 7.7

Table 7.7: Vertical equilibrium check

Downward Forces (kN)	Value	Upward Forces (kN)	Value
Self-weight of caisson	102596	Wall friction	18848
		Resistance against the bottom of cutting edges	12040
		Buoyancy due to water pressure	104789
Total downward	102596	**Total upward**	135677

The remaining force is an upward force of $33081kN$. This means that this force needs to be overcome in order to bring the caisson to the desired depth. In figure 7.1 an overview of the forces can be found. Here also the tipping point can be found on which depth the downward forces do not exceed the upward forces anymore. This point is found at a depth of $9.5m$.

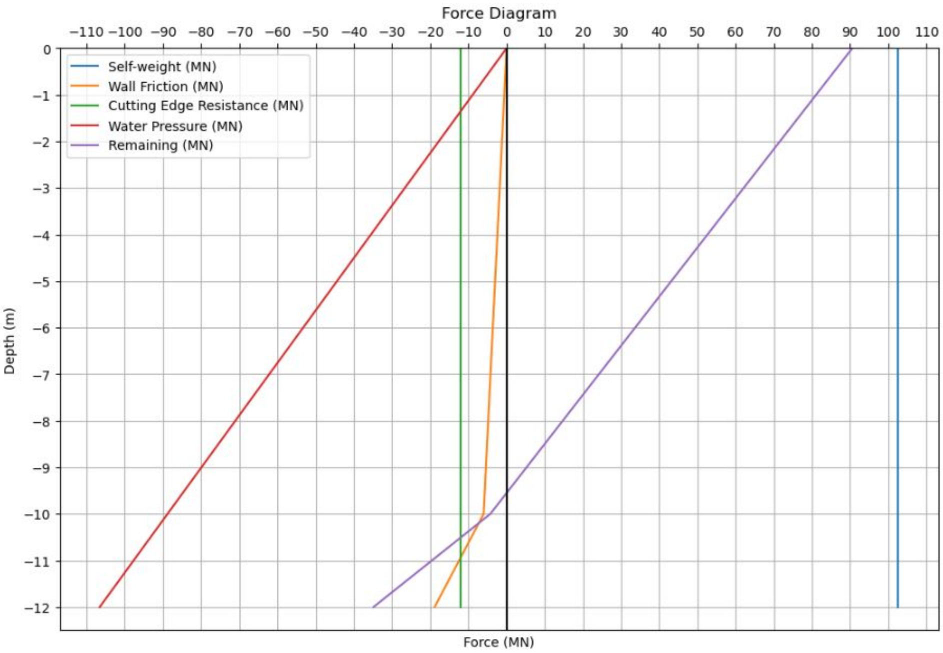

Figure 7.1: Force diagram of the forces during the sinking process

In practice, this can be solved by a temporary but fast reduction of the air pressure. By reducing the air pressure in the working chamber, the weight on the cutting edges on the ground increases and causes soil to collapse so that the caisson sinks further. In this case, the apparent solution would be to fill the hollow section in the caisson as shown in figure 2.8 with water. This will add additional weight to sink the caisson. The hollow section inside the caisson has a volume of $4310.6m^3$. This means an extra ballast of $43.3Mn$ can be added to the caisson if the hollow section is filled with seawater.

The working chamber is empty at the time of sinking. When the caisson is at depth, the chamber has to be filled. Normally this is done with concrete. At sea, this is difficult to do because a concrete plant is not common at sea, and transport is also difficult. Therefore, the obvious solution is to fill the working chamber with sand. This also brings an advantage when the foundation of the turbines has to be decommissioned [1].

7.2.2. Limitations

When installing the caisson to a depth of twelve meters under the seabed where the water level is 25 meters, the pressure is 3.7 bar corresponding to a water depth of 37 meters. Operational durations of labour at this depth are constrained, necessitating an alternative breathing mixture at the time at which maintenance or dismounting of the equipment in the working chamber takes place. It is aimed to minimise the amount of time that people are at work in this scenario because operating at higher air pressure lengthens the decompression period.

8 Conclusion

In this chapter, the research will be concluded by providing an answer to the questions stated in the research objective. The conclusion to this research can be seen as advice for individuals or companies interested in designing and building pneumatic caisson foundations.

This thesis investigated the performance of a pneumatic caisson foundation compared to a monopile foundation for offshore wind turbines The main focus was on soil-structure interactions and structural behaviours under various load scenarios. The results of the analysis imply that pneumatic caissons are suitable for offshore applications since they can withstand forces similar to those of monopiles while displaying greater rigidity and fewer displacements.

The monopile and the pneumatic caisson foundations are subjected to vertical forces from the weight of the turbine as well as lateral forces from the wind, waves, and current. The maximal environmental forces were calculated and exerted on the different models.

Analysis of monotonic behaviour from the pushover analysis showed that the caisson reaches the elastoplastic and non-linear behaviour transition at a lower force exerted on the structure in comparison with the monopile. However, the elastic capacity of the caisson appeared to be sufficient to support the applied loads. The monopile shows a longer linear elastic range before deforming non-linearly compared to the caisson. Nevertheless, both structures have appropriate load-bearing capacity to withstand the maximal environmental loads. Further analysis showed that, compared to the monopile, the caisson had a stiffer structural response to the applied forces. The caisson was able to handle the maximum calculated environmental force levels with smaller displacements compared to the monopile.

The results of the free vibration analysis and the Fast Fourier Transform showed that the natural frequencies of both foundation types fall within the soft-stiff range and do not overlap with the frequencies of the waves in the JONSWAP spectrum and the wind from the Kaimal spectrum, so resonance with the forcing frequencies is unlikely to occur. In addition, the natural frequency of the caisson is slightly higher than the natural frequency of the monopile. This is because of the higher stiffness of the caisson.

The caisson maintained structural stability with few permanent deformations under the cyclic loading scenarios. The caisson had a steady cyclic response with small and constant hysteresis loops, indicating a stiff response and little energy dissipation. Almost no cyclic degradation was shown, which indicates robustness against the constant cyclic loads on offshore wind turbines. In contrast, the monopiles showed more flexibility and energy dissipation via bigger hysteresis loops, showing a higher damping potential compared to the caisson. This indicates that while the monopile can absorb more energy, it may experience higher strains or deformations compared to the stiffer response of the caisson. In addition, the monopile showed a shrinking of the hysteresis loops over the cycles, which implies an increase in soil stiffness over the cycles that increases the soil stability.

The significant dimensions and mass of the caisson require the use of specialised production facilities with direct access to the sea. At the Verolme shipyard, Bougainville yard, or Barendrecht port, a large caisson can be built on a site with direct water access. The weight of the caisson surpasses the buoyancy, making floating transport impossible. Thus, the caisson must be transported by barge or by a semi-submersible vessel. For the last part of sinking, the caisson needs to overcome the friction forces at the walls and the buoyant force. By adding extra ballast, the caisson can be sunken to the desired depth. For decommissioning, first, the working chamber needs to be emptied again. Next, the caisson is lifted out of the seabed by repressurising the working chamber together with draining the water from the hollow section of the caisson to overcome the sinking forces of the caisson.

Lastly, to conclude this thesis, the main research question will be answered:
"To what extent is a pneumatically submerged caisson a viable and feasible alternative as a foundation of an offshore wind turbine compared to the monopile foundation?"

The pneumatic caisson foundation is a viable and feasible alternative to the current monopile foundation for offshore wind turbines. It is a promising option because it can provide lower displacements under maximal environmental loading compared to the monopile. Additionally, it exhibits a stable response to both monotonic and cyclic forces. Furthermore, it is possible to install the caisson with low vibration and noise levels. This gives the caisson an advantage over the monopile, as its lower noise and vibration levels during installation result in reduced disturbance to marine life, making it more suitable for use in environmentally sensitive areas. The caisson is a strong contender for offshore wind turbine foundations by focusing on soil-structure interactions and associated soil behaviour, as it shows a higher initial load-bearing capacity due to its stiffness and stability under cyclic and monotonic loading scenarios. The caisson's strength is derived from its stiffness, which effectively prevents displacements, in contrast to the monopile's strength, which is derived from flexibility that allows for more displacements. Therefore, the caisson is a potential foundation solution that holds its specific characteristics.

This study examined the stability performance of pneumatic caisson foundations in comparison to monopile foundations for offshore wind turbines. However, the economic viability of employing caisson foundations offshore requires additional investigation. The installation of a pneumatic caisson may require more time compared to the installation of monopiles. The installation of caissons could increase offshore operational expenses, including vessel time and manpower, hence reducing the cost-effectiveness. The economic feasibility of the pneumatic caisson method in the offshore environment remains to be examined.

9 Discussion

In this chapter, issues encountered when trying to answer the research questions will be evaluated. First, the possible improvements in the research will be elaborated on. Together, the improvements and inaccuracies that were encountered during the study are stated. Lastly, recommendations for follow-up studies and improvements are given in this chapter.

In practice, during the excavation of the caisson, a spacing of 5 cm between the caisson and the soil is filled with bentonite flushing to lower the friction between the soil and the wall. In this thesis, the bentonite flushing is not taken into account. However, it is important to state this since it could impact the friction resistance, resulting in a lower overall stability of the caisson. In practice, it would be possible to expel the bentonite flushing from the spacing. For example, by injecting grout into the spacing. This would increase the friction of the caisson and the surrounding soil to a level equal to if there is soil in the spacing. However, this will make decommissioning of the caisson more difficult. Further research is advised on how to deal with bentonite flushing and how it will affect the frictional resistance of the caisson. This could, for example, be added to the Plaxis model.

For the modelling of the monopile, transition piece, and tower the average steel thickness is used. Therefore, the centre of gravity of the wind turbine will be lower in reality than in the model. This could influence the accuracy of the free vibration analysis and the calculated natural frequencies and damping ratios. By dividing the wind turbine into more segments, this problem could be overcome in any further calculations with the model.

The expected response from the dynamic boundary conditions was not observed. There was still a significant displacement at the viscous dynamic boundary combined with the normally fixed deformation boundary condition. Therefore, it was decided to remove the dynamic boundaries and significantly enlarge the mesh. In this case, the soil damped any vibrations before they reached the mesh's boundaries. Although this was acceptable, this issue could be looked into further in case other dynamic calculations are made with these models.

During the calculation of the different phases in the cyclic analyses, mesh imperfections occurred during the later phases where higher loads were applied to the structure. Large peaks in the mesh occurred at the interface between the caisson structure and the soil. This indicated a meshing or numerical problem. After multiple attempts to refine the mesh to fix this issue, the peaks became smaller. However, the peaks did not completely disappear. Most likely, this affected the results. Further research into the problem is advisable to increase the reliability of soil-structure interactions predicted by the model.

There was no distinction made between the ULS and SLS loading conditions in this thesis. The objective of this study was to examine the variations in the behaviour of soil structure interaction between the different foundation types instead of focusing on the ULS and SLS conditions for the final caisson design. In this study, the maximal environmental force that could occur was calculated based on existing data and with a chosen return period of 50 years. For future calculations or designs of the caisson, it would be advised to examine the different SLS and ULS loading cases that could occur.

No optimisation of the caisson's dimension has been made. The initial dimensions of the caisson appeared to be sufficient to withstand the forces exerted on the structure. An optimal caisson dimension to find the most economical design but still withstand all the forces exerted on the structure can be found. This could also be designed in a way that the caisson would have enough buoyant force to float on its own and the caisson could be towed to the desired position. This would save costs on expensive transportation vessels and cranes.

For further research, it is advised to investigate what the soil-structure interaction will be if the caisson is embedded deeper into the seabed and the ceiling of the caisson is covered with soil. Now only one configuration was investigated. If the caisson is embedded deeper, the surface of the caisson will interact with the stiffer surrounding soil, which will divide the forces more evenly into the soil, extending the linear behaviour of the caisson and preventing early plastic deformations. Significant cost benefits are expected to be gained in optimising the caisson design.

The most critical point is expected to be the connection of the transition piece with the caisson. At this connection, a lot of forces and stresses will act. At this point also a transition between materials, from steel to concrete, takes place. This results in a transition in the stiffness of the materials and is therefore expected to be a critical point in the design.

Fatigue was outside the scope of this thesis. However, this is an important factor to take into account. Concrete has lower fatigue resistance than steel. Also, due to the differences in material properties between concrete and steel, it is most likely that connections between the steel transition piece and the steel monopile are prone to fatigue failure. It is advised to do thorough research into the fatigue of the structure, especially focusing on the connection between steel and concrete. Also, the fatigue of the wind turbine itself needs to be examined in this case since the stiffness of the foundation affects the fatigue resistance of the wind turbine on top.

In section 6.1 it is stated that the structure would have failed if the lateral base displacement was bigger than the diameter of the monopile or transition piece divided by ten. Due to the different characteristics of the monopile and the caisson, it may be questioned if this rule of thumb also applies to a concrete caisson. It was assumed the caisson would fail as soon as the rotation point of the caisson moved away from the centre line of the structure due to plastic deformation and the nonlinear behaviour that occurs when this happens. This will take additional research into the failure behaviour of concrete caissons to determine whether this is a correct assumption.

In the models, no structural damping was assigned to the structural elements of the monopile and the caisson. Therefore, the results of the logarithmic decrement method performed on the free vibration showed low values for the damping ratio and the logarithmic decrement. These values are not realistic. To improve the model, structural damping needs to be added to the structural elements of the caisson and the monopile. Besides structural damping, other sources of damping can be investigated and added to the model to generate more realistic results.

Lastly, the economic feasibility of the pneumatic caisson method in the offshore environment remains to be examined. Costs were not taken into account in this thesis. Further research is required into the economic feasibility of the pneumatic caisson as the foundation for an offshore wind turbine. The monopile can be installed relatively quickly. It needs to be investigated how long the installation of the caisson will take in the offshore environment. Also, the equipment necessary to install the caisson and the transportation to the offshore location are expensive. The combination of these factors will determine if the caisson could be an economically viable alternative compared to the monopile.

9.1. Recommendations for Follow-Up Studies

Multiple follow-up studies are recommended to improve this study's conclusions. A summary of the several recommendations for follow-up studies is provided. The impact of the bentonite flushing on the caisson's frictional resistance and stability should be studied and maybe implemented into the Plaxis models. To investigate other soil-structure interactions and design efficiencies, different caisson configurations and designs should be studied. For example, deeper caisson embedment in the seabed can be studied. A fatigue study should be carried out to investigate the influence of the caisson foundation on the fatigue resistance of the complete structure. The main focus could be on the steel-concrete connection, which is expected to be vulnerable to cyclic loads. The vibration analysis results can be made more realistic by adding structural damping and other damping sources into the Plaxis models. This would result in a more accurate determination of natural frequencies and damping ratios. Research on the economic feasibility of the caisson needs to be done. Caisson installation, transportation, and equipment requirements should be compared to monopiles. Further research into concrete caisson failure mechanisms under severe loads and a lifetime comparison of caissons and monopiles would help determine their sustainability and cost-effectiveness.

This research could open up opportunities for caissons to be used as a possible offshore wind turbine foundation option. By expanding the understanding of the practical applications and tackling challenges with implementation, this study contributes to the development of offshore wind energy technologies. As a foundation for further study and development, the knowledge gathered from this thesis shows the potential of pneumatic caissons to enhance the stability and durability of wind turbine foundations. This work lays the foundation for future developments that could introduce a new and less harmful alternative for marine life in offshore wind energy foundations.

References

[1] B. Admiraal. *Personal communication on practical consideration for caisson installments*. Conversation, October 15, 2024. Oct. 2024.

[2] Bartho Admiraal and Antoine Feddema. "PNEUMATISCH AFZINKEN 2.0: EEN WERELDRECORD CAISSONPROJECT DOOR GROOTSCHALIGE INNOVATIES". In: (Nov. 2023). URL: https://www.vakbladgeotechniek.nl/pdf-archief/jaargang-27-2023-nummer-4.

[3] Bartho Admiraal and Martijn van Wijngaarden. *Pneumatische caissonmethode*. May 2020. URL: https://www.cementonline.nl/pneumatische-caissonmethode.

[4] Sergio Avila-Sanchez et al. "Foundations in Offshore Wind farms: Evolution, characteristics and range of use. Analysis of main dimensional parameters in monopile foundations". In: *Journal of Marine Science and Engineering* 7.12 (Dec. 2019), p. 441. DOI: 10.3390/jmse7120441. URL: https://doi.org/10.3390/jmse7120441.

[5] BarendrechtNU. *Video over 'Bouwdok Barendrecht' langs de Oude Maas*. 2018. URL: https://barendrechtnu.nl/nieuws/historie/23969/video-over-bouwdok-barendrecht-langs-de-oude-maas.

[6] Thomas Benz. "Small-Strain Stiffness and Damping in Soil Models". PhD Thesis. Stuttgart, Germany: University of Stuttgart, 2007.

[7] *Betonvoet voor windturbines op zee*. July 2017. URL: https://www.deingenieur.nl/artikel/betonvoet-voor-windturbines-op-zee.

[8] *Blyth wind farm - EDF Renewables*. July 2022. URL: https://www.edf-re.uk/our-sites/blyth/.

[9] George Bocharov. *pyextremes: Extreme Value Analysis (EVA) in Python*. https://pypi.org/project/pyextremes/. Accessed: 2024-11-19. 2024.

[10] J.W. Bosch, G. Arends, and W. Broere. *Use of underground space*. Jan. 2011. URL: https://repository.tudelft.nl/view/MMP/uuid:0d24a9aa-da35-4db4-a7e1-8573c1a480f2.

[11] Miriam Brandt et al. "Responses of harbour porpoises to pile driving at the Horns Rev II offshore wind farm in the Danish North Sea". In: *Marine Ecology Progress Series* 421 (Jan. 2011), pp. 205–216. DOI: 10.3354/meps08888.

[12] R. Brinkgreve, M Kappert, and P Bonnier. "Hysteretic damping in a small-strain stiffness model". In: (Apr. 2007). DOI: 10.1201/NOE0415440271.ch106.

[13] Ronald Brinkgreve. *The Hardening Soil Model: Advanced Material Modeling in PLAXIS*. https://blog.bentley.com/software/the-hardening-soil-model/. Accessed: 2024-11-25. Feb. 2021.

[14] Rick Bruintjes et al. "The impact of experimental impact pile driving on oxygen uptake in black seabream and plaice". In: vol. 27. Jan. 2016, p. 010042. DOI: 10.1121/2.0000422.

[15] W. Carswell et al. "Foundation damping and the dynamics of offshore wind turbine monopiles". In: *Renewable Energy* 80 (2015), pp. 724–736. ISSN: 0960-1481. DOI: https://doi.org/10.1016/j.renene.2015.02.058. URL: https://www.sciencedirect.com/science/article/pii/S0960148115001743.

[16] Subrata Kumar Chakrabarti. *Hydrodynamics of offshore structures*. WIT press, 1987.

[17] CodeCogs. *JONSWAP - Spectra - Waves - Fluid Mechanics - Engineering in C, C++*. Accessed: 2024-11-20. 2012. URL: https://www.codecogs.com/library/engineering/fluid_mechanics/waves/spectra/jonswap.php.

[18] Marcin Cudny and Andrzej Truty. “Refinement of the Hardening Soil model within the small strain range”. In: *Acta Geotechnica* 15.8 (2020), pp. 2031–2051. ISSN: 1861-1133. DOI: 10.1007/s11440-020-00945-5. URL: https://doi.org/10.1007/s11440-020-00945-5.

[19] Daiho Corporation. *Outline of Pneumatic Caisson Civil Engineering Business Technology & Solution Daiho Corporation*. Dec. 2022. URL: https://www.daiho.co.jp/en/tech/civil_eng/nk/.

[20] Damen Shiprepair and Conversion. *Damen Verolme Rotterdam*. 2024. URL: https://www.damen.com/companies/shiprepair/damen-verolme-rotterdam.

[21] DHI Group. *Metocean On Demand*. Accessed: 2024-11-04. 2024. URL: https://www.metocean-on-demand.com/.

[22] DNV. *DNV-ST-0437: Loads and site conditions for wind turbines*. Tech. rep. Nov. 2016.

[23] Empire engineering. *The Empire Engineering Guide to Offshore Wind Foundations 2023*. Second edition. 2023. URL: https://www.empireengineering.co.uk/wp-content/uploads/2023/07/Empire-Engineering-Guide-to-Offshore-Wind-Updated-compressed.pdf.

[24] Torsten Faber. “Tower and Foundation”. In: *Wind Power Technology: An Introduction*. Ed. by Alois Peter Schaffarczyk. Cham: Springer International Publishing, 2023, pp. 291–318. ISBN: 978-3-031-20332-9. DOI: 10.1007/978-3-031-20332-9_7. URL: https://doi.org/10.1007/978-3-031-20332-9_7.

[25] B. Feddema. *Personal communication on soil parameters for the hardening soil small strain model*. Conversation, August 21, 2024. Oct. 2024.

[26] Fugro. *Geotechnical Parameters Hollandse Kust (noord) Wind Farm Zone Dutch Sector, North Sea*. Tech. rep. P903749/06 (7). June 2019.

[27] Evan Gaertner et al. *Definition of the IEA Wind 15-Megawatt Offshore Reference Wind Turbine*. Tech. rep. 5. Mar. 2020, p. 052052. URL: https://www.nrel.gov/docs/fy20osti/75698.pdf.

[28] K. Hasselmann et al. *Measurement of Wind-Wave Growth and Swell Decay during the Joint North Sea Wave Project (JONSWAP). Suppl. A*. Deutches Hydrographisches Institut, 1973.

[29] Anthony D. Hawkins, Louise Roberts, and Samuel Cheesman. “Responses of free-living coastal pelagic fish to impulsive sounds”. In: *The Journal of the Acoustical Society of America* 135.5 (May 2014), pp. 3101–3116. DOI: 10.1121/1.4870697. URL: https://doi.org/10.1121/1.4870697.

[30] James E. Herbert-Read et al. “Anthropogenic noise pollution from pile-driving disrupts the structure and dynamics of fish shoals”. In: *Proceedings - Royal Society. Biological sciences/Proceedings - Royal Society. Biological Sciences* 284.1863 (Sept. 2017), p. 20171627. DOI: 10.1098/rspb.2017.1627. URL: https://doi.org/10.1098/rspb.2017.1627.

[31] J.A Hildebrand. “Anthropogenic and natural sources of ambient noise in the ocean”. In: *Marine Ecology-progress Series - MAR ECOL-PROGR SER* 395 (Dec. 2009), pp. 5–20. DOI: 10.3354/meps08353.

[32] Guy Houlsby, Lars Ibsen, and Byron Byrne. “Suction Caissons for Wind Turbines”. In: *Int Symp Front Offshore Geotech* 75 (Aug. 2005). DOI: 10.1201/NOE0415390637.ch4.

[33] M. James and S. Haldar. “Design Strategies of Offshore Wind Turbines in Shallow and Deep Water-Indian Perspective”. In: *Indian Geotech Journal* 54 (2024), pp. 1999–2014. DOI: 10.1007/s40098-024-01021-5. URL: https://doi.org/10.1007/s40098-024-01021-5.

[34] Christopher Jung and Dirk Schindler. “The role of the power law exponent in wind energy assessment: A global analysis”. In: *International Journal of Energy Research* 45.6 (2021), pp. 8484–8496. DOI: https://doi.org/10.1002/er.6382. eprint: https://onlinelibrary.wiley.com/doi/pdf/10.1002/er.6382. URL: https://onlinelibrary.wiley.com/doi/abs/10.1002/er.6382.

[35] Madjid Karimirad. “Wave and Wind Theories”. In: *Offshore Energy Structures: For Wind Power, Wave Energy and Hybrid Marine Platforms*. Cham: Springer International Publishing, 2014, pp. 165–186. ISBN: 978-3-319-12175-8. DOI: 10.1007/978-3-319-12175-8_8. URL: https://doi.org/10.1007/978-3-319-12175-8_8.

[36] Evangelos Kementzetzidis. *Personal communication on rayleigh damping as a soil parameter*. Conversation, October, 2024. Oct. 2024.

[37] Faseel Khan. *Considerations for modelling a thick slab as a plate*. Apr. 2024. URL: https://bentleysystems.service-now.com/community?id=kb_article_view&sysparm_article=KB0108507.

[38] Rasmus Tofte Klinkvort et al. "A consistent, rigorous and super fast monopile design approach". In: Aug. 2020.

[39] Fachun Lai et al. "A new installation technology of large diameter deeply-buried caissons: Practical application and observed performance". In: *Tunnelling and underground space technology (Print)* 125 (July 2022), p. 104507. DOI: 10.1016/j.tust.2022.104507. URL: https://doi.org/10.1016/j.tust.2022.104507.

[40] Abdollah Malekjafarian et al. "Foundation damping for monopile supported offshore wind turbines: A review". In: *Marine Structures* 77 (2021), p. 102937. ISSN: 0951-8339. DOI: https://doi.org/10.1016/j.marstruc.2021.102937. URL: https://www.sciencedirect.com/science/article/pii/S0951833921000058.

[41] Adnan Memija. *First Gravity-Based Foundation Loaded and Ready for Fécamp Site*. 2022. URL: https://www.offshorewind.biz/2022/07/01/first-gravity-based-foundation-loaded-and-ready-for-fecamp-site/.

[42] *Monopiles & transition pieces*. May 2024. URL: https://sif-group.com/en/monopiles-and-transition-pieces/.

[43] C. Mueller-Blenkle et al. *Effects of Pile-driving Noise on the Behaviour of Marine Fish*. Tech. rep. COWRIE Ref: Fish 06-08, Technical Report, 2010.

[44] NEN. *NEN-EN 1997- 1+C1+A1: Eurocode 7: Geotechnisch ontwerp - Deel 1: Algemene regels*. Tech. rep. ICS 91.080.01; 93.020. June 2016.

[45] A. Niemunis and M. Cudny. "Discussion on "Dynamic soil-structure interaction: A three-dimensional numerical approach and its application to the Lotung case study". Poor performance of the HSS model". In: *Computers and Geotechnics* 98 (2018), pp. 243–245. ISSN: 0266-352X. DOI: https://doi.org/10.1016/j.compgeo.2018.02.003. URL: https://www.sciencedirect.com/science/article/pii/S0266352X18300314.

[46] Tomoyuki Oyake et al. "CHARACTERISTICS AND THEORIES OF THE PNEUMATIC CAISSON METHOD". In: *Conference on Our World in Concrete & Structures* (Aug. 2017). URL: https://www.orsc.co.jp/english/tec/con03.html.

[47] Fang-Le Peng et al. "Remote-control technology performance for excavation with pneumatic caisson in soft ground". In: *Automation in Construction* 105 (2019), p. 102834. ISSN: 0926-5805. DOI: https://doi.org/10.1016/j.autcon.2019.102834. URL: https://www.sciencedirect.com/science/article/pii/S092658051930127X.

[48] *Pneumatisch afzinken VSF*. URL: https://www.vsf.nl/nl/funderingen/caissons-en-luchtdruktechnieken/pneumatisch-afzinken.

[49] *Reference Manual 3D*. Bentley, Dec. 2023. URL: https://bentleysystems.service-now.com/sys_attachment.do?sys_id=d23b12ca87ec1e98abaf2fc6cebb357d.

[50] Louise Roberts et al. "Sensitivity of the mussel Mytilus edulis to substrate-borne vibration in relation to anthropogenically-generated noise". In: *Marine Ecology Progress Series* 538 (Oct. 2015). DOI: 10.3354/meps11468.

[51] P. Robertson. "Interpretation of cone penetration tests - A unified approach". In: *Canadian Geotechnical Journal* 46 (Nov. 2009), pp. 1337–1355. DOI: 10.1139/T09-065.

[52] P. K. Robertson and K. L. Cabal. *Guide to Cone Penetration Testing for Geotechnical Engineering*. 6th. Corporate Headquarters: 2726 Walnut Avenue, Signal Hill, California 90755. Telephone: (562) 427-6899. Fax: (562) 427-3314. E-mail: info@greggdrilling.com. Website: www.greggdrilling.com. Signal Hill, California: Gregg Drilling & Testing, Inc., 2015.

[53] RVO. *New offshore wind farms*. May 2024. URL: https://english.rvo.nl/topics/offshore-wind-energy/new-offshore-wind-farms.

[54] RVO. *Offshore Wind Energy Plans 2030-2050*. July 2021. URL: https://english.rvo.nl/topics/offshore-wind-energy/plans-2030-2050.

[55] RVO. *Windparken op De Noordzee*. Nov. 2023. URL: https://www.rvo.nl/onderwerpen/windenergie-op-zee/windparken-noordzee.

[56] SciPy. *SciPy Signal Processing Tutorial*. https://docs.scipy.org/doc/scipy/tutorial/signal.html. Accessed: 2024-10-24. 2024.

[57] SciPy Developers. *Fast Fourier Transform (FFT) Tutorial*. https://docs.scipy.org/doc/scipy/tutorial/fft.html. SciPy. 2023. URL: https://docs.scipy.org/doc/scipy/tutorial/fft.html.

[58] Ilaria Spiga, Gary Caldwell, and Rick Bruintjes. "Influence of Pile Driving on the Clearance Rate of the Blue Mussel, Mytilus edulis (L.)" In: vol. 27. July 2016, p. 040005. DOI: 10.1121/2.0000277.

[59] Kingsley Sunday and Feargal Brennan. "A review of offshore wind monopiles structural design achievements and challenges". In: *Ocean Engineering* 235 (2021), p. 109409. ISSN: 0029-8018. DOI: https://doi.org/10.1016/j.oceaneng.2021.109409. URL: https://www.sciencedirect.com/science/article/pii/S0029801821008192.

[60] M.J. Tucker, P.G. Challenor, and D.J.T. Carter. "Numerical simulation of a random sea: a common error and its effect upon wave group statistics". In: *Applied Ocean Research* 6.2 (1984), pp. 118–122. ISSN: 0141-1187. DOI: https://doi.org/10.1016/0141-1187(84)90050-6. URL: https://www.sciencedirect.com/science/article/pii/0141118784900506.

[61] Ramon Varghese, Vikram Pakrashi, and Subhamoy Bhattacharya. "A Compendium of Formulae for Natural Frequencies of Offshore Wind Turbine Structures". In: *Energies* 15.8 (2022). ISSN: 1996-1073. DOI: 10.3390/en15082967. URL: https://www.mdpi.com/1996-1073/15/8/2967.

[62] Jian-Hong Wan et al. "Natural Frequency Analysis of Monopile Supported Offshore Wind Turbines Using Unified Beam-Column Element Model". In: *Journal of Marine Science and Engineering* 11.3 (2023). ISSN: 2077-1312. DOI: 10.3390/jmse11030628. URL: https://www.mdpi.com/2077-1312/11/3/628.

[63] Xuefei Wang et al. "A review on recent advancements of substructures for offshore wind turbines". In: *Energy Conversion and Management* 158 (2018), pp. 103–119. ISSN: 0196-8904. DOI: https://doi.org/10.1016/j.enconman.2017.12.061. URL: https://www.sciencedirect.com/science/article/pii/S019689041731213X.

[64] Lindy Weilgart. *Best Available Technology (BAT) and Best Environmental Practice (BEP) for Mitigating Three Noise Sources: Shipping, Seismic Airgun Surveys, and Pile Driving - Technical Series No. 46*. CMS Secretariat, 2023. ISBN: 978-3-937429-37-3.

[65] Wind & Water works. *Dutch Offshore Wind Innovation Guide 2024*. Tech. rep. Nov. 2023. URL: https://www.rvo.nl/sites/default/files/2023-11/KiCdPayqFKa36nM1EBHlRdiJwgIneUZgPPy3N0_Q6KI.pdf.

[66] WindEurope. *Wind Energy in Europe: 2023 Statistics and the Outlook for 2024-2030*. Tech. rep. WindEurope, 2024. URL: https://windeurope.org/intelligence-platform/product/wind-energy-in-europe-2023-statistics-and-the-outlook-for-2024-2030/ (visited on 11/21/2024).

A

Calculation of the loads

In this appendix, the formulas used to calculate the hydraulic and wind forces from Section 4.1.1 are given. These formulas originate from the Python script that was used to calculate the hydraulic forces, hence the clear parameter distinction in each formula. First, a table is provided with the parameters used to make the calculations. Second, the equations are shown. Lastly, the calculated values are provided.

In the Table A.1 the parameters can be found that are used in the equation to make the calculations for the hydraulic and wind loads.

Table A.1: Parameters used for the calculation of the hydraulic and wind loads

Parameter	**Description**	**Value**	**Units**
D_{pile}	Pile diameter	10.0	m
γ_w	Wave spreading factor	0.9	-
γ_{cb}	Blockage factor	0.9	-
C_d	Drag coefficient	1.2	-
C_m	Inertia coefficient	1.9	-
ρ	Water density	1025	kg/m³
g	Gravitational acceleration	9.81	m/s²
$marine\_growth$	Additional diameter due to marine growth	0.2	m
MSL	Mean sea level	25	m
$H_{s,50}$	Significant wave height (50-year return period)	7.2	m
$H_{max,50}$	Maximum wave height (50-year return period)	13.9	m
$current_{50}$	Current speed (50-year return period)	1.15	m/s
HAT_{50}	Highest astronomical tide (50-year return period)	2.4	m
d	Water depth	25	m
ρ_a	Air density	1.225	kg/m³
C_a	Wind drag coefficient	0.8	-
v_{ref}	Rated wind speed at reference height	37.72	m/s
z_{ref}	Reference height for rated wind speed	100	m
α	Wind shear exponent	0.10	-
D_1	Diameter of section 1 (0 to 30m height)	10	m
H_1	Height of section 1	30	m
D_{bottom}	Diameter at 30m height	10	m
D_{top}	Diameter at 150m height	6.5	m
$H2_{start}$	Starting height of section 2	30	m
$H2_{end}$	Ending height of section 2	150	m
$water\_depth$	Water depth above mudline	25	m
$apply\_height\_mudline$	Height above mudline for equivalent force	50	m
$height\_above\_mudline$	Height above mudline where force is applied	50	m

Calculation of Peak Period T_p for the 50-year Return Period
The peak period T_p is calculated using the significant wave height H_s using the formula:

$$T_{p,50} = 5.3\sqrt{H_{s,50}} = 14.2s \tag{A.1}$$

Amplitude Calculation ζ_{50}

$$\zeta_{50} = 0.5 \cdot 1.94 \cdot H_{s,50} = 6.98m \tag{A.2}$$

Maximum water level

$$D_{max,50} = MSL + 0.5 + 0.5 \cdot HAT_{50} = 26.7m \tag{A.3}$$

Maximum height that the waves reach

$$D_{upper,50} = D_{max,50} + \zeta_{50} = 33.68m \tag{A.4}$$

$$D_{lower,50} = 0m \tag{A.5}$$

$$D_{mid,50} = \frac{D_{upper,50} - D_{lower,50}}{2} = 16.84m \tag{A.6}$$

Reference heights for Wheeler stretching

$$z_{upper,50} = 6.98m \tag{A.7}$$

$$z_{mid,50} = D_{max,50} \cdot \left(\frac{D_{max,50} + z_{mid,50,pre}}{D_{max,50} + \zeta_{50}} - 1 \right) = -9.86m \tag{A.8}$$

$$z_{lower,50} = -D_{max,50} = -26.7m \tag{A.9}$$

Wave length, number and angular frequency
Using the wavelength function defined in the code: Wave number k_{50} and angular frequency ω_{50} are calculated as:

$$\omega_{50} = \frac{2\pi}{T_{p,50}} \tag{A.10}$$

$$\alpha = \frac{\omega_{50}^2 \cdot d}{9.81} \tag{A.11}$$

$$k_{50} = \frac{\alpha \left(\tanh \alpha\right)^{-0.5}}{d} \tag{A.12}$$

$$L_{50} = \frac{2\pi}{k_{50}} = 214.2m \tag{A.13}$$

Wave Particle Velocities
For upper, mid, and lower levels, the velocities are calculated as:

$$u_{upper,50} = \zeta_{50} \cdot \omega_{50} \cdot \frac{\cosh(k_{50} \cdot D_{max,50})}{\sinh(k_{50} \cdot D_{max,50})} \cdot \gamma_w + \text{current}_{50} \cdot \gamma_{cb} \tag{A.14}$$

$$u_{mid,50} = \zeta_{50} \cdot \omega_{50} \cdot \frac{\cosh(k_{50} \cdot (D_{max,50} + z_{mid,50}))}{\sinh(k_{50} \cdot D_{max,50})} \cdot \gamma_w + \text{current}_{50} \cdot \gamma_{cb} \tag{A.15}$$

$$u_{low,50} = \zeta_{50} \cdot \omega_{50} \cdot \frac{\cosh(k_{50} \cdot (D_{max,50} + z_{lower,50}))}{\sinh(k_{50} \cdot D_{max,50})} \cdot \gamma_w + \text{current}_{50} \cdot \gamma_{cb} \tag{A.16}$$

Water Particle Accelerations
Similarly, water particle accelerations are calculated:

$$\dot{u}_{upper,50} = \zeta_{50} \cdot \omega_{50}^2 \cdot \frac{\cosh(k_{50} \cdot D_{max,50})}{\sinh(k_{50} \cdot D_{max,50})} \tag{A.17}$$

$$\dot{u}_{mid,50} = \zeta_{50} \cdot \omega_{50}^2 \cdot \frac{\cosh(k_{50} \cdot (D_{max,50} + z_{mid,50}))}{\sinh(k_{50} \cdot D_{max,50})} \tag{A.18}$$

$$\dot{u}_{low,50} = \zeta_{50} \cdot \omega_{50}^2 \cdot \frac{\cosh(k_{50} \cdot (D_{max,50} + z_{lower,50}))}{\sinh(k_{50} \cdot D_{max,50})} \tag{A.19}$$

Drag and Inertia Forces
Drag and inertia forces for the different levels are given by:

$$F_{d,50} = 0.5 \cdot \rho \cdot C_d \cdot (D_{pile} + \text{marine\_growth}) \cdot u \cdot |u| \tag{A.20}$$

$$F_{i,50} = \frac{\pi}{4} \cdot \rho \cdot C_m \cdot (D_{pile} + \text{marine\_growth})^2 \cdot \dot{u} \tag{A.21}$$

Total Combined Forces
The total forces are calculated by summing up the drag forces and the inertia forces and using the following equation to calculate the total hydraulic force:

$$F_{tot,50} = \sqrt{F_{d,50}^2 + F_{i,50}^2} \tag{A.22}$$

Resulting in the forces as shown in Table A.2.

Table A.2: Calculated forces at the different heights representing the forcing profile

Location	Total Force [kN/m]
Upper	459.72
Mid	428.71
Lower	337.69

The base shear is calculated using Simpson's rule:

$$F_{base,50} = \frac{(z_{upper,50} - z_{lower,50})}{6} (F_{tot,50,upper} + 4 \cdot F_{tot,50,mid} + F_{tot,50,lower}) = 11.45MN \tag{A.23}$$

The overturning moment at the base is calculated according to:

$$\begin{aligned} M_{oe,50} = & F_{base,50} \cdot |D_{max,50}| + \frac{(z_{upper,50} - z_{lower,50})}{6} \\ & (F_{tot,50,upper} \cdot |z_{upper,50}| + 4 \cdot F_{tot,50,mid} \cdot |z_{mid,50}| + F_{tot,50,lower} \cdot |z_{upper,50}|) \\ & = 487.38MNm \end{aligned} \tag{A.24}$$

Wind Force Calculation
The wind speed profile is:

$$v(z) = v_{ref} \left(\frac{z}{z_{ref}} \right)^{\alpha} \tag{A.25}$$

The wind load per unit length is given for the first section with a constant diameter:

$$q_{wind,1}(z) = 0.5 \cdot \rho_a \cdot C_a \cdot D_1 \cdot v(z)^2 \tag{A.26}$$

For the second section where the diameter tapers from $10m$ to $6.5m$ at the top of the tower:

$$q_{wind,2}(z) = 0.5 \cdot \rho_a \cdot C_a \cdot D(z) \cdot v(z)^2 \tag{A.27}$$

where $D(z)$ is linearly varying between D_{bottom} and D_{top}.

By integrating the profiles and adding the found forces the following total wind force is found:

$$F_{wind,tot} = 796.79kN \approx 0.8MN \tag{A.28}$$

The overturning moment caused by this wind force is equal to:

$$M_{OE,wind} = h_{ref} \cdot F_{wind,tot} = 80MNm \tag{A.29}$$

By adding the hydraulic shear force at the base with the total wind force the total base shear is found:

$$F_{total,base,50} = F_{base,50} + F_{wind,tot} = 12.45MN \tag{A.30}$$

Similarly, for the overturning moment:

$$M_{OE,total,base,50} = M_{oe,50} + M_{OE,wind} = 567.38MNm \tag{A.31}$$

B Model Visualisation

In this appendix, multiple plots of the outcomes of the different analyses are provided. The goal of these plots is to give insights into what happened during the modelling in Plaxis 3D and to support the understanding of the found results. First, figures of the generated meshes are shown. Second, plots from the pushover analysis are provided. Third, figures of the free vibration are provided. Lastly, figures are provided for both cyclic static analyses.

B.1. Generated Meshes

In figures B.1, B.2 the generated meshes of the monopile and caisson model with tower are shown, together with the dimension of the meshes.

Generated Mesh of the Monopile with Tower Model

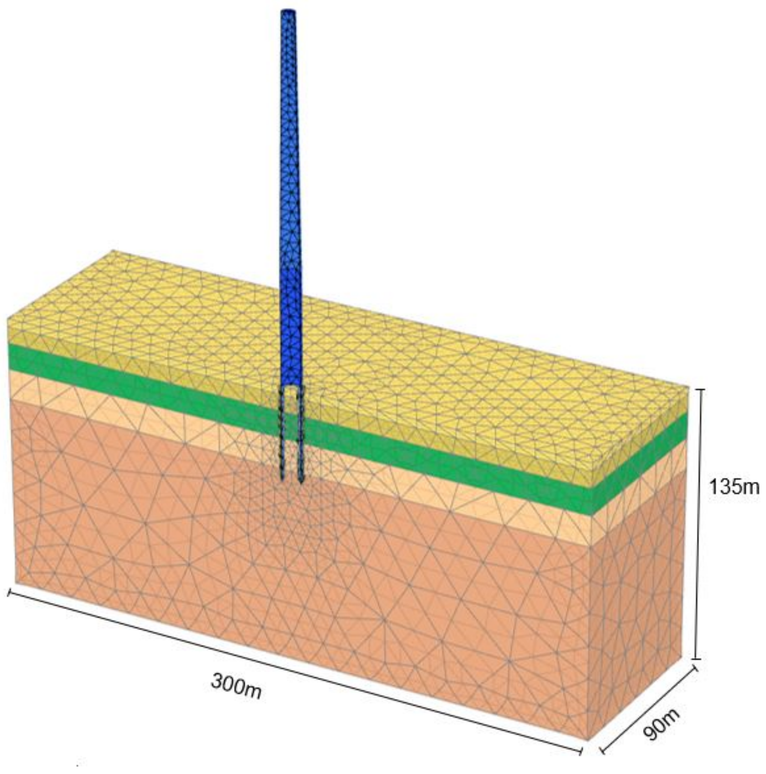

Figure B.1: Generated mesh of the monopile with tower model

Generated Mesh of the Caisson with Tower Model

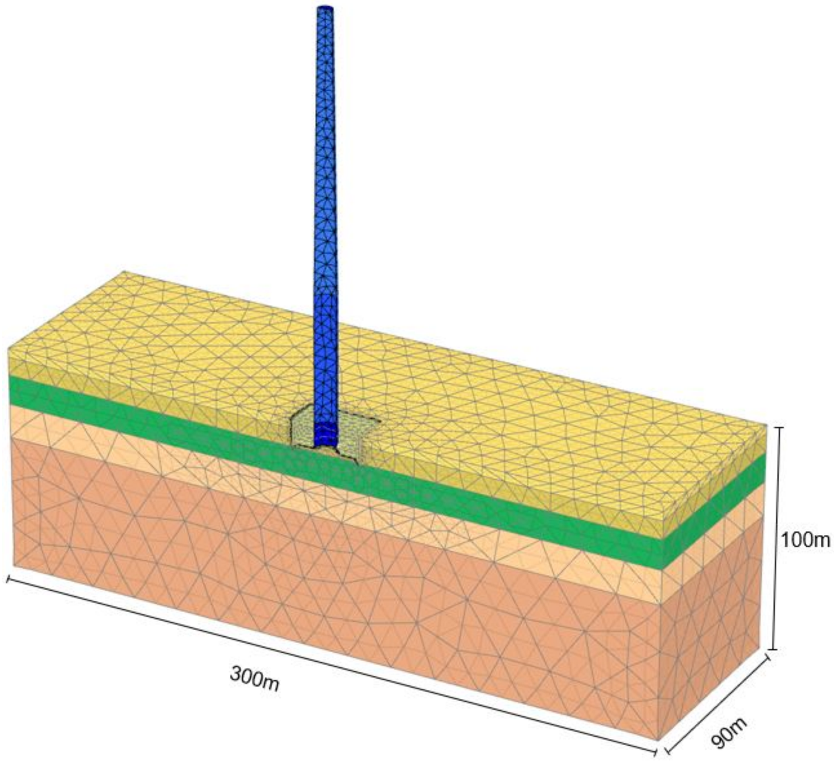

Figure B.2: Generated mesh of the caisson with tower model

In Figures B.3, B.4 the generated meshes of the monopile and caisson model 5D models are shown, together with the dimension of the meshes.

Generated Mesh of the 5D Monopile

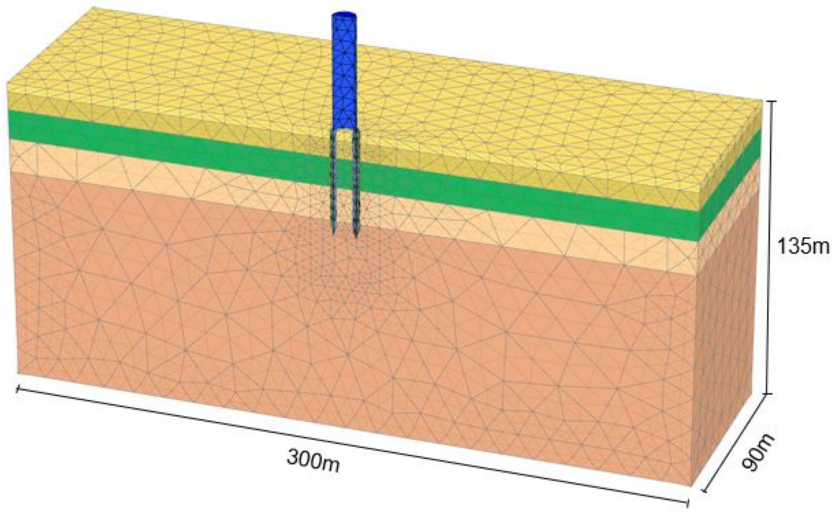

Figure B.3: Generated mesh of the monopile 5D model

Generated Mesh of the 5D Caisson

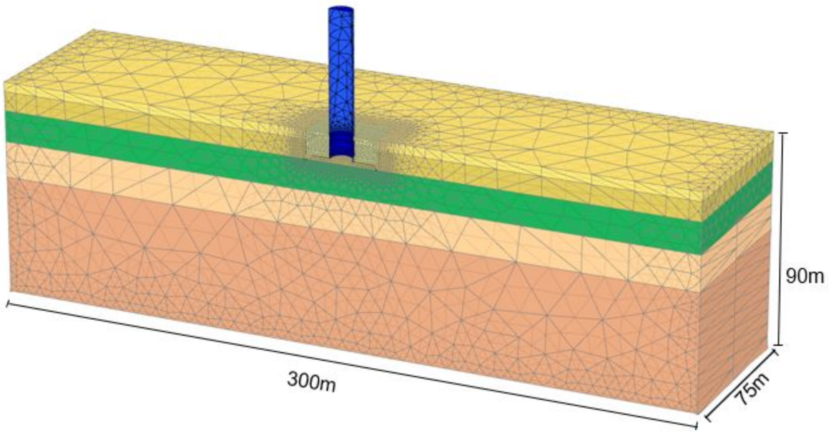

Figure B.4: Generated mesh of the caisson 5D model

B.2. Pushover Analysis

B.2.1. Pushover Analysis of the Monopile with Tower Model

In Figure B.5 the connectivity plot of the monopile with tower model is shown to display the finer mesh around the monopile and the interface between the structure and the surrounding soil.

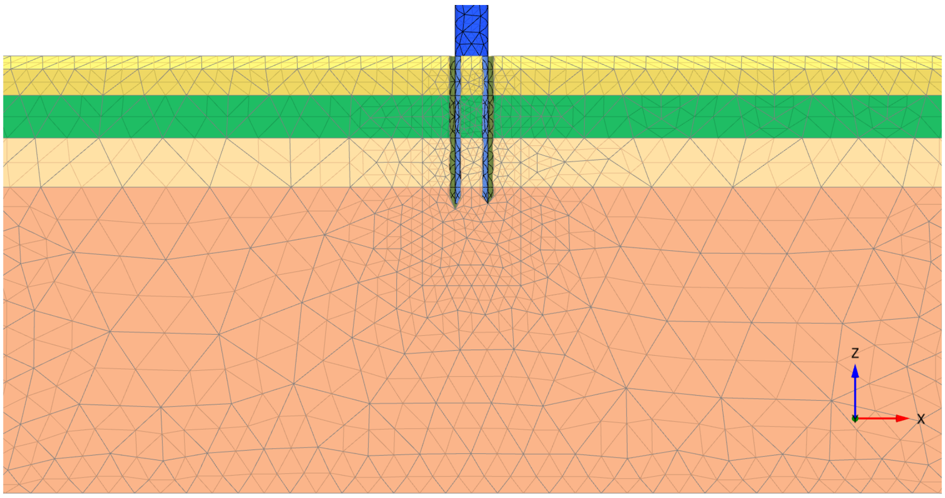

Figure B.5: Connectivity plot monopile with tower model

In Figure B.17 the deformed mesh of the total displacement is shown. The maximum deflection of 44 meter is at the top of the tower. The base displacement is 1.151 meter as can be seen in figure B.9 and B.10. In this figure, the shaded plot and vector plot of the base displacement are given respectively. In figures B.7 and B.8 the shaded and vector plots of the total displacement at this base displacement are shown.

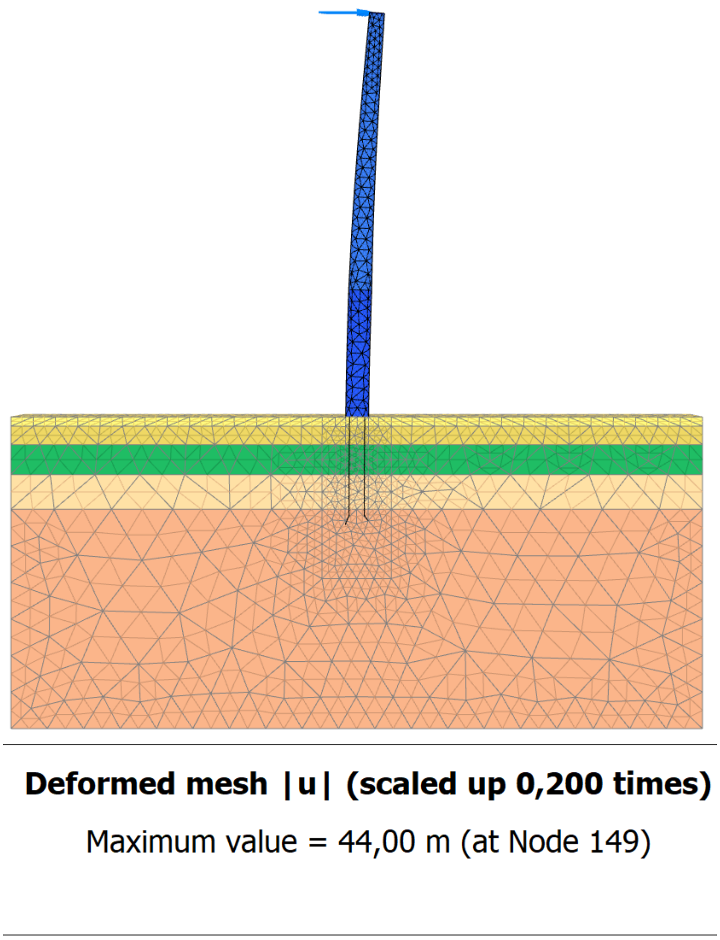

Figure B.6: Deformed mesh total displacement push-over 1-meter base displacement monopile with tower model

Total Displacement of the Monopile with 1-meter Base Displacement

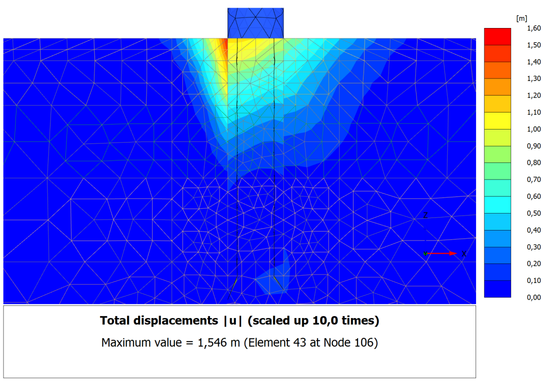

Figure B.7: Push over total displacement monopile shaded

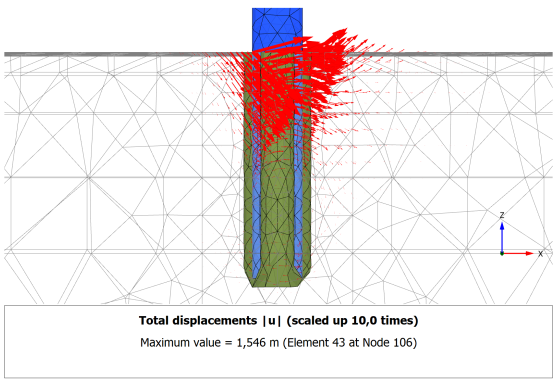

Figure B.8: Push over total displacement monopile vector

Base Displacement of 1-meter Monopile

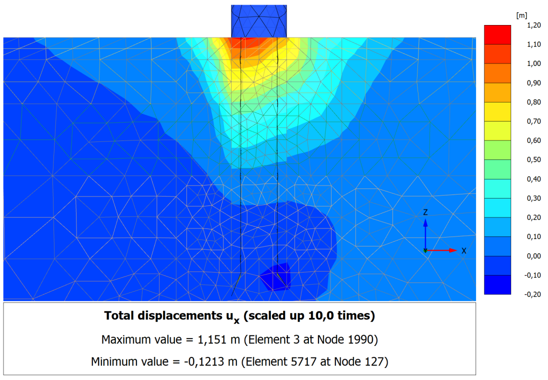

Figure B.9: Pushover 1-meter base displacement monopile shaded

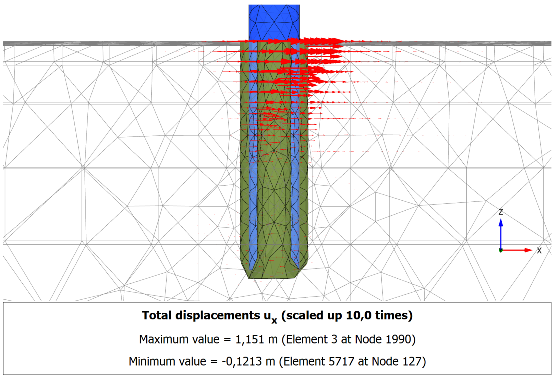

Figure B.10: Pushover 1-meter base displacement monopile vector

B.2.2. Pushover Analysis Caisson with Tower Model

In figure B.11 the connectivity plot of the caisson with tower model is shown to show the finer mesh around the caisson and the interface between the structure and the surrounding soil.

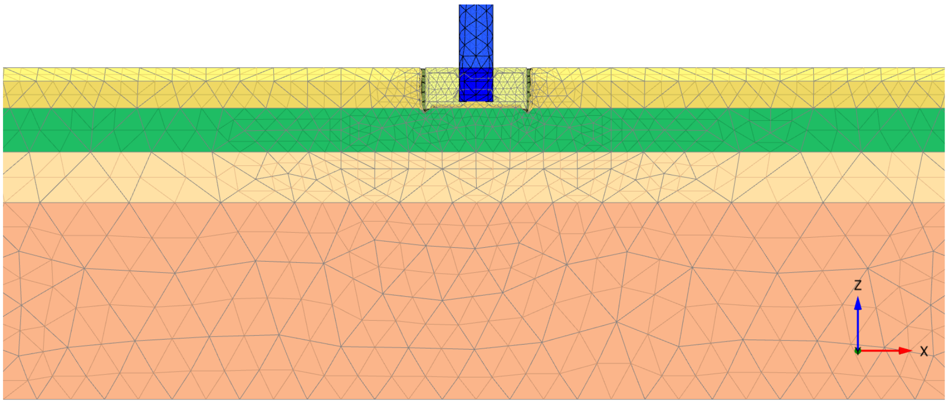

Figure B.11: Connectivity plot caisson with tower model

In figure B.17 the deformed mesh of the total displacement is shown. The maximum deflection of 35.72 meter is at the top of the tower. The base displacement is 1.247 meter as can be seen in figure B.9 and B.10. In this figure, the shaded plot and vector plot of the base displacement are given respectively. In figures B.7 and B.8 the shaded and vector plots of the total displacement at this base displacement are shown.

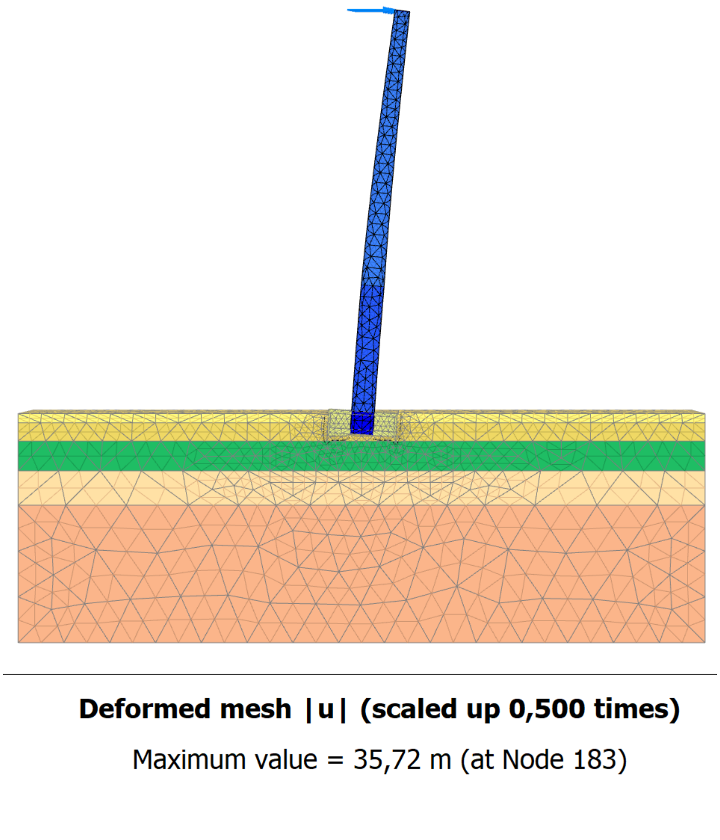

Figure B.12: Deformed mesh total displacement push-over 1 meter base displacement caisson with tower model

Total Displacement of the Caisson with 1-meter Base Displacement

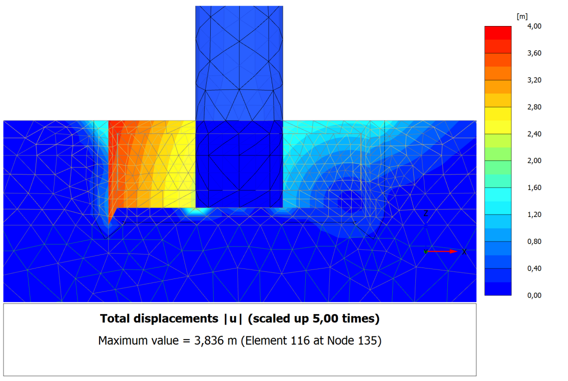

Figure B.13: Push over total displacement caisson shaded

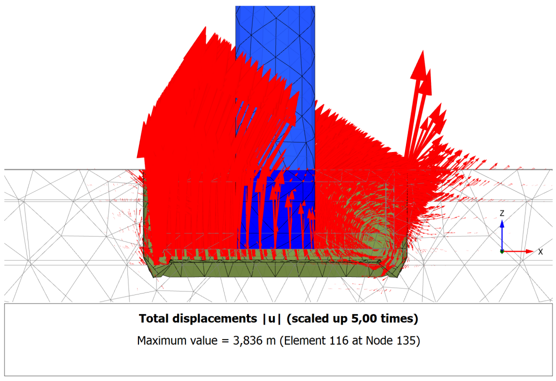

Figure B.14: Push over total displacement caisson vector

Base Displacement of 1-meter Caisson

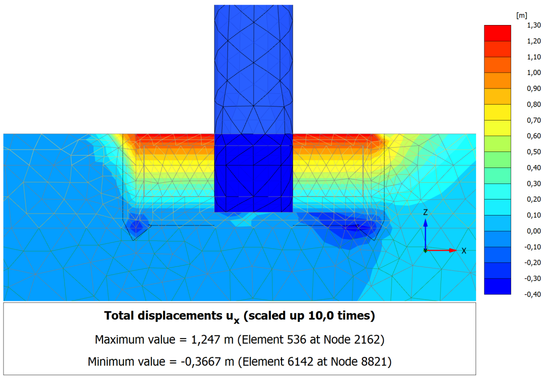

Figure B.15: Push over one meter base displacement caisson shaded

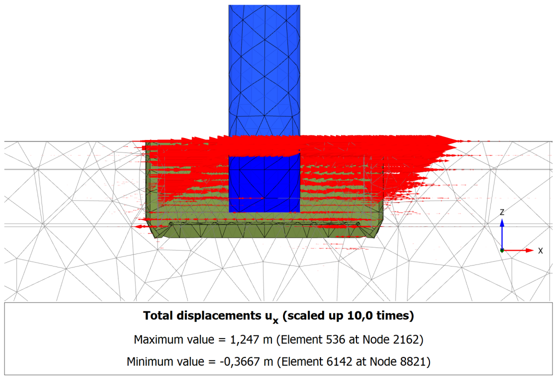

Figure B.16: Push over 1-meter base displacement caisson vector

B.3. Free Vibration Analysis

In this section, plots of the free vibration analysis for the monopile and caisson with tower models are shown.

B.3.1. Free vibration analysis monopile with tower model

Deformed Mesh Free Vibration Analysis

In figures B.17, B.17 and B.19 the deformed mesh of the first cycle of the free vibration is displayed.

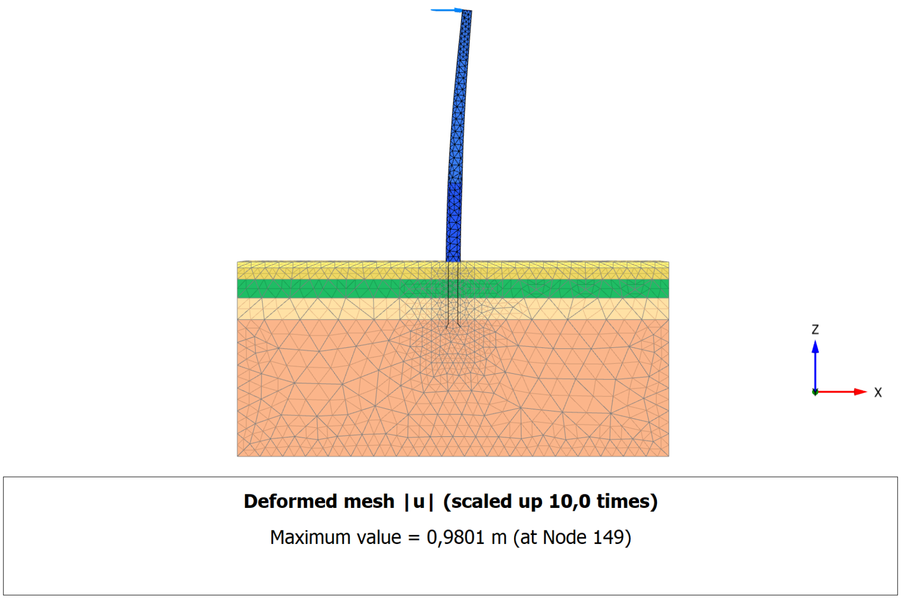

Figure B.17: Deformed mesh of the monopile with tower model at the start of the analysis

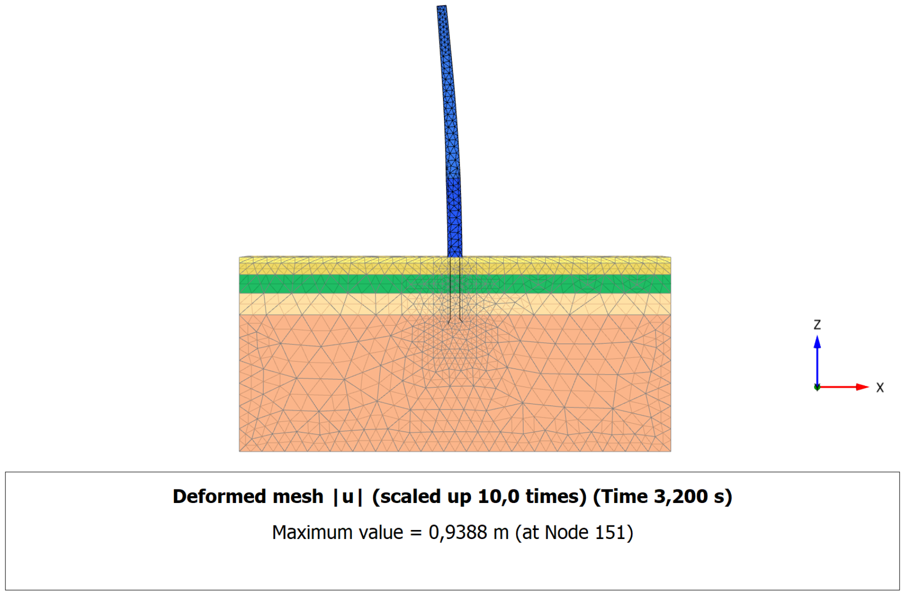

Figure B.18: Deformed mesh of the monopile with tower model after half a cycle of the analysis

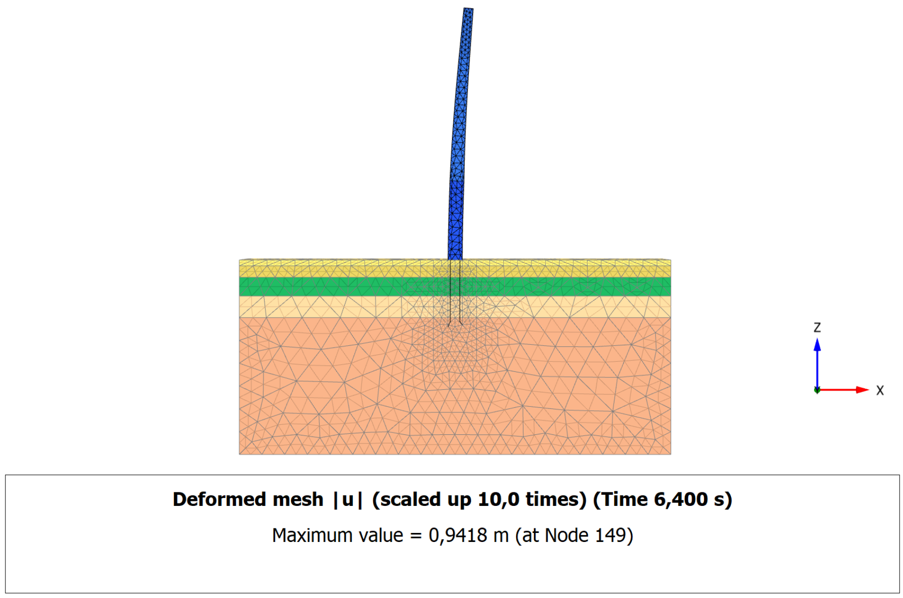

Figure B.19: Deformed mesh of the monopile with tower model after one cycle of the analysis

Shaded and Vector Plots of the Monopile with Tower Model

In the figures below, the shaded and vector plots of the total displacement of the free vibration analysis of the monopile with complete tower model are shown. The plots show the total displacement at the start, halfway, and after one full cycle of the free vibration. The plots give insights into the deformation and the rotation of the soil and the monopile.

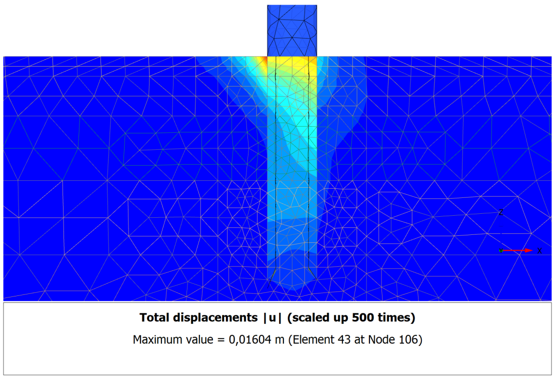

Figure B.20: Total displacement at the start of the analysis monopile with tower model shaded plot

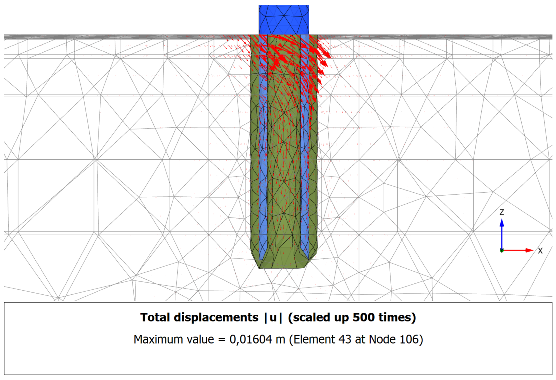

Figure B.21: Total displacement at the start of the analysis monopile with tower model vector plot

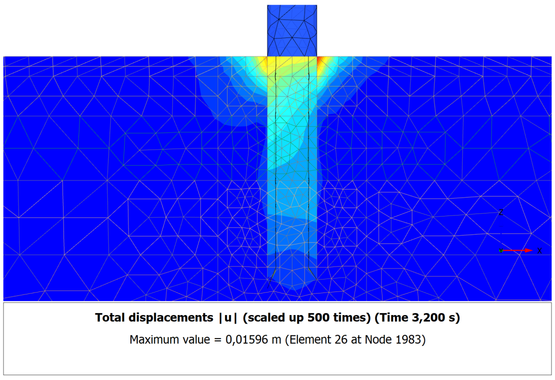

Figure B.22: Total displacement after half a cycle monopile with tower model shaded plot

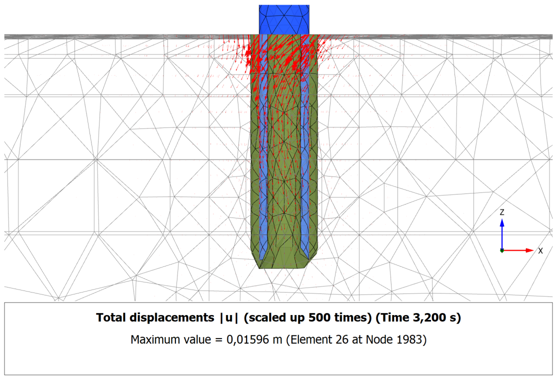

Figure B.23: Total displacement after half a cycle monopile with tower model vector plot

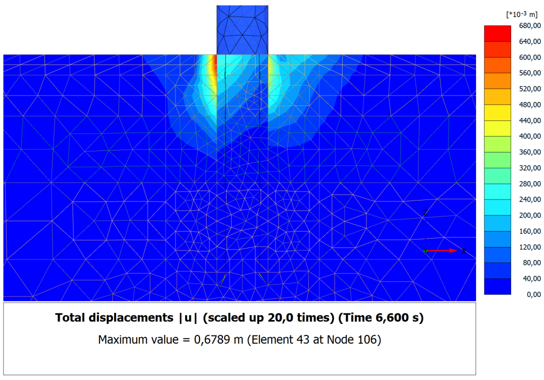

Figure B.24: Total displacement after one cycle monopile with tower model shaded plot

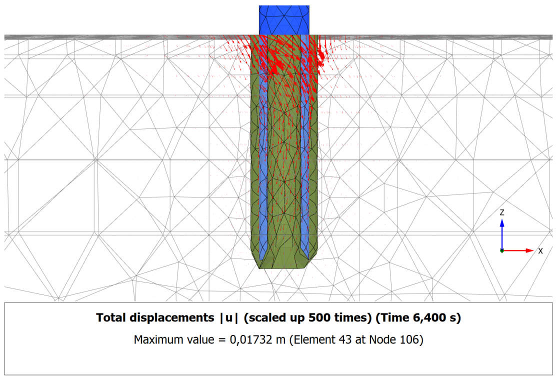

Figure B.25: Total displacement after one cycle monopile with tower model vector plot

B.3.2. Free Vibration Analysis Caisson with Tower Model

Deformed mesh of the free vibration

In figures B.26, B.26 and B.28 the deformed mesh of the first cycle of the free vibration is displayed.

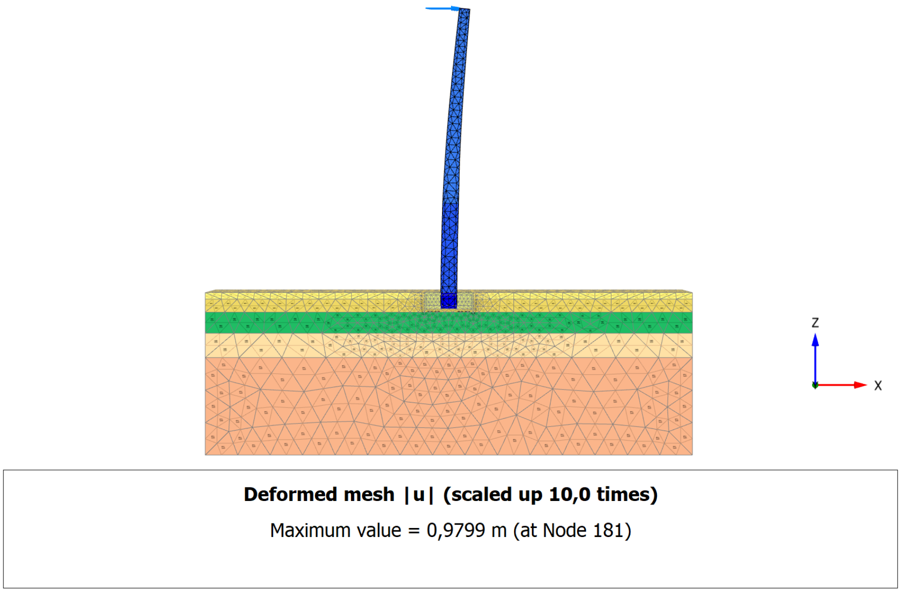

Figure B.26: Deformed mesh of the caisson with tower model at the start of the analysis

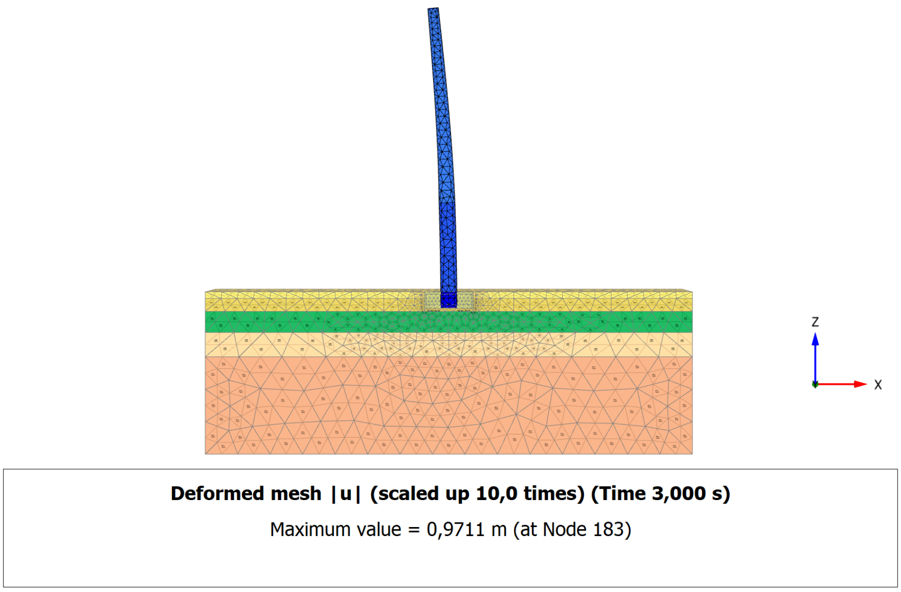

Figure B.27: Deformed mesh of the caisson with tower model after half a cycle of the analysis

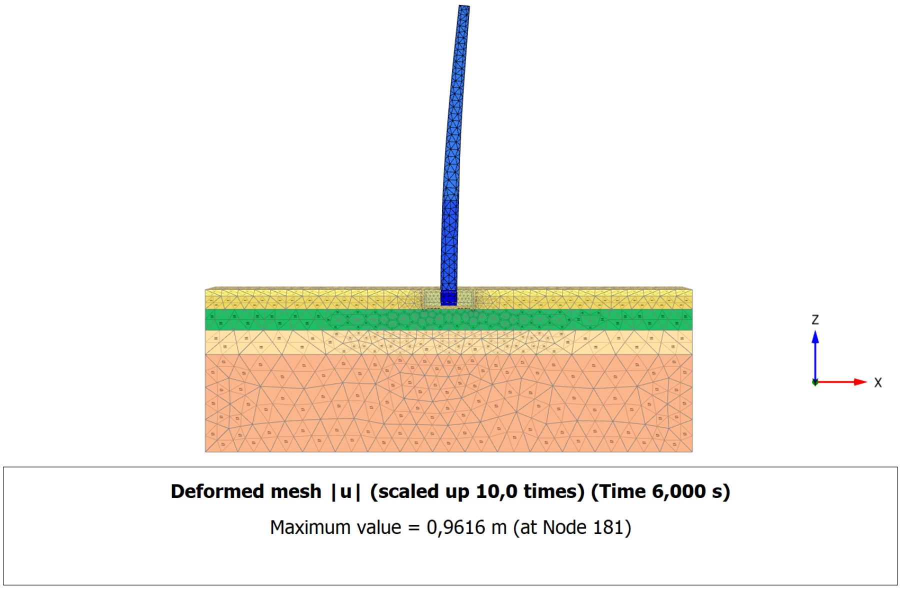

Figure B.28: Deformed mesh of the caisson with tower model after one cycle of the analysis

In the following figures, the shaded and vector plots of this first cycle of the free vibration are displayed.

Shaded and vector plots of the caisson with tower model

In the figures below, the shaded and vector plots of the total displacement of the free vibration analysis of the caisson with complete tower model are shown. The plots show the total displacement at the start, halfway, and after one full cycle of the free vibration. The plots give insights into the deformation and the rotation of the soil and the caisson.

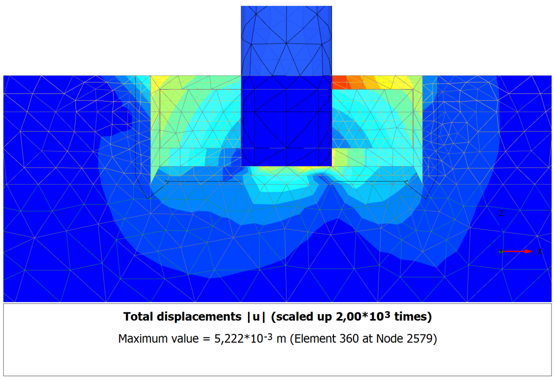

Figure B.29: Total displacement at the start of the analysis caisson with tower model shaded plot

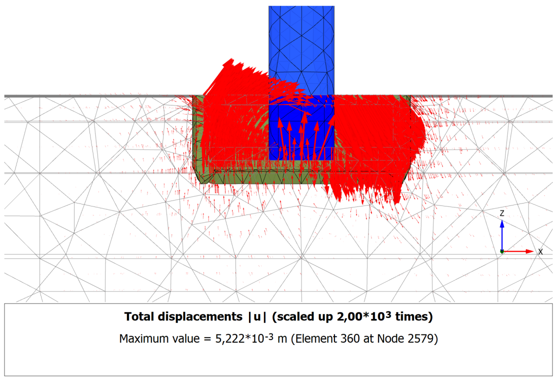

Figure B.30: Total displacement at the start of the analysis caisson with tower model vector plot

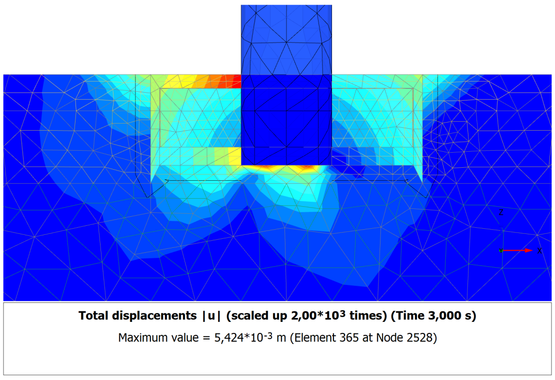

Figure B.31: Total displacement after half a cycle caisson with tower model shaded plot

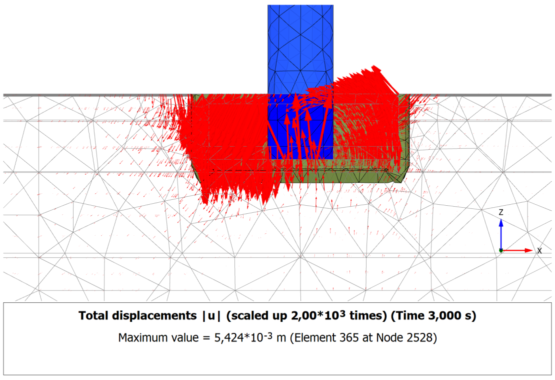

Figure B.32: Total displacement after half a cycle caisson with tower model vector plot

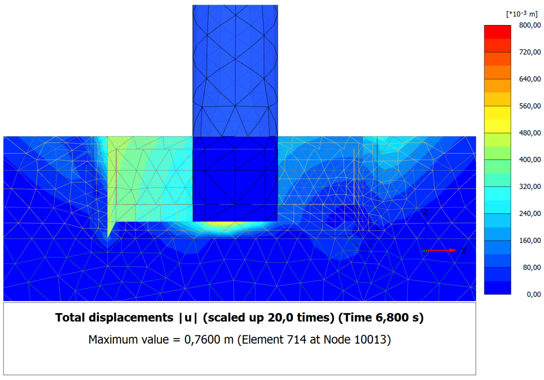

Figure B.33: Total displacement after one cycle caisson with tower model shaded plot

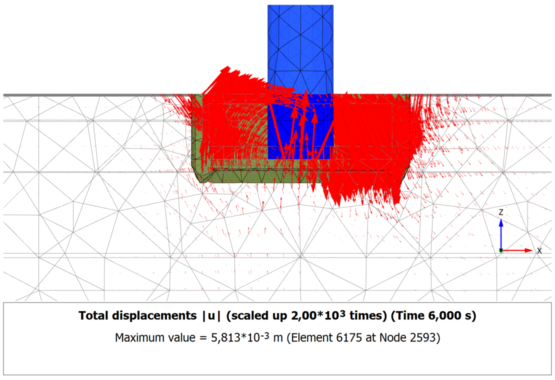

Figure B.34: Total displacement after one cycle caisson with tower model vector plot

B.4. Cyclic loading analysis

In this part of the appendix, additional stress-strain diagrams are provided to gain an extra understanding of the behaviour that is developing during the cyclic analysis.

The graph as shown in Figure B.35 displays the deviatoric stress-strain behaviour of the monopile under cyclic loading. Points 1 (blue) and 4 (green), closer to the mudline, show bigger stress-strain loops, indicating local plastic deformation and energy dissipation. Lower loading effects are visible in points 2 (red) and 3 (purple). During loading and unloading transitions, overshooting is visible, especially at Points 1 and 4, where stress peaks occur before stabilising. Progressive soil degradation is indicated by the increasing loops and accumulated strains.

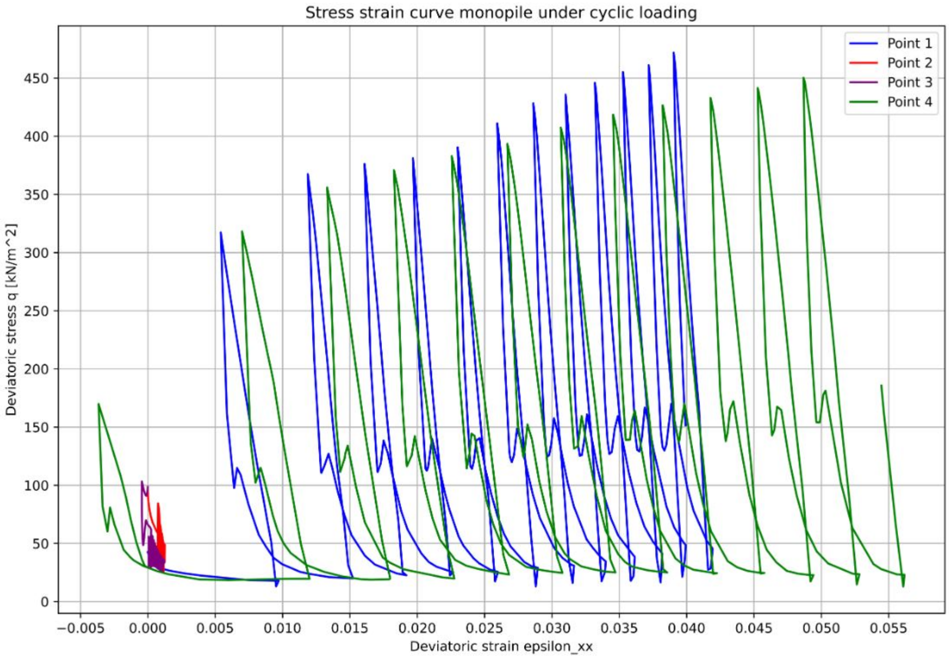

Figure B.35: Deviatoric stress-strain curve of the monopile

The graph displayed in Figure B.36 shows the deviatoric stress-strain response of a caisson under cyclic loading. The highest stresses in the caisson are approximately $110kN/m$, which is substantially less than the monopile's $400kN/m$. Points 1 (blue) and 4 (green), close to the mudline, have thinner loops, which suggests a more elastic reaction and less energy loss. Points 2 (red) and 3 (purple) show higher stress but almost zero strain accumulation. The higher stress values are likely caused by the stiffer response of the caisson when interacting with stiffer soil layers compared to the points closer to the mudline. In comparison to the monopile, there is little accumulation of strains, indicating less cyclic degradation, and the stresses are lower compared to the monopile. This is probably because of the caisson's wider load distribution. Overshooting effects, which are visible in the monopile graph, are less noticeable here. In general, the caisson appears to handle the loading more effectively than the monopile and shows more stable and controlled cyclic behaviour.

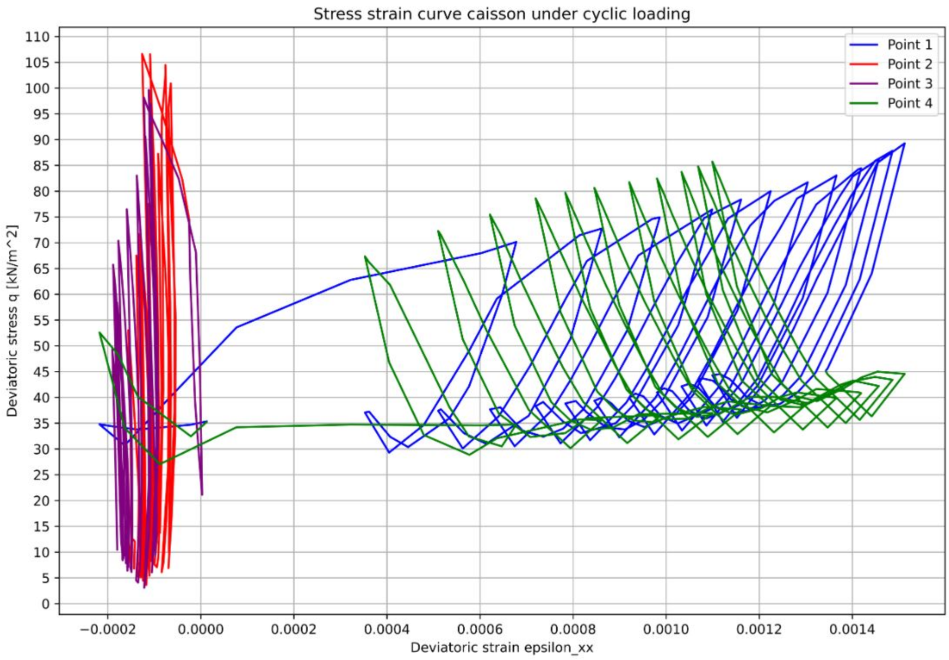

Figure B.36: Deviatoric stress-strain curve of the caisson